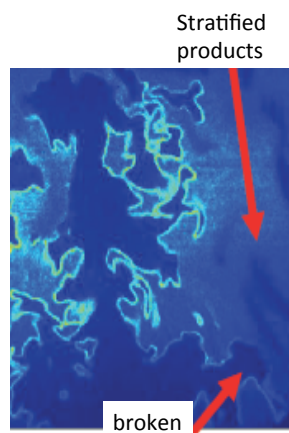
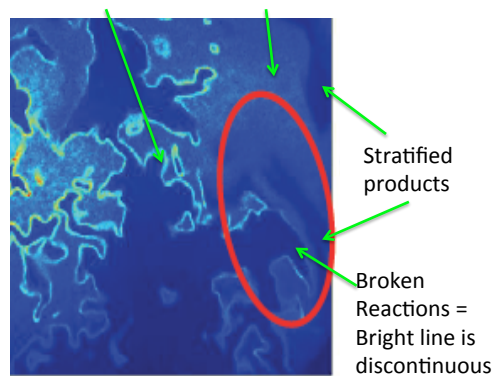


How to achieve broken reactions ? - stratified products

simultaneous CH-OH PLIF (Carter, Driscoll, Skiba, Wabel):

CH reaction layer =
thin bright blue line

OH products =
broad light blue



→ keep products hot to avoid broken reactions

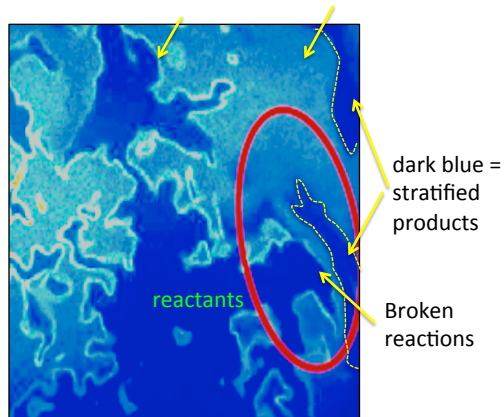


37

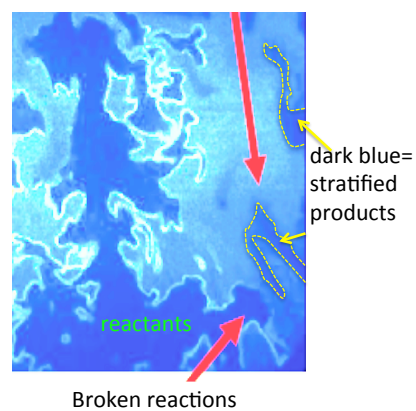
Stratified Products - lead to broken reactions

CH reaction layer =
thin bright blue line

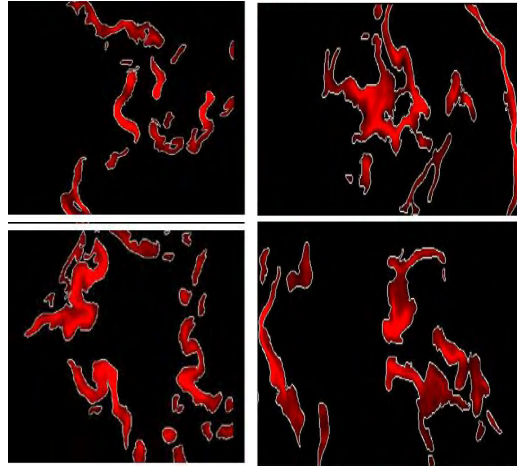
OH products =
broad light blue



CH-OH method of Cam Carter



Broken reaction layers - with stratified products



What happens at “extreme” levels of turbulence ?

Wabel, Skiba, Driscoll, to PROCI 36

- As u'/SL is increased to “extreme” values of 240, preheat zone gets very thick = 16 times the laminar thickness
- The reaction layers do not become thick, and remain at 1-2 times their laminar thickness
- Extreme turbulence is predicted to cause “broken” reactions, but no broken reactions were seen, even when turbulence was 10 times the predicted limit
As long as the product gas were kept hot – no stratification of products because of No outside air entrainment
- If some outside air was entrained to cause stratification of product, then some Broken reactions were observed
- Distributed reactions were not observed in the Bunsen flame, even for extreme Turbulence levels. Distributed requires preheating of reactants and internal Hot gas recirculation, such as in a gas turbine combustor



Additional axes needed on the Borgi regime diagram

Da_2 = residence time of eddies in flame (x/U) / chemical time

Reactivity ($Y. Ju$) = Initial temperature of reactants / ignition temp.
(T_R / T_{ig})

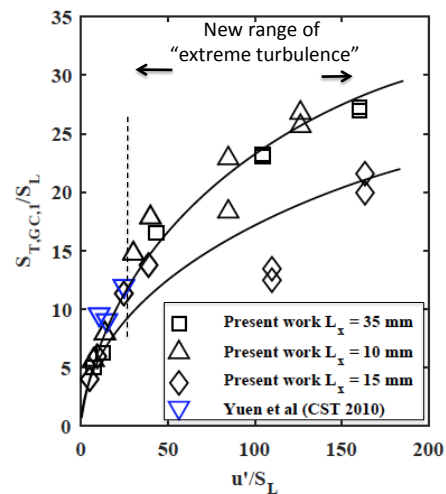
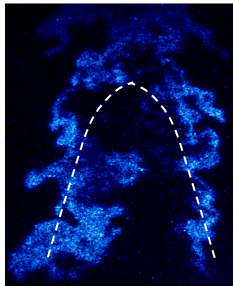
Degree of stratification = "DS" = [T'_{rms} / T]_{products}
controls "broken" regime boundary



41

Turbulent Burning Velocity

$$S_T = \frac{\dot{m}_R}{\rho_R A_T}$$




Wabel, Driscoll, PROCI 36, 2016



42

Turbulent Burning Velocity – what happens at extremely large turbulence levels ?

correlations are different for each “canonical geometry”



$$\frac{S_T}{S_L} = \frac{A_T}{A_L} = \left[1 + C_1 \left(\frac{u'}{S_L} \right)^2 \right]^{1/2} - \left[C_2 \left(\frac{u'}{S_L} \right)^2 \right]$$

Schelkin theory Bending term

Bending term = due to ? Eddies destroyed traversing preheat layer ?
Geometric effects
Strain causes local extinction ?

Function C_1 and C_2 = ? Depend on integral scale ? Residence time
due to mean velocity ?

Extend Burning velocity curve to “extremely” high turbulence levels (10X)



43

What do all these measurements mean ? Implications for models

Turbulent Burning Velocity S_T increases if
Thermal diffusivity α_T increases, or
Reaction rate $\dot{\omega}_p$ increases

$$\bar{\rho} S_T \frac{d\bar{c}}{dx} = \bar{\rho} \alpha_T \frac{d^2 \bar{c}}{dx^2} + \bar{\omega}_p$$

Diffusivity: model $\alpha_T = \nu_T$ = related to resolved
scale velocity gradients (Smagorinsky)

$$c = \frac{T - T_R}{T_P - T_R}$$

How to model reaction rate $\bar{\omega}_p$? Depends on probability that flamelet is at a point

i) $\bar{\omega}_p = \rho_R S_L \Sigma$ + flame surface density (Σ) transport eqn (Bray, F-TacLES, Fureby)

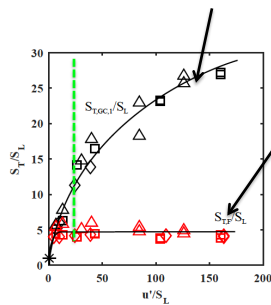
ii) Or Set $\bar{\omega}_p(\bar{c}, \bar{c}'^2) = \int_0^1 \dot{\omega}_p(c) P(c, \bar{c}, \bar{c}'^2) dc$ + need PDF shape near $c = 0.5$
FPV (Moin, Pitsch, Ihme)



44

Implications for modeling

1. Provide modelers → measured PDF and flame surface density → to correctly model reaction rate, for methane and JP-8 at high Re
2. Provide modelers → measured Consumption Speed ($S_{T,G}$) for “extreme” turbulence = mass flow rate of reactants / density reactants / area for methane, JP-8 at high Re
Models also should compute correct flame brush thickness
3. Model should predict “bending” at high Re



Wabel, Skiba, Driscoll, Seoul Symp.

4. Model should predict Thin Flamelet Component (FC) of burning velocity

$$(S_{T,F}) = S_L (A_T/A_L) \quad \text{where} \\ A_T \approx \text{integral of flame surface density}$$

Model should explain why Flamelet Component curve is flat?
= flame cannot wrinkle
any more, but propagates faster



45

Implications for modeling , continued

5. Model should account for “**Differential Broadening**” – Preheat layer is broadened by 16X but reaction layer broadened by only by 2X
6. Model should explain **Variation of turbulence** across flame brush
7. Model should predict that
 - **Stratified** flames become broken & distributed but
 - non-stratified flames do not
8. Model should explain why **Geometries** of Bunsen, spherical, gas turbine / swirl flames lead to → different turbulent burning velocities
9. Model should predict - measured effect of **Preheating** the reactants (Y. Ju)
10. Model should predict differences due to JP-8 **Pyrolysis layer**



46

What global metrics MUST a model predict correctly ?

before attempting to measure individual terms ?

Premixed turbulent flames:

Global Consumption Speed vs u' Model first must demonstrate it can predict measured height of a bunsen flame, angle of a V flame, dR/dt of spherical flame

Flame Brush thickness - as function of distance (Bunsen) or time (spherical)

Carbon Monoxide Emission Index - g CO / kg fuel

Non-premixed turbulent flames (jet, jet in coflow, jet in crossflow)

Flame Length (properly defined) as function of U_F , U_A , etc.

Carbon Monoxide Emission Index - g CO / kg fuel

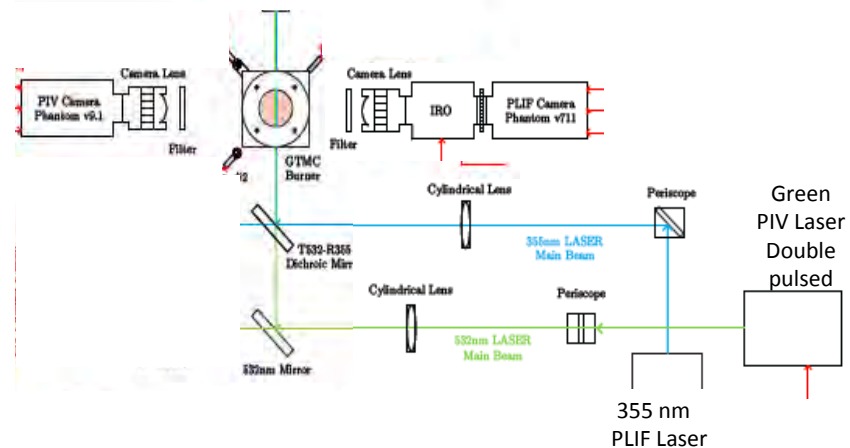


47

Kilohertz simultaneous PLIF and PIV

Quantronix kilohertz lasers - US made

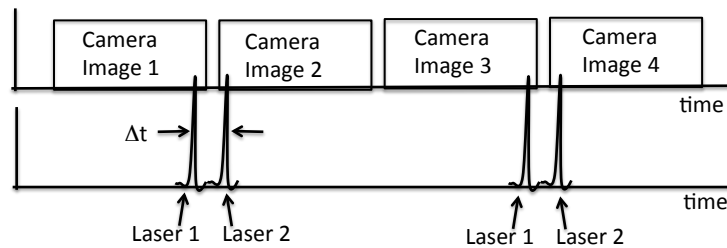
Edgewave kilohertz lasers – German made



48

“Frame straddling” - with kHz PIV

One PIV camera operating at 20,000 images/sec
Two lasers – each operating at 10,000 pulses /sec



$\Delta t = \Delta x / U$ want $\Delta x =$ distance particle moves = 1/3 interrogation box size

Interrogation box = one PIV velocity vector = 0.3 mm
so $\Delta x = 0.1$ mm

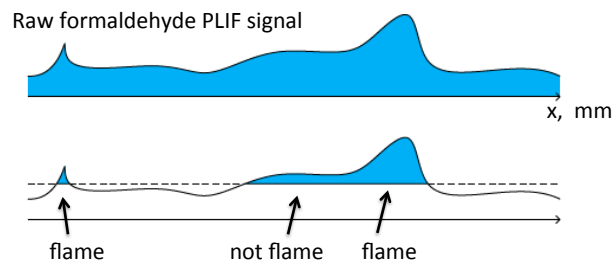
If $U = 50$ m/s, then $\Delta t = 2 \mu\text{s}$

camera must turn off, then turn on - in less than $2 \mu\text{s}$



49

Edge detection - to identify flame - from formaldehyde PLIF



Flame is at the sharp edge of the formaldehyde PLIF signal

Perform: thresholding for background subtraction

Spatial smoothing to remove noise, Canny edge detection algorithm

Check that flame is nearly continuous



50

CH Reaction layer

Cam Carter (AFRL)
 Tonghun Lee UIUC
 Driscoll (UM)
 Not yet published

10 kilohertz

314.4 nm C-X band

Case 5, $u'/S_L = 62$

Highly corrugated

Highly wrinkled

Merging



51

Excite CH at new wavelength 314 nm

Cam Carter, Tonghun Lee Appl. Phys. B 116:515

$C^2\Sigma^+ - X^2\Pi(0,0)$ Band

Previously CH excited $A^2\Delta - X^2\Pi(0,0)$ band at 431 nm
 and $B^2\Sigma - X^2\Pi(0,0)$ at 390 nm

New method is best for kHz lasers: developed by Cam Carter, Tonghun Lee

$C^2\Sigma^+ - X^2\Pi(0,0)$ Band at 314 nm

10 kHz diode-pumped, Q-switched Nd:YAG laser
 (Edge-Wave Innoslab IS12II-E)

532-nm pumps a dye laser (Sirah CREDO with DCM dye)

628 nm into a BBO frequency doubling crystal to 314 nm

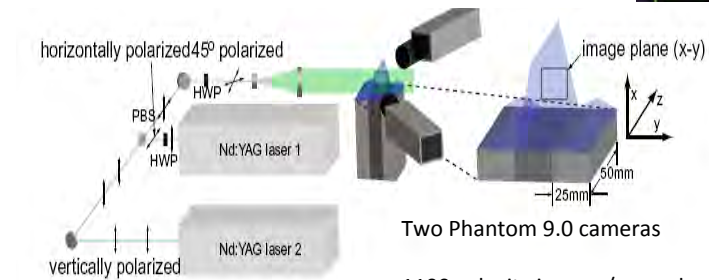
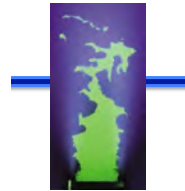
Linewidth is 0.1 cm^{-1} , duration 7 ns, energy is 0.22 mJ at 10 kHz



52

Steinberg, Driscoll Michigan 2-D Slot burner

measure stretch efficiency function for LES
complete velocity, flame surface data base
Cinema-stereo PIV



Two Clark OMB YAG lasers
Pulsed at 1100 pulses/sec

“fully-turbulent” $u'/S_L = 3.0$
 $S_T/S_L = 2.5$

Two Phantom 9.0 cameras

1100 velocity images/second
Scheimpflug stereo PIV optics

Small field of view 8 x 11 mm
Spatial resolution = 140 microns
Time resolution 0.9 ms



53

Kilohertz PIV

Steinberg, Driscoll
Comb. Flame 156, 2285
Michigan kHz PIV
eddies passing through flame

Sheet thickness = 200 microns
spatial resolution = 200 microns
temporal resolution = 4,000 Hz

Lasers:

Quantronix Hawk: 4,000 Hz, 355 nm,
for CH₂O PLIF

Quantronix Hawk PIV laser: 4,000 Hz,
for PIV

Cameras:

Phantom v711 +LaVision high speed
Intensifier

Phantom 9.1




54

Observe eddy pairs –consistent with Damköhler, Schelkin

Colors = Vorticity (ω_z); -700 s^{-1} (blue)
and 700 s^{-1} (red)

Field of view = 6 mm x 10.5 mm,
 $\Delta t = 0.9 \text{ ms}$

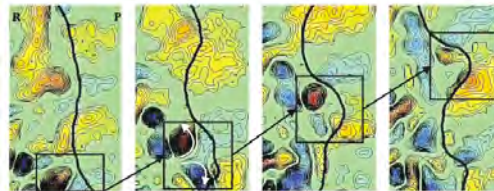
1. Initial Vortex Pair
2. Vortex Pair Disappears
3. Wrinkle in Flame Appears

Reactants 

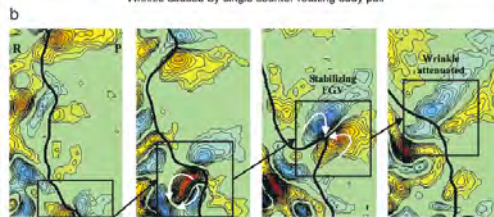
Products



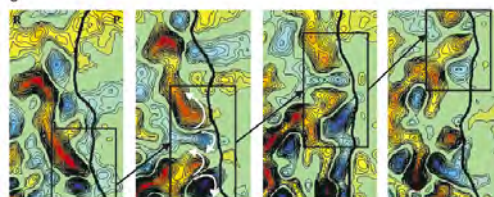
55



Wrinkle caused by single counter-rotating eddy pair

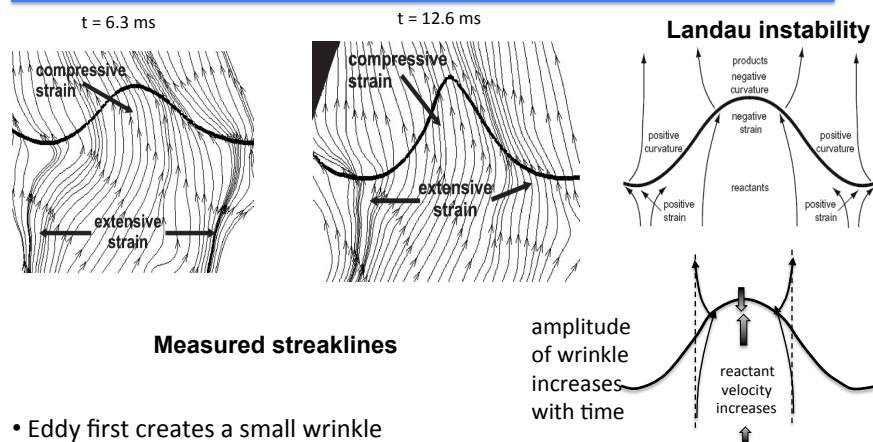


Flame generated vorticity observed



56

What do kHz diagnostics tell us ? Hydrodynamic Instability observed

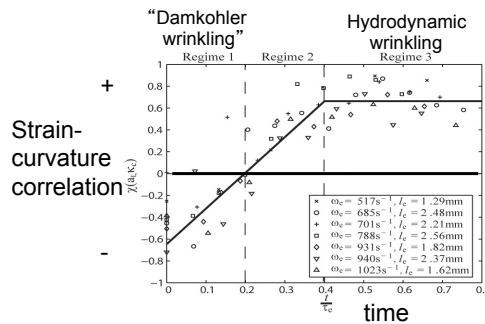


- Eddy first creates a small wrinkle
- Measured diverging streaklines agree with theory
- Strain and curvature are positively correlated
- Wrinkle forms cusp due to hydrodynamic instability



KHz diagnostics tell us - the Time History of the Eddy-Flame Interactions

- **Early times:** observe “Damkohler-like” wrinkling sometimes
Strain & curvature are negatively correlated as predicted
- Later times: vortex is destroyed by flame passage
- **Later times:** observe **Landau hydrodynamic instability** causes additional wrinkling
Then strain & curvature are positively correlated



Goal: provide LES submodels with stretch rate efficiency function

Flame surface density models use the following equation for

Σ = subgrid flame surface density = flame area/volume

$$\frac{\partial \Sigma}{\partial t} + \tilde{U} \frac{\partial \Sigma}{\partial x} + \tilde{V} \frac{\partial \Sigma}{\partial y} = v_T \frac{\partial^2 \Sigma}{\partial y^2} + \underset{\uparrow}{\tilde{K}} \Sigma - \bar{M} - \bar{Q}$$

↑
flame area increase per second
(per unit volume)

K = Subgrid stretch rate
of flame area

= $(1/A) dA/dt$
= area increase per second
(per unit area)

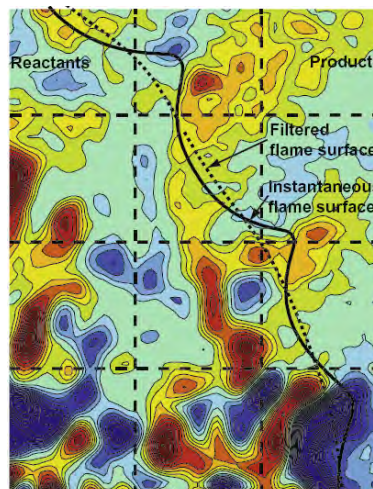
$K \Sigma = (1/A) (dA/dt) (\text{area/volume})$



59

Steinberg measured subgrid stretch rates

1. Break up the experimental field into “cells”
2. **Track eddy motions** in a Lagrangian manner
3. **Perform “filtering”** - both spatial and time averaging over each cell
4. **Correlate** the cell-averaged flame stretch rate with either the cell-averaged (u' / L) (Poinso) or the fluid strain rate S



60

How to measure K = (subgrid) stretch rate on flame surface

Why ? To predict correct degree of wrinkling, flame area
 To predict local flame speed
 To predict local extinction, overall blowout

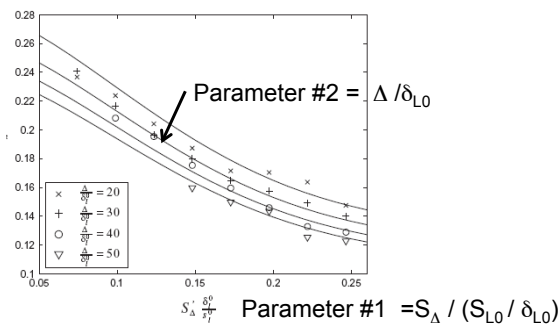
$$K = \frac{1}{A} \frac{dA}{dt} = -\hat{n} \cdot (\hat{n} \cdot \nabla) \vec{u} + \underbrace{\nabla \cdot \vec{u}}_0 + (\nabla \cdot \hat{n}) S_L$$

Stretch Rate of the
 Flame Surface Area A
 Strain Rate of Flame Surface
 Curvature of Flame Surface



Measurements relate subgrid stretch K to the resolved-scale strain rate S_{ij}

Measured Stretch Efficiency function Γ_s needed for LES



S_Δ = subgrid strain rate, related to resolved-scale velocity gradients

such as $\frac{\partial \vec{u}}{\partial x}$



LES Closure - requires three steps

Step 1. Compute subgrid fluid strain rate from energy dissipation balance

$$\frac{\nu}{2} (S'_{\Delta})^2 = \varepsilon = -\overline{u_i u_j} \widehat{S}_{ij}$$

Subgrid resolved

Step 2. Compute subgrid Reynolds stress using Smagorinsky:

$$-\overline{u_i u_j} = 2 C \Delta^2 \widehat{S}_{ij} |\widehat{S}_{ij}|$$

Step 3. Use our measurements to compute:

$$K = \text{fcn}(S'_{\Delta}, \Delta)$$

K = subgrid flame stretch rate
(on the flame surface)

S'_{Δ} = subgrid fluid strain rate
in reactants



63

What does kHz PIV tell us ?

1. **Stretch rate measurements** needed to model correct area, speeds
2. **Eddy-flame interaction measurements** are needed to assess physics of DNS and LES
3. **A method was developed** to make high-speed movies of eddy – flame interactions and to measure stretch rates
4. **“Damkohler wrinkling”** increases flame area at early times
5. **“Landau hydrodynamic instability”** increases area after eddy gone
6. **Subgrid stretch rate correlation with resolved strain rate** was measured to improve LES models



64

“3-D” eddy-flame imaging

Lay the kilohertz laser sheet horizontal

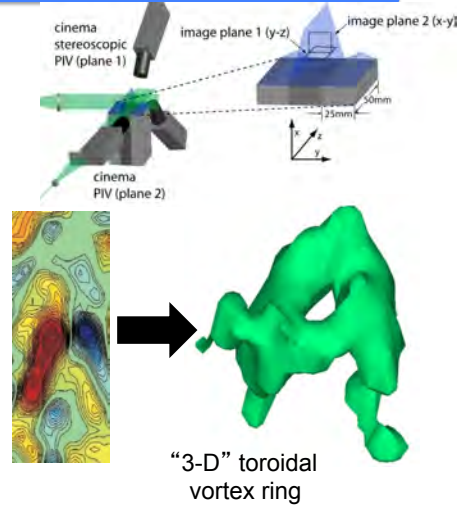
As eddies pass vertically upward through sheet:

Rapidly image eddies in the horizontal plane

Apply Taylor’s hypothesis

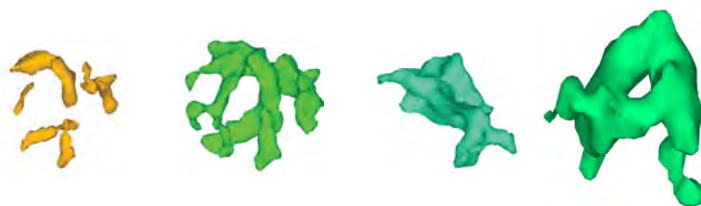
$$\frac{\partial}{\partial x} = \frac{1}{U} \frac{\partial}{\partial t}$$

Check Taylor’s hypothesis using one vertical sheet



65

KHz PIV images 3-D Vortical Structures = bundles of tubes

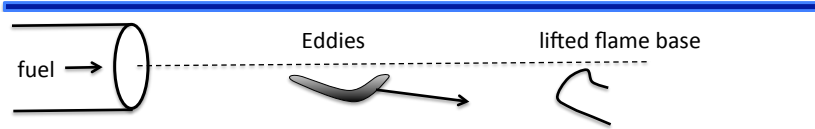


Observe Strain-Rate Structures - Sheets and Blobs



66

Kilo Hertz PIV movie of eddies entering a lifted flame base
Upatniek, Driscoll PROCI 29, p. 1867 (2002)



Particle Image Velocimetry

AE 633 W17 Driscoll

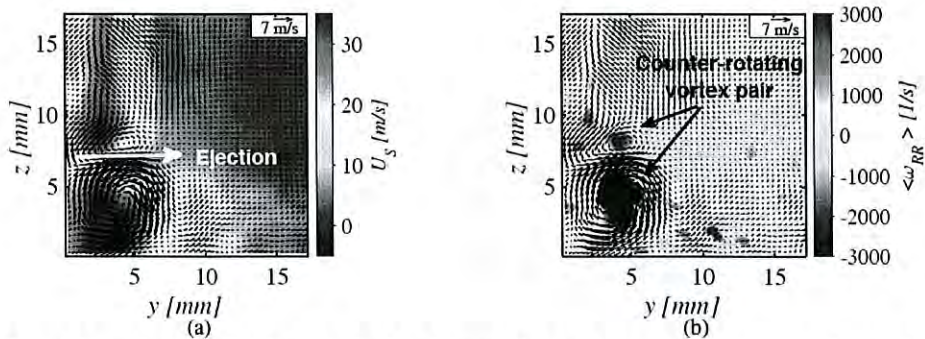
J. Westerweel, Annual Review Fluid Mech 2013, 45, 409.

LaVision sales brochures, on internet

Particle Image Velocimetry, M. Raffel, Springer Verlag Pub., 1998

1. Examples: Rohan Morajkar, Robin Hunt, Tim Wabel, Adam Steinberg
2. Setup: dual pulsed light sheets, interline transfer camera
3. Interrogation box size and Timing rules for Δt : optimal displacement Δx , out of plane motions, dynamic range
4. Field of view limitations and Freezing of particle motion, with 10 ns laser pulses
5. DaVis data analysis: spatial correlations, validation of vectors,
6. Particle seeding: particle diameter formula, particle types, types of seeders
7. Uncertainties in velocity results
10. Stereo PIV
11. Kilohertz PIV timing , two separate cameras vs one kHz interline transfer camera
12. Tomo-PIV
13. Micro PIV
14. Pulse burst laser PIV 40 kHz, but about 100 images/sample, repeat many times/s

1. Examples



Rohan Morajkar, Ph.D. thesis: Role of secondary flows on flow separation induced by shock/boundary layer interaction in supersonic inlets

2. Setup

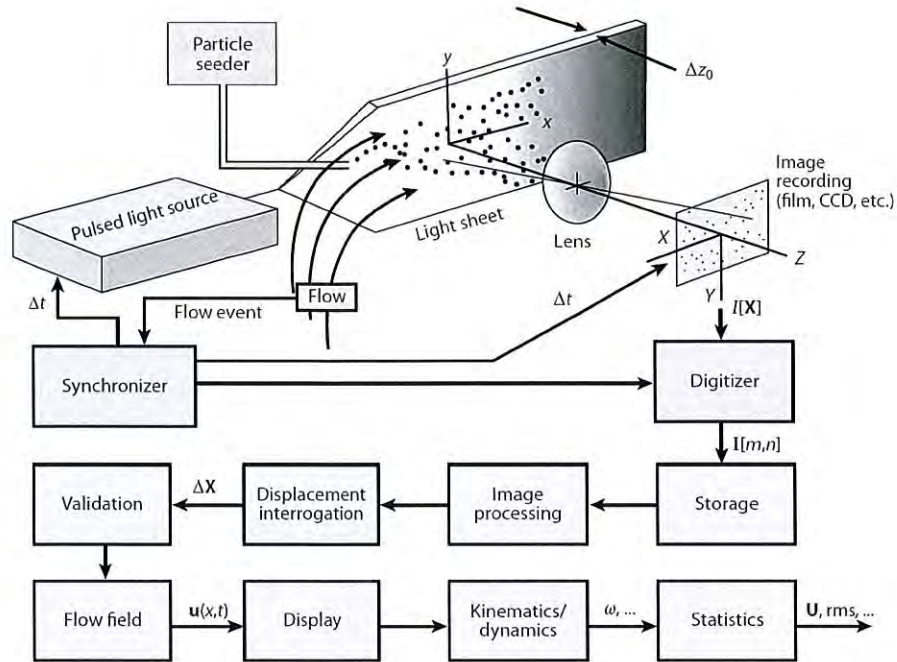
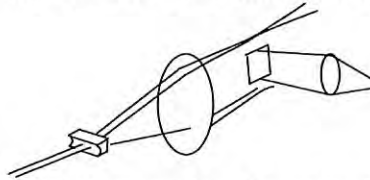


Figure 2

Elements and processes in a planar, 2D particle image velocimeter system. Figure taken from Adrian & Westerweel (2011, figure 1.2). Abbreviation: CCD, charge-coupled device.

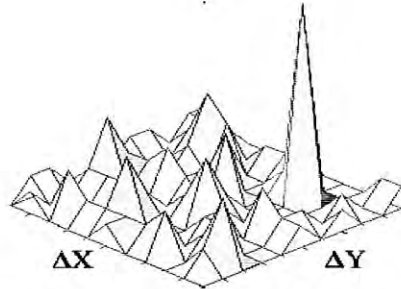
Seed the flow with 1 micron Alumina or titanium dioxide particles, or kerosene drops – that follow both the mean as well as the fluctuations in gas velocity

Combine two green laser beams at 532 nm - from two Nd:YAG Spectra Physics lasers into one beam. Pass the two beams through cylindrical optics to form a single overlapping light sheet
Fire one laser about 1 μ sec after the other laser, this difference is Δt



The cylindrical lens turns the two beams into a diverging light sheet. The spherical lens creates a non-diverging light sheet and it focuses the sheet to be thinnest at the center of the field of view.

Record the image of the particles in the first sheet; call this image 1. Then record the image of the particles in the second sheet, call this image 2. A special interline transfer camera will record both images. It uses half the pixels for the first image and the other half for the second image. That way both images are perfectly registered in space.



The highest spike is the average displacement (Δx , Δy) of the 20 particles. If the highest spike is not at least 2-3 times higher than the other spikes, the velocity of that interrogation box is not valid and no vector is computed. About 97% of the boxes have good vectors and 3% have no vector.

Record 400 images of velocity vectors; each image contains 4096 vectors on a 64 by 64 grid. See the images above taken by Rohan. Now compute the mean velocity for each interrogation box; average the 400 values (one from each image). Repeat to get r.m.s. velocity fluctuation.

Cross flow: suppose you have a swirling flow that has a velocity of U_θ perpendicular to the plane of the laser sheets. Then you have to select Δt to be less than $(U_\theta / \delta_{\text{sheet}})$ where δ_{sheet} is the laser sheet thickness. This will make sure that the particle is hit by both laser sheets before it moves from the back side to the front side of the sheet. So you typically do not want the laser sheet to be too thin; a value of δ_{sheet} of 1-2 mm is typical.

Dynamic Velocity Range: DVR = ratio of maximum to minimum velocities measurable

$$\text{DVR} = u_{\text{max}} / u_{\text{min}} = [1/3 (\text{interrogation box size}) / \Delta t] / [0.2 d_p / \Delta t]$$

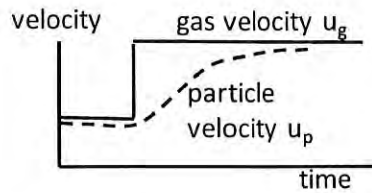
where d_p is particle diameter. The smallest average displacement of a particle that we can measure is about 0.2 particle diameters, when you average over 20 particles for $1/3$ box size = 125 microns, particle size = 2 micron, DVR = 312

Thus if the maximum velocity present is 100 m/s, min velocity measurable is 0.3 m/s

Note: if you want a larger dynamic range, you should pick a larger interrogation box size, since box size appears in the numerator of the DVR formula. However, you get less spatial resolution, since spatial resolution is your interrogation box size. You also get fewer vectors in each image.

2. Field of view limitations and freezing of particle motion

A **field of view** that we often use is 20 mm by 20 mm, in order to zoom in and see fluid and flame velocity fields down to small scales. However, you may want to look at large field of view that is, say a 1 meter by 1 meter. The first problem is that the laser energy per pulse is spread out over a 1 meter high light sheet, so the intensity of scattered light will be 50 times less than for the 20 mm by 20 mm field of view. Also, the camera has to be placed far away from the sheet, in order to focus a large (1 meter by 1 meter) field of view on to a small 1 cm by 1 cm array inside



(mass of particle) (acceleration of particle) = Stokes drag force on particle exerted by the higher speed gas

$$\rho_p \frac{4}{3} \pi \left(\frac{d}{2}\right)^3 \frac{du_p}{dt} = c_D \frac{1}{2} (u_g - u_p)^2 \frac{\pi d^2}{4}$$

now set the drag coefficient for small particles to:

$$c_D = 24 / [(u_g - u_p) d / \nu] \quad \text{so equation becomes:}$$

$$\frac{du_p}{dt} + A u_p = B \quad \text{where } A = \frac{18 \nu \rho_g}{d^2 \rho_p} \text{ and } B = \frac{18 \nu \rho_g}{d^2 \rho_p} u_g$$

Now define a new variable $y = u_g - u_p$ and plug in, separate variables and integrate. Initial velocity of gas is u_i . So:

$$u_p(t) = u_g - (u_g - u_i) \exp(-t/\tau)$$

$$\tau = \left[\frac{18 \nu \rho_g}{d^2 \rho_p} \right]^{-1} \quad \text{is the time constant}$$

We require that particles must follow flow to within 1% for a frequency of flow oscillation:

$$f = 1 / t$$

$$\frac{(u_g - u_i)}{u_g} = 0.01 \quad \text{Plug these two in to get the required PIV particle diameter:}$$

$$d = \left[\frac{18 \nu \rho_g}{(-\ln(0.01) \rho_p)} \frac{1}{f} \right]^{1/2} \quad \text{higher frequencies require smaller particle diameters}$$

ex. Alumina density = 3700 kg/m^3 , air density = 1.2 kg/m^3 $\nu = 0.15 \text{ cm}^2/\text{s}$
 suppose an eddy of size 1.5 mm undergoes a velocity fluctuation of $u' = 15 \text{ m/s}$,
 this causes a fluctuation of frequency $15 \text{ m/s} / 1.5 \text{ mm} = 10 \text{ kHz} = f$
 Plug this into the formula above to get particle diameter $d = 1.4 \text{ microns}$

Some researchers define the Stokes number to be:

$$St = \tau / (L / U) \quad \text{where } \tau \text{ is the time constant defined above.}$$

Microgrit: <http://products.stutzcompany.com/item/lapping-compounds/sub-micron-aluminum-oxide-polishing-powder/2500>

Zeeospheres: <http://www.palmerholland.com/Principals/25/Details>

Uncertainty

The actual time between laser pulses Δt must be carefully measured using a high speed oscilloscope because the value that the computer sets for Δt may not be the actual value. With a bright flame present, Jacob Temme used a 532 nm, 2 nm FWHM band pass filter in line with a mechanical shutter that reduced the exposure time of the second PIV frame from 100 ms to approximately 5 ms.

Statistical uncertainty: should my mean values be averaged over 400 images or 4000 images ?

Statistical uncertainty depends on the number (N) of PIV images used to determine the mean values. Another factor is the interrogation box size. In Ethan Eagles thesis N was selected to be 1700 images and the typical interrogation box size was 0.43 mm by 0.43 mm. Statistical analysis [27] shows that the 98% confidence interval (CI98) is given by:

$$CI_{98} = \bar{U}_e \pm 2.33 \frac{\sigma_u}{\sqrt{N}}$$

(see Moore, DS, McCabe, GP (1999) Introduction to the practice of statistics. W.H. Freeman Co. NY.)

One has 98% confidence that the mean from averaging of N PIV images will differ from the expectation value \bar{U}_e by the amount $2.33 \sigma_u / \sqrt{N}$. The expectation value \bar{U}_e is the mean that would be computed if an infinite number of images were collected. In Ethan's free stream, where the standard deviation (σ_u) is measured to be 0.011 (600 m/s). Inserting this value indicates that there is 98% confidence that that ensemble mean lies within 0.06% of the expectation value, so there is no reason to average over more than 1700 images in the free stream. There is more uncertainty in the boundary layer where the standard deviation is larger.

Velocity bias:

Near a wall, the low velocity gas will not contain many particles, but when higher velocity gas gets near the wall it will contain more particles. So measurements near a wall can be biased and the measured velocity will be higher than the actual velocity.

Velocity measurements

Pitot probe - must know flow direction, must know gas density, mean velocity only, perturbs recirculation zones and flames

Hot wire anemometry - averages over two directions, must know gas density, limited to non-reacting, perturbs recirculation zones

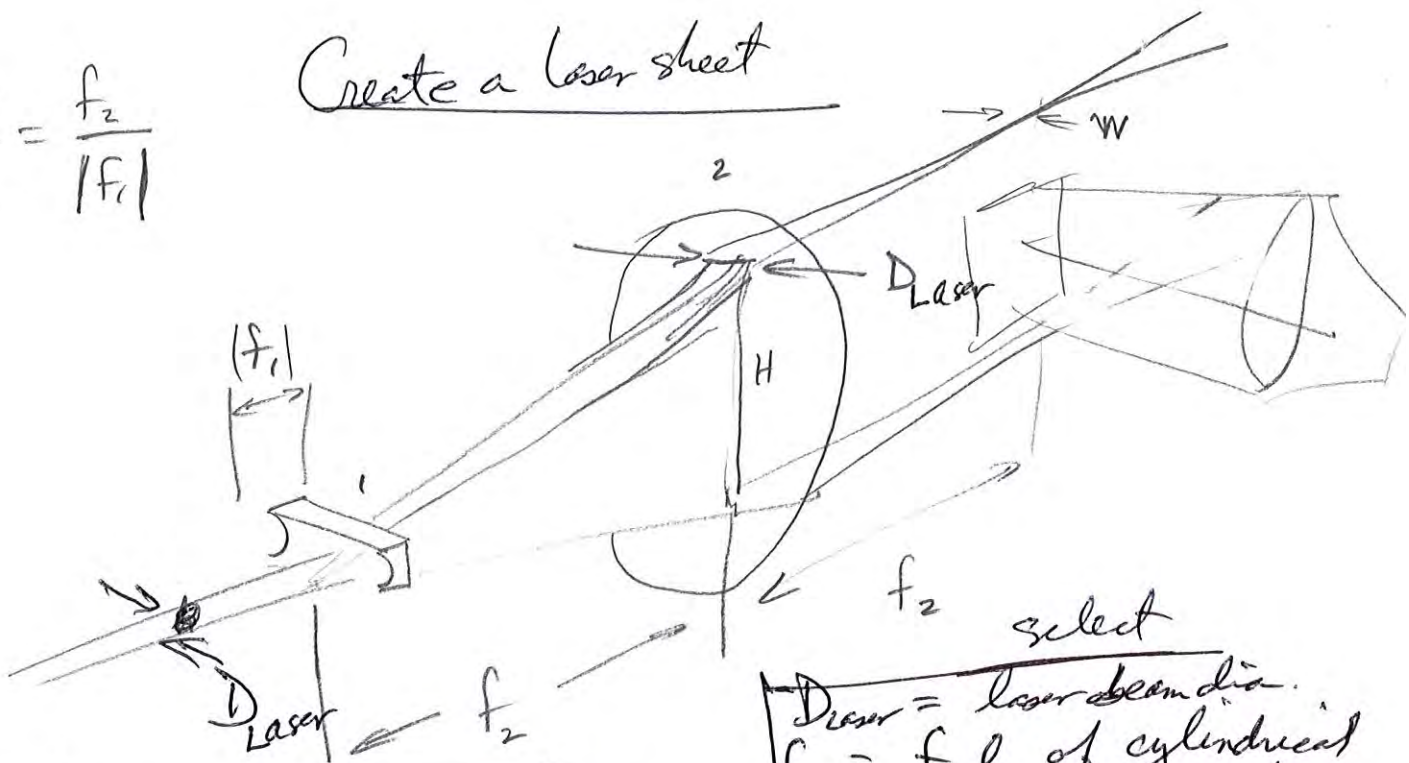
Laser Velocimetry - gives time history of velocity at a point, must be able to seed flow with particles, requires optical access, lasers can be disturbed by windows, shocks

PIV: stereo, kHz, tomo: time history of velocity in a sheet, must be able to seed flow with particles, requires optical access, some flames are too bright

Doppler Shift of emitted light - in supersonic flow the emitted light from fluorescence or hot gases is Doppler shifted and this shift tells you the gas velocity; good for Electric Propulsion

Create a laser sheet

$$\frac{H}{h} = \frac{f_2}{|f_1|}$$



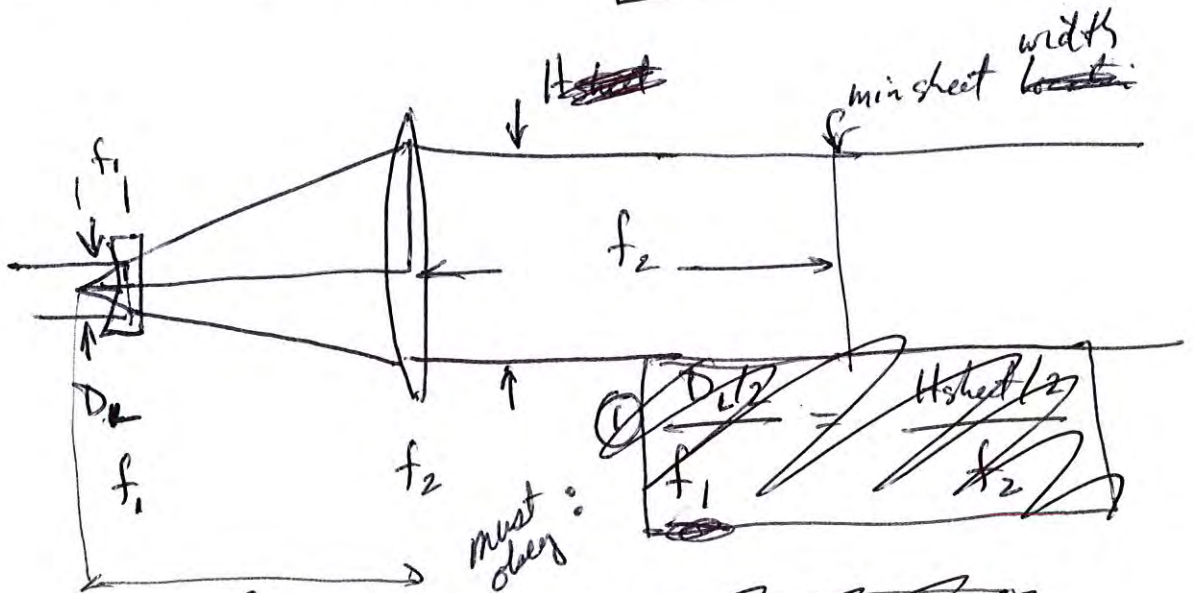
width of sheet at center of field of view

$$W = \frac{4 \lambda f_2}{\pi D_{\text{Laser}}} \quad (1)$$

D_{Laser} = laser beam dia.
 f_1 = f.l. of cylindrical lens
 f_2 = f.l. of spherical lens
 λ = wavelength of laser

$$H = D_{\text{Laser}} \left(\frac{f_2}{f_1} \right) \quad (2)$$

Q mechanic looks 1 molecule

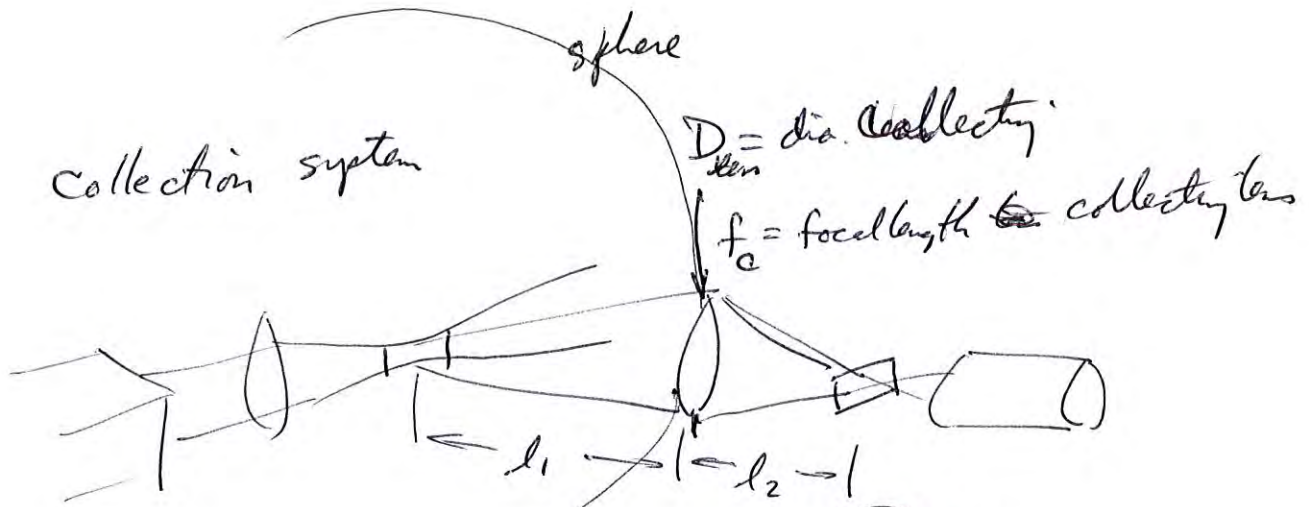


given laser diameter $D_L = 2\text{mm}$
 want $H = 35\text{mm}$
 $W = 200\mu\text{m}$

$$W = \frac{4 \lambda f_2}{\pi D_{\text{Laser}}} \quad (2)$$

8-12
 $W = \text{FWHM of } 0.1\% \text{ of center line intensity}$

collection system



signal collected $\propto \frac{A_{lens}}{A_{sphere}} = \frac{D_{lens}^2}{4l_1^2}$

if you collect all the light $A_{lens} = 4\pi l_1^2$, $\Omega = \frac{4\pi l_1^2}{l_1^2} = 4\pi \text{ sterad.}$

$$\frac{1}{l_1} + \frac{1}{l_2} = \frac{1}{f_c}$$

$$F\# \text{ lens} = \frac{f_c}{D_L}$$

best you can do is about F# = 1.2

make l_1 as small as possible } maximize Ω
 make D_L as large as possible }

8-13

~~4-11~~

4-113 ~~3-10~~

focusing formulas

$$\frac{1}{l_1} + \frac{1}{l_2} = \frac{1}{f_2}$$

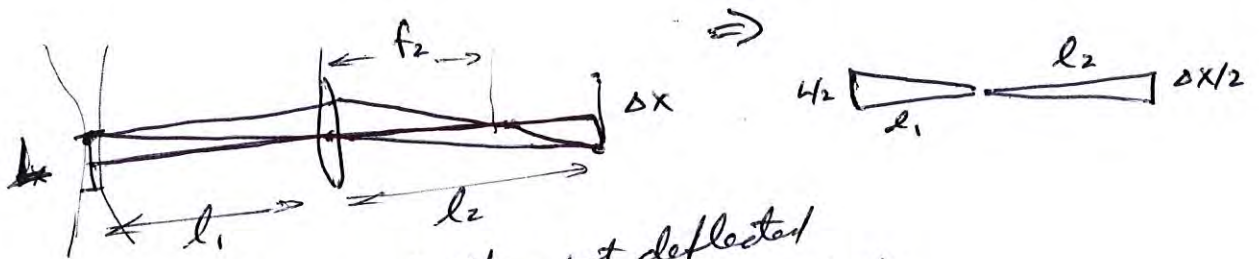
$f_2 =$ focal length of lens 2

ex $f_2 = 100 \text{ mm} = 10 \text{ cm} = 4''$

$\Delta x =$ slit width

$L =$ length along laser beam

if $l_1 = 8'' = 200 \text{ mm}$
 $\therefore l_2 = 8'' = 200 \text{ mm}$



ray going thru center of lens not deflected
 ray that is horizontal goes through focal pt.

$$\therefore \frac{\Delta x}{l_2} = \frac{L}{l_1}$$

from similar triangles

if $l_1 = l_2 = 200 \text{ mm}$

$\Delta x = L$ slit width = length along laser

= spatial resolution

to get most light collected

a) maximize Ω , want large $(D_L / l_1) =$ "fast lens"

big D_L (expensive)

small $l_1 \rightarrow$ small f focal length

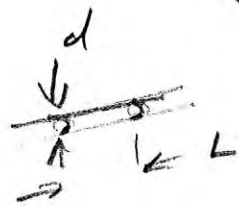
typ $f:1.4$ best
 3-14

$f \# = \frac{f}{D_L} = \frac{5.6''}{4''}$
 of a lens

~~3-14~~

Single point LIF - focusing

refer to our sketch of the laser



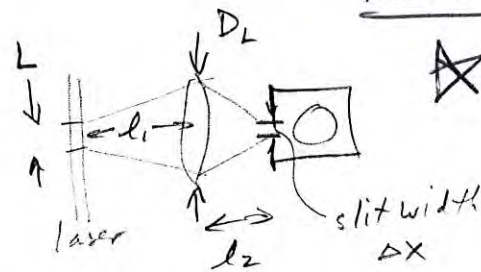
extra

(vi) $V_c = \frac{\pi d^2}{4} \cdot L$ scattering volume

(vii) $I_\nu = \frac{E_L}{(\frac{\pi d^2}{4}) \Delta t \Delta \nu} = \frac{\text{laser energy}}{(\text{area of beam}) (\text{pulse duration}) (\text{laser linewidth})}$

(viii) collection solid angle

$$\Omega = \frac{\pi D_L^2}{4 l_1^2}$$



eliminate l_2 : $\frac{1}{l_1} + \frac{1}{l_2} = \frac{1}{f}$

and $\frac{l_1}{L} = \frac{l_2}{\Delta x}$

normally $l_1 \gg l_2 \therefore l_2 \approx f$

$\therefore l_1 = l_2 \frac{L}{\Delta x} = f \frac{L}{\Delta x}$

(ix)

eliminate D_L :

$$FN \equiv \frac{f}{D_L} = \text{"f-number of lens"} = 1.2 \text{ typ.}$$

(x) so $D_L = f / FN$

now combine eqns v, vi, vii, viii, ix, x:

~~1-29~~ 8-15

~~1-29~~

Stereo PIV

- to measure three velocity components: (u, v, w) in the (x, y) laser sheet plane
- from the image you can compute u', v', w' and $\frac{\partial u}{\partial x}, \frac{\partial u}{\partial y}, \frac{\partial v}{\partial x}, \frac{\partial v}{\partial y}, \frac{\partial w}{\partial x}, \frac{\partial w}{\partial y}$
- but you cannot measure derivatives in the z direction, unless you create two stereo PIV planes parallel to each other

From the book PIV by M Raffel: you set up two cameras as shown below:

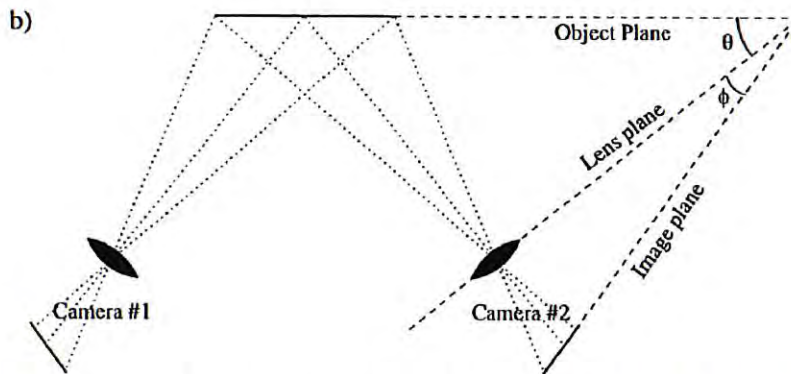


Fig. 7.1. Basic stereoscopic imaging configurations: a) lens translation method, b) angular lens displacement with tilted back plane (Scheimpflug condition)

Raffel defines the particle displacement in the light sheet as $D_x = X'_i - X_i$ and $D_z = Z'_i - Z_i$. The displacement in the recording plane of the CCD camera are: $x'_i - x_i$ and $z'_i - z_i$.

Then he defines the magnification to be M , as he shows below:

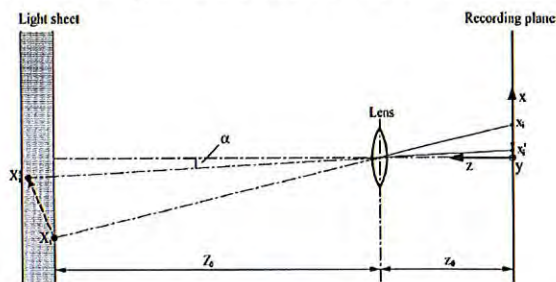


Fig. 2.28. Imaging of a particle within the light sheet on the recording plane

particle moves distance D_x and D_z in laser sheet

Next he relates the displacements in the laser sheet to displacements in the recording plane by equations 7.1 and 7.2 below:

7.1.1 Reconstruction geometry

This section describes the geometry necessary to reconstruct the three-dimensional displacement field from the two projected, planar displacement fields. Past descriptions of stereoscopic PIV imaging systems assume a symmetric configuration [90, 107, 112, 113, 117]. In the present case the two cameras may be placed in any desirable configuration provided the viewing axes are not collinear.

In section 2.4.3 we determined the basic equations- equation (2.19) and equation (2.20)- for particle image displacement assuming geometric imaging:

$$x'_i - x_i = -M \left(D_X + D_Z \frac{x'_i}{z_0} \right) \quad (7.1)$$

$$y'_i - y_i = -M \left(D_Y + D_Z \frac{y'_i}{z_0} \right) \quad (7.2)$$

Now he defines the angles α and β for each camera:

In the following we will use the angle α in the XZ plane between the Z axis and the ray from the tracer particle through the lens center to the recording plane (see figure 2.28). Correspondingly, β defines the angle within the YZ plane.

$$\tan \alpha = \frac{x'_i}{z_0}$$

$$\tan \beta = \frac{y'_i}{z_0}$$

The velocity components measured by the right camera are given by:

$$U_r = -\frac{x'_i - x_i}{M \Delta t}$$

$$V_r = -\frac{y'_i - y_i}{M \Delta t}$$

The velocity components for the left camera U_l and V_l can be determined accordingly. Using the above equations, the three velocity components (U, V, W) can be reconstructed from the measured values. For $\alpha, \beta \geq 0$ we obtain:

$$U = \frac{U_r \tan \alpha_l + U_l \tan \alpha_r}{\tan \alpha_r + \tan \alpha_l} \quad (7.3)$$

$$V = \frac{V_r \tan \beta_l + V_l \tan \beta_r}{\tan \beta_r + \tan \beta_l} \quad (7.4)$$

$$W = \frac{U_l - U_r}{\tan \alpha_r + \tan \alpha_l} \quad (7.5)$$

$$= \frac{V_l - V_r}{\tan \beta_r + \tan \beta_l} \quad (7.6)$$

Note: from the right camera the velocities are U_r and V_r and the angles are α_r, β_r
from the left camera the velocities are U_l and V_l and the angles are α_l, β_l

Therefore Eqns. 7.3 to 7.6 give the desired three velocities U, V, W

$$Dz = \text{displacement in } z \text{ (out of plane)}$$

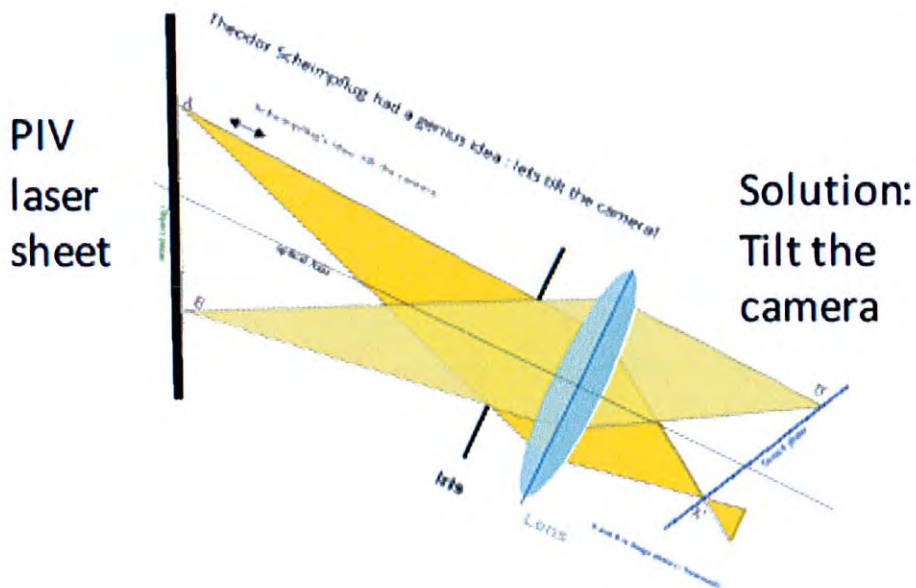
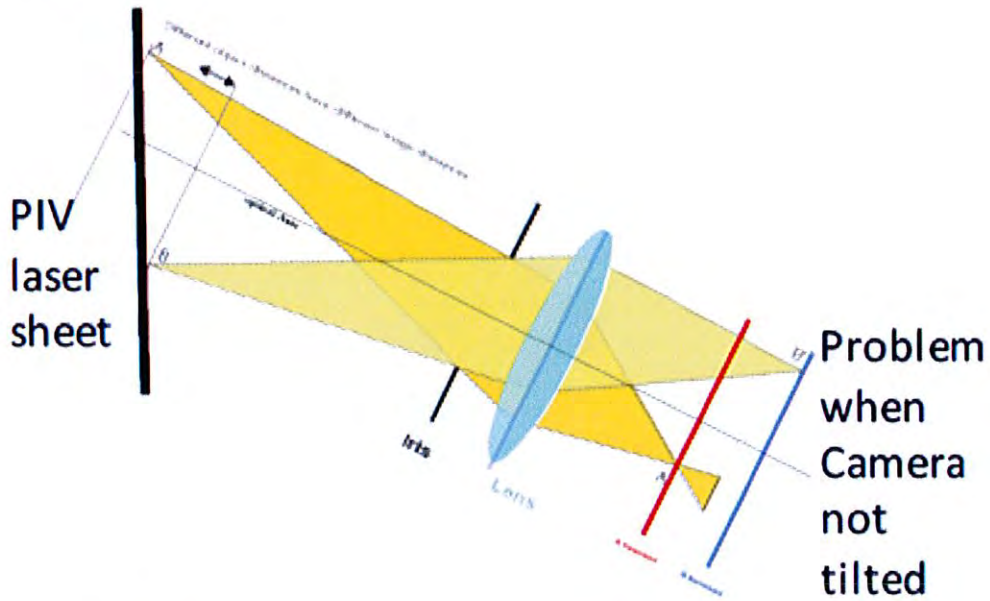
$$Dz = z'_i - z_i$$

$$W = \frac{(z'_i - z_i)}{\Delta t}$$

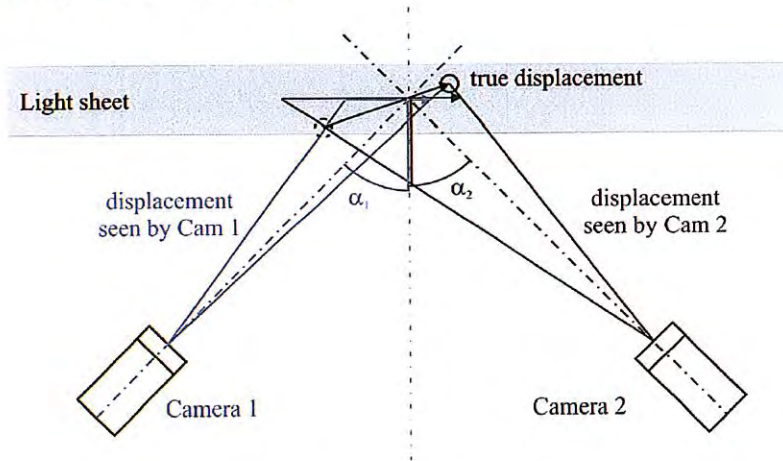
Scheimpflug principle

Normally, the focus plane is 90 degree to the optical axis. This is due to symmetry reasons.

A problem arises when two objects have so different distances, that they can not be focussed at the same time.

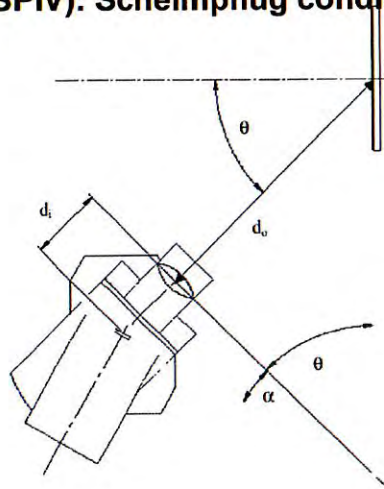


Stereoscopic PIV (SPIV)



True 3D displacement ($\Delta X, \Delta Y, \Delta Z$) is estimated from a pair of 2D displacements ($\Delta x, \Delta y$) as seen from left and right camera respectively

Stereoscopic PIV (SPIV): Scheimpflug condition



Kilohertz PIV

Ansís Upatnieks (2001) Adam Steinberg Yuntao Chen Aaron Skiba at Michigan

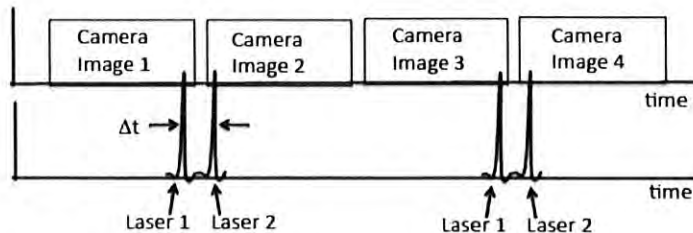
One Phantom v9.1 high rep rate 8 kHz camera, operated in frame straddling mode
 One Quantronix Duo: contains two Nd:YAG lasers, one pulses at 4 kHz, other pulses at 4 kHz

Yuntao Chen, Comb Flame 174, 120

The kHz PIV laser beam is produced by a 532 nm Quantronix Hawk- Duo Nd:YAG laser at a sustained frequency of 8 kHz at 10 mJ/pulse. The beam is contracted by cylindrical lens (CVI-SCX-50.8-254.3- UV-355-532). A laser sheet with a height of 20 mm is obtained above the burner surface. The PIV camera (Phantom v9.1) is coupled with a Nikkor 105 mm f2.8 macro lens and a narrow band-pass 532 nm filter (Andover 532FS02-50). It is synchronized with the laser pulse at 8 kHz, at which frequency the resolution of the camera is 384 × 384 pixels, yielding a scale of 39 μm per pixel for a field of view of 15 mm × 15 mm. The resolving power of the camera is determined by a standard 1951 USAF target to be 9 lpmm. With frame-straddling, the the PIV signal is obtained at 4 kHz.

After processing the PIV images in LaVision Davis software with a 64 × 64 pixels window and 50% overlapping ratio, a matrix of 12 × 12 vectors per frame was obtained. All 144 vectors were averaged in axial and radial direction, and the average axial and radial velocity were estimated

Frame Straddling to do kHz PIV with only one camera – do not have to do tedious registration of two separate cameras



$\Delta t = \Delta x / U$ want $\Delta x = \text{distance particle moves} = 1/3 \text{ interrogation box size}$

Interrogation box = one PIV velocity vector = 0.3 mm
 so $\Delta x = 0.1 \text{ mm}$

If $U = 50 \text{ m/s}$, then $\Delta t = 2 \mu\text{s}$

camera must turn off, then turn on - in less than 2 μs

Handwritten notes:
 8000 frames/sec
 8000 pulses/sec =
 (one pulse / frame)
 4000 pulses/sec Laser 1
 4000 pulses/sec Laser 2

Handwritten equation:

$$\Delta t = \frac{\Delta x}{U} = \frac{1/3 (\text{box})}{U}$$

Handwritten calculation:

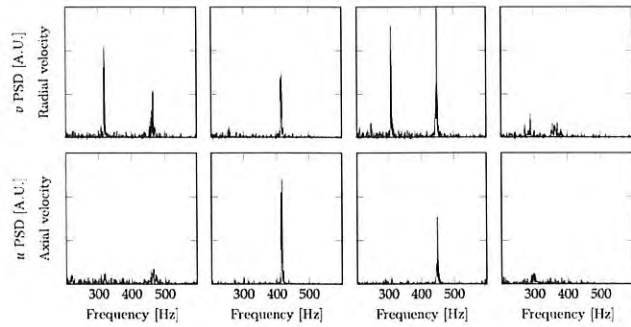
$$\text{box} = 0.3 \text{ mm}$$

$$\Delta x = 0.1 \text{ mm}$$

$$\Delta t = \frac{0.1 \text{ mm}}{50 \text{ m/s}}$$

$$= 2 \mu\text{s}$$

During a combustion instability, kHz PIV gives the spectrum, the magnitude and the phase angle of velocity oscillations



Temme, Comb Flame 161, 958 – velocity exiting TAPS injector is oscillating

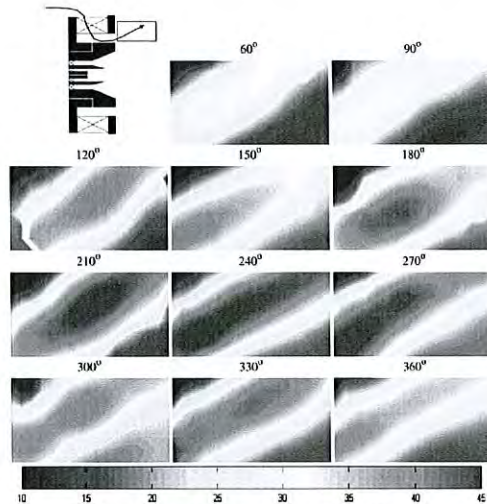
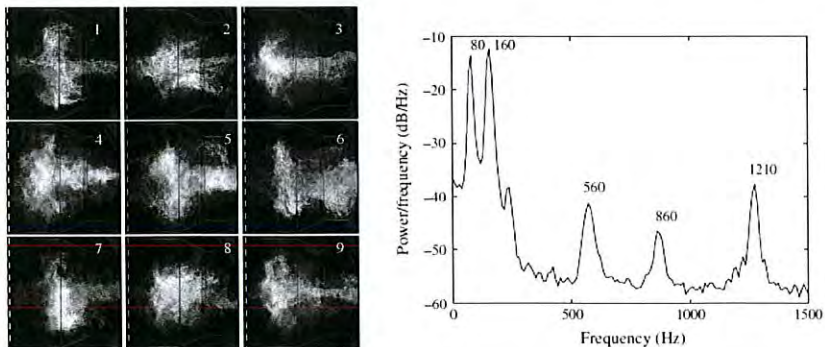


Fig. 8. Phase-averaged inlet velocity fields with values of phase angle marked. Color scale is axial velocity (U) in m/s. Note that lower velocities occur at a phase angle of 90° and higher velocities occur at 270° . Image size is 4 mm by 8 mm located near the outer swirler as indicated. Case 1.

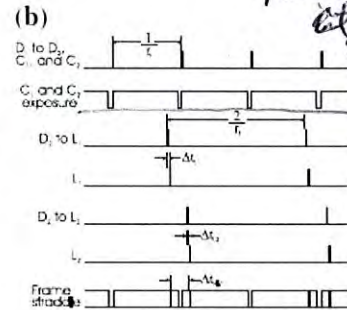
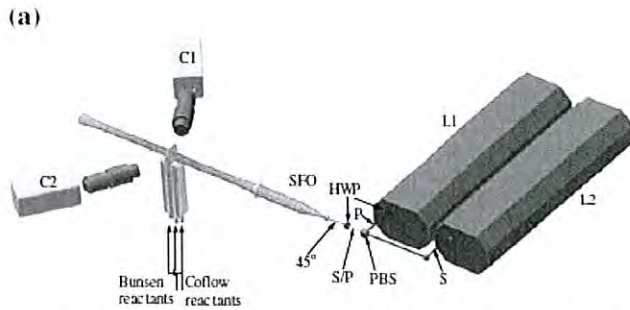
Oscillating velocity causes flame liftoff to oscillate, causing pressure spectrum to have spikes



If you want kHz Stereo PIV, then you will need **two** high speed cameras

Steinberg, Expts Fluids

Same as previous picture but two cameras recording at same time

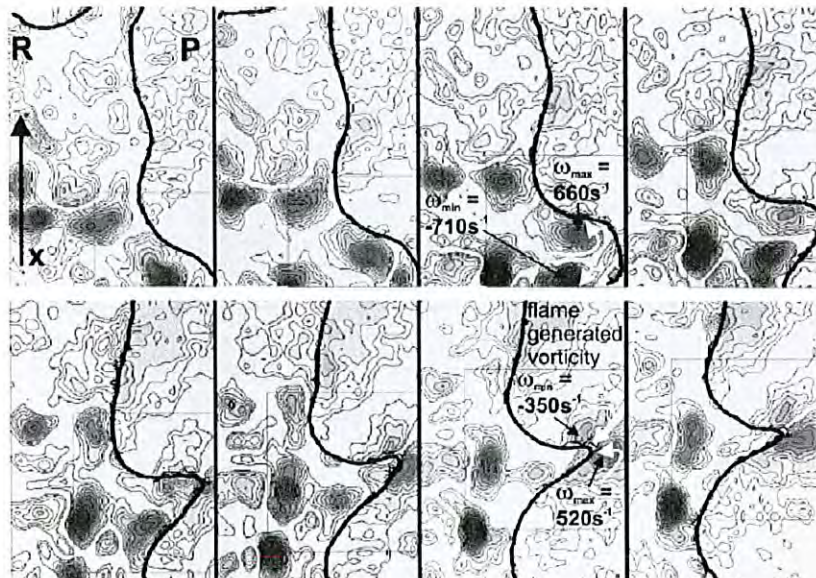


System layout. Polarization indicated. HWP - Half wave plate. PBS - Polarizing beam splitter, SFO - Sheet forming optics.

Timing diagram. D_i are delay generator signals.

Table 1 CS-PIV parameters

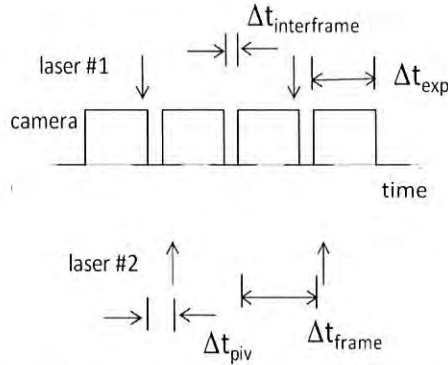
Parameter	Value
Camera frame rate	2,222 Hz
Temporal resolution	0.9 ms
Δt_{PIV}	40 μ s
Stereo angle	35°
Camera resolution	672 px \times 1,120 px
Field of view	12.8 mm \times 18.2 mm
Interrogation box	280 μ m
Vector spacing	140 μ m
Seed material	Silica coated TiO ₂
Nominal seed diameter	0.15 μ m



videos of turbulent eddies passing through a premixed turbulent flame

Timing of kilohertz PIV - camera requirements J. F. Driscoll, June 18, 2012

We need one kHz camera and a Duo KHz laser (two lasers) :



same figure as before

Fig. 1. Optimum timing of kilohertz PIV

Frame one records laser pulse #1, frame two records laser pulse #2 and so on.

We want Δt_{piv} to be short, so camera must have an interframe time of less than:

$$\Delta t_{interframe} < \Delta t_{piv} = \Delta x_p / U$$

interframe time limits speed flow velocity you can look at

$\Delta t_{interframe}$ = minimum time between frames (see Figure 1) =
 = 0.25 μs (Photron SA5), 0.5 μs (Phantom V1610), 2 μs Photron SAX and Phantom 9.1

Δt_{piv} = PIV delay time between laser 1 and laser 2, given by Eq. 1

Δx_p = particle displacement during $\Delta t_{piv} = 1/3^{rd}$ of interrogation box size

U = gas velocity Δt_{frame} = framing time = 1/ (rep rate of camera)

$\Delta t_{interframe} = 0.25 \mu s$
 $\Delta x_p = 0.1 mm, box = 0.3 mm$

We want to see some "event" evolve during N velocity images before it is convected out of our field of view (FOV). Ex: $N = 5$ gives five velocity images of event with a FOV = 12 mm (12 mm by 12 mm image)

$$\text{Camera Rep rate} = (2 U N) / (FOV) = 1 / \Delta t_{frame}$$

$U_{max} = \frac{0.1 mm}{0.25 \mu s} = 400 m/s$

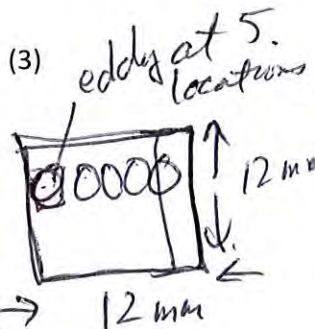
Factor of 2 is in Eq. 2 because we need 2 camera images to get one velocity image, so camera must run at twice the rep rate as the lasers

$$\text{Laser rep rate} = \frac{1}{2} \text{ Camera rep rate}$$

FOV = field of view in flow direction

N = number of velocity images you want before event is convected out of the field of view

Δt_{exp} = exposure time of camera = not important if you want to minimize Δt_{piv}



1

8-23

$$\tau = \text{transit time} = \frac{12 mm}{U} = \frac{FOV}{U}$$

$$\text{frame time} = \frac{\tau}{5} = \frac{FOV}{5U}$$

Our Michigan kilohertz PIV system (Yuntao Chen)

Interrogation box size	=	200 microns
Δt (PIV) =		10 microsec, OK, is larger than interframe time of 1 microsec
U =		10 m/s
Δx =		100 microns = $\frac{1}{2}$ box size
Δt_{frame}	=	125 microsec (8000 frames/sec, 4000 PIV velocity images/s)
N		= 5 velocity images / transit time of FOV
FOV =		25 mm
Reqd camera rep rate		$2 (10 \text{ m/s}) (5) / (25 \text{ mm}) = 4000 \text{ frames/s}$, we do 8000

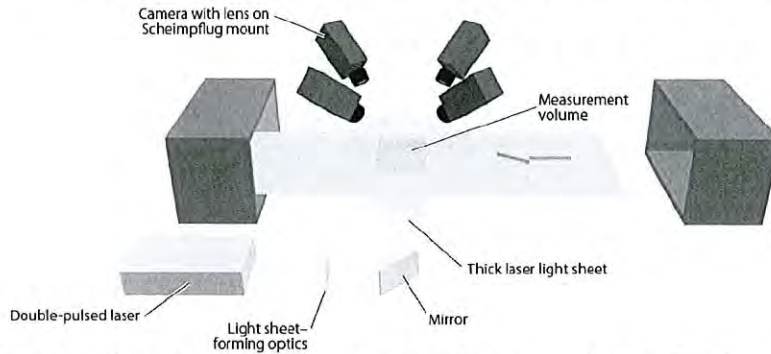
Our measured interframe time (Yuntao): Phantom v9.1 (old one): 3 micro seconds

Phantom v711 (new one): 320 nano seconds

Note: adding a second PIV camera will not allow us to go to larger gas velocities or larger framing rates but will allow for stereo PIV

2. TOMOGRAPHIC PIV

Tomographic PIV (Figure 4) was recently introduced as a promising new method for measuring the instantaneous 3D velocity field (Elsinga et al. 2006). In this approach, the tracer particles are



slab =
 16.5 mm
 12.3 mm
 2.5 mm

The variety of applications achieved to date clearly demonstrates the versatility of tomographic PIV, perhaps explaining its growing importance. The technique has been used in different flow facilities covering a velocity range from only a few micrometers per second in a water tank (Worth & Nickels 2011) to 510 m s^{-1} in a supersonic wind tunnel (Humble et al. 2009, Elsinga et al. 2010). Furthermore, it can measure anywhere from millimeter-sized volumes when employing a microscope objective with four ports for imaging (Kim et al. 2011) to meter-sized volumes, as demonstrated in a large-scale convection cell by Kühn et al. (2011). Extensions to tomographic TR-



slab

Principle of Tomographic PIV

Tracer particles within the measurement volume are illuminated by a high power pulsed light source and the scattered light pattern is recorded simultaneously from typically 4 viewing directions using CCD cameras. The 3D particle distribution is reconstructed by a tomographic reconstruction algorithm (MART) as a 3D light intensity distribution for each voxel. The particle displacement within a chosen interrogation volume is then obtained by the 3D cross-correlation of the reconstructed particle distribution at the two exposures, using advanced iterative multi-grid algorithms with deformed interrogation windows. Calibration errors are automatically corrected by the patented LaVision **Volume Self-Calibration** procedure.

like MRI

Tomographic-PIV

Tomographic-PIV is a measurement technique that allows resolving the particle motion within a three-dimensional measurement volume without the need to detect individual particles. This recently developed method (Elsinga et al., 2006) is based on the simultaneous view of the illuminated particles by digital cameras placed along several observation directions similarly to the stereoscopic PIV configuration. The innovative element of the technique is the tomographic algorithm used to reconstruct the 3D particle field from the individual images. The 3D light intensity distribution is discretized over an array of voxels and then analyzed by means of 3D cross-correlation interrogation returning the instantaneous three-component velocity vector field over the measurement volume.

Tomographic-PIV has been developed for research laboratory applications and its extension to industrial wind tunnel environments so far has not been performed. Despite its recent introduction, by early 2007 the technique has already been successfully applied in both air and water flow measurements within about 10 experiments conducted over several European laboratories (TU Delft, LaVision, DLR Göttingen, TU Braunschweig, Poitiers University). The requirement to implement time-resolved Tomographic-PIV is the same as for planar PIV, which has been already verified with both low repetition-rate Tomographic-PIV measurements in water flows and a high-repetition rate boundary layer experiment in air flow.

The most important limiting factors are the extent of the measurement volume depth (typical depth-to-width ratio 0.25), the power required for volume illumination (typically 5 times higher than for a stereo-PIV experiment), the time required for digital evaluation of recordings (nowadays a few hours per snapshot) and the associated data storage (typically 10 times larger than for planar PIV). Last but not least a slightly extended optical access is required with respect to stereo-PIV because the viewing directions typically cover a solid angle, although the linear configuration is also a possible option if required.

(slab)

Its working principle is that, tracer particles immersed in the flow are illuminated by a pulsed light source within a three-dimensional region of space (Figure 16, Raffel et al., 2007). Particle images are recorded in focus from several viewing directions using CCD cameras. The Scheimpflug condition between the image plane, lens plane and the median object-plane has to be fulfilled, which is practically achieved by means of camera-lens tilt mechanisms with the rotation axis freely adjustable. The latter condition is not sufficient to ensure that particle images are in focus over the entire depth of the measurement volume. This requirement is satisfied with an appropriate depth of focus by selecting an appropriate lens aperture.

The reconstruction of the 3D object from the digital images requires prior knowledge of the mapping function between the image planes and the physical space. This is achieved by means of a calibration procedure similar to that of stereoscopic PIV. However the procedure requires such mapping function to be defined onto a volumetric domain as opposed to that used for planar stereo-PIV. The requirement for a precise alignment between calibration and measurement plane is not a restriction in this case since no such plane exists for the tomographic technique, which makes it easier to implement the experiment with respect to laser light positioning. However, the requirement for a precise relative position between cameras for the tomographic technique (one-fifth of the particle image diameter) is much more stringent than that for planar stereo PIV (Raffel et al., 2007).

8-26

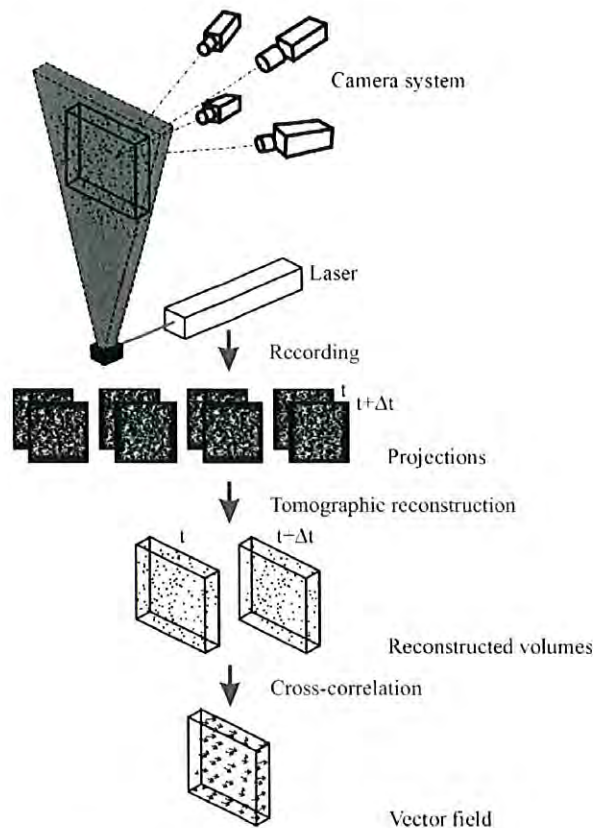


Figure 16: Principle of Tomographic-PIV.

Although recently introduced the tomographic PIV technique has been applied to several flow conditions from more academic configurations such as circular cylinder wakes to increasingly challenging topics such as low speed turbulent boundary layers and shock wave boundary layer interaction at Mach 2. The technique as also been implemented in conjunction with high repetition rate hardware for the time resolved measurement of boundary layer transition to turbulence described in details in the section of PIV applications.

Micro-PIV

Many areas in science and engineering are existing where it is important to determine the flow field at the micron scale. Industrial applications of micro-fabricated fluidic devices are present in the aerospace, computer, automotive, and biomedical industries. In the aerospace industry, for instance, micron-scale supersonic nozzles measuring approximately $35\mu\text{m}$ are being designed for JPL/NASA to be used as microthrusters on micro-satellites and for AFOSR/DARPA as flow control devices for palm-size micro-aircraft (Bayt and Breuer, 2001). In the computer industry, inkjet printers, which consist of an array of nozzles with exit orifices on the order of tens of microns in diameter, account for 65% of the computer printer market (Bayt and Breuer, 2001). The biomedical industry is currently developing and using microfabricated fluidic devices for patient diagnosis, patient monitoring, and drug delivery. The i-STAT device (i-STAT, Inc.) is the first microfabricated fluidic device that has seen routine use in the medical community for blood analysis. Other examples of microfluidic devices for biomedical research include microscale flow cytometers for cancer cell detection, micromachined electrophoretic channels for DNA

fractionation, and polymerase chain reaction (PCR) chambers for DNA amplification (Northrup, et al., 1995). The details of the fluid motion through these small channels, coupled with nonlinear interactions between macromolecules, cells, and the surface-dominated physics of the channels create very complicated phenomena, which can be difficult to simulate numerically.

In 1998 Santiago et al. (1998) demonstrated the first μ PIV system—a PIV system with a spatial resolution sufficiently small enough to be able to make measurements in microscopic systems. This first μ PIV system was demonstrated measuring slow flows—velocities on the order of hundreds of microns per second—with a spatial resolution of $6.9 \times 6.9 \times 1.5 \mu\text{m}^3$ (Raffel, et al. 2007). The measurement principle is based on Particle Image Velocimetry for large scale applications. The optical velocimetry technique uses conventional microscopy and digital imaging methods for the quantitative determination of two-component velocity data in a two-dimensional measurement plane. Depending on the choice of microscope objectives regions of investigation range from $1 \times 1 \text{ mm}^2$ for a $5\times$ magnification lens to $50 \times 50 \mu\text{m}^2$ for a $100\times$ magnification lens. Within the region of interest velocity information spacing is of order $1 \mu\text{m}$. Spatial resolution up to a few 100 nm can be achieved (refer to review paper by Lindken et al., 2009).

For the optical measurement technique a transparent working medium and optical access to the area of investigation is needed. The flow is seeded with tracer particles for the visualization of the motion of the fluid. Ideally the tracer particles should follow the flow. This is achieved by matching the density of the fluid and of the flow-tracing particle or by the use of very small particles.

A volume of liquid with tracer particles is illuminated and observed with the aid of a microscope objective. For volume illumination all tracer particles emit light, but only the light originating from tracer particles in the focus plane of the microscope objective (and of those slightly out of focus) is collected by the objective lens and the position of those tracers is captured on a digital camera at one instant of time t_1 . After a short time interval Δt the tracer particles are illuminated again and their position is recorded on a second digital image at time $t_2 = t_1 + \Delta t$. Please note that during the imaging process the three-dimensional particle positions are projected onto a two dimensional image plane where they form a two-dimensional particle image pattern. When there is a flow the positions of the tracer particles have slightly changed in the two consecutive recordings. The tracer particles with velocity v have shifted by a certain displacement Δs and hence, $v = \Delta s / \Delta t$. The two digital images are sent to a PC, where they are stored together with the time information. In a successive evaluation step the particle displacement Δs is digitally evaluated from the image pair.

For the purpose of data acquisition, a typical μ PIV realization consists of a pulsed light source that is synchronized with the digital camera by a timing unit. The synchronization is done in a way that the first light pulse is set at the end to the first camera recording and the second pulse is set at an arbitrary time in the second recording. In this way the time interval Δt is independent of the camera frame rate, but defined by the time interval between the two synchronized light pulses. The time interval can now be adjusted to the flow conditions.

Frequency doubled Nd:YAG lasers at 532 nm wavelength of the laser light are a standard pulsed light source for PIV. For μ PIV applications less than 10 mJ of laser power per pulse is sufficient. Double cavity lasers consist of two lasers that can be triggered independently and of a beam-combining optic for the adjustment of the overlap of the two laser beams. Frequency-doubled Nd:YAG lasers are robust, have a good beam quality and the light can easily be coupled into the standard beam path of a microscope. Alternative light sources are diode-pumped lasers like Nd:YLF lasers that have a longer pulse length. This increases the signal intensity of fluorescent tracers. Ongoing development of laser diodes and high-power LEDs will increase the applicability of these types of light sources when used to illuminate μ PIV recordings.

For a high image quality the camera should have the highest possible sensitivity/quantum efficiency. If the signal quality is insufficient intensified CCD cameras are an alternative but the image quality of intensifiers is poor. The use of double-shutter cameras reduces the time interval between two consecutive recordings to $1 \mu\text{s}$ allowing measurements of high velocities at high magnification. The quality of a μ PIV recording is significantly improved by fluorescence imaging.

Fluorescent tracer particles are added to the flow. Fluorescence is excited by illumination with monochrome laser light and the tracer emits light shifted to a longer wavelength, while all other obstacles like the walls of the microchannel reflect and scatter light at the original wavelength. An optical filter in the microscope is placed between the light collecting objective and the digital camera. The optical filter reflects light at the illumination wavelength and transmits the fluorescent light that has a longer wavelength. With this optical setup, light originating from the fluorescent tracer particles is collected on the camera sensor, while light originating from the channel walls and other non-fluorescent disturbances is blocked by the optical filter. This significantly improves the signal to noise ratio of the μ PIV measurement. A schematic of a μ PIV set-up is shown in Figure 17 (for detail refer to Lindken et al., 2009).

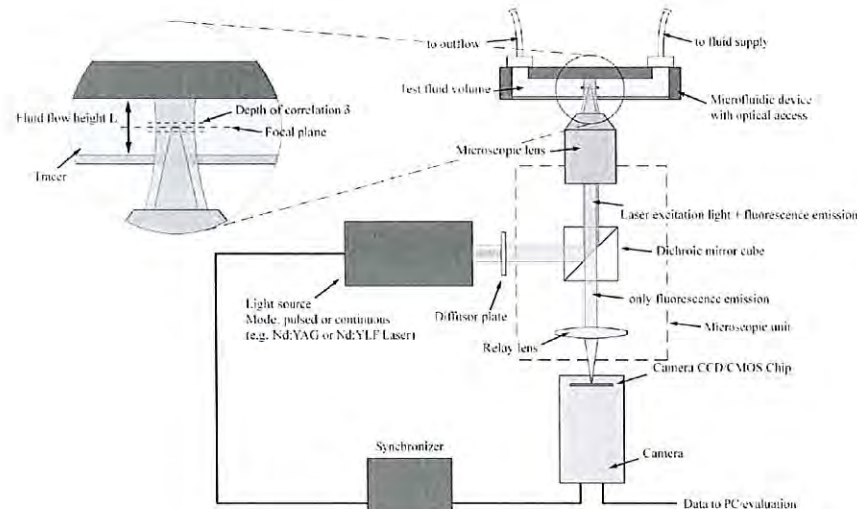


Figure 17: Schematic of a μ PIV setup (Lindken et al., 2009).

Currently, applying the advanced techniques, the maximum spatial resolution of this technique stands at approximately $1\mu\text{m}$. By using smaller seed particles that fluoresce at shorter wavelengths, this limit could be reduced by a factor of 2 to 4 (Raffel et al., 2007). Still higher spatial resolutions could be obtained by adding a particle tracking step after the correlation-based PIV. Spatial resolutions of an order of magnitude smaller could then reasonably be reached.

The various μ PIV apparatus and algorithms have been demonstrated to allow measurements at length scales on the order of $1\mu\text{m}$, significantly below the typical Kolmogorov length scale. These spatial resolutions are indispensable when analyzing flows in microdomains or the smallest scales of turbulence. The most significant problem standing in the way of extending μ PIV to gas phase flows is seeding. With adequate seeding, it can be extended to gas flows. The significant issues associated with gas phase flows and microchannel flow are further explored by Meinhart et al. (2000, 1999).

Errors in PIV

PIV measurements contain errors arising from several sources which are mentioned below (Prasad, 2000):

- (1) *Random* error due to noise in the recorded images.
- (2) *Bias* error arising from the process of computing the signal peak location to sub-pixel accuracy.

(3) *Gradient* error resulting from rotation and deformation of the flow within an interrogation spot leading to loss of correlation.

(4) *Tracking* error resulting from the inability of a particle to follow the flow without slip.

(5) *Acceleration* error caused by approximating the local Eulerian velocity from the Lagrangian motion of tracer particles.

Certain errors can be minimized by careful selection of experimental conditions (for example, tracking error). However, other sources are inherent to the nature of the correlation in PIV and cannot be eliminated. For example, even if the recorded images are free from noise, the location of the correlation peak can be influenced by random correlations between particle images not belonging to the same pair. In addition, bias errors result from a phenomenon called pixel-locking in which the signal peak location is biased towards the nearest pixel while using a curve-fit or centroiding schemes to locate the discretized signal with sub-pixel accuracy. Similarly, gradient errors will occur in turbulent flow. Finally, acceleration error cannot be eliminated because of the very principle of PIV which uses the Lagrangian motion of particles to approximate the instantaneous Eulerian flow velocity.

Previous work has shown that random errors in PIV usually scale with the particle image diameter (Adrian, 1991).

$$\sigma_{\text{random}} = cd_e$$

where d_e is the effective particle image diameter, and c is a constant whose value is between 0.05 and 0.10 depending upon experimental conditions (Prasad, et al., 1992; Boillot and Prasad, 1996).

Bias errors arise during the process of calculating the particle displacement to sub-pixel accuracy. Essentially, the correlation field is available on a discretized grid (typically 32×32). The location (S_x, S_y) of the maximum value in the correlation field will correspond to the particle displacement, but obviously, such a displacement will be an integer pixel value. In order to reduce measurement error, one attempts to locate the peak with sub-pixel accuracy using either a curve-fit method or a centroiding scheme. Unfortunately, any such scheme causes both random errors and bias errors. Experience shows that while centroiding schemes perform poorly on both counts in comparison to a parabolic or Gaussian curve-fitting, the latter can also cause significant bias errors.

The term bias error was coined to describe the phenomenon of pixel-locking, i.e. during the process of determining the displacement to sub-pixel accuracy, the resulting value is always biased towards the nearest integer-valued pixel (Prasad, et al., 1992). Bias error is zero if the particle is displaced exactly n pixels or $n + 0.5$ pixels, where n is an integer. For displacements $n < \Delta x < n + 0.5$ pixels, the measured displacement is biased towards n , and for $n + 0.5 < \Delta x < n + 1$ pixels, the measured displacement is biased towards $n + 1$. The situation is depicted in Figure 18 where a linear velocity profile (Couette flow) actually gets measured as a 'staircase' profile. The true and measured values coincide at integer and at half-pixel values.

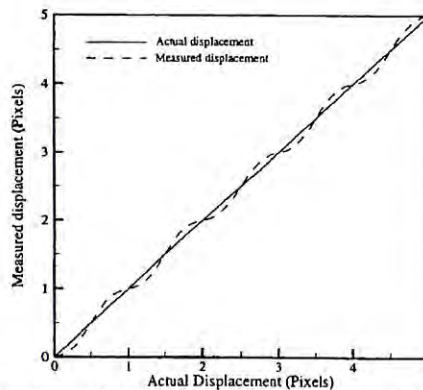


Figure 18: Bias error due to pixel-locking.

FlowMaster Endoscopic PIV

Camera and Laser
Endoscopes for Limited Optical
Access

PIV measurements in IC engines, turbo machinery or pumps usually require the manufacturing of costly prototypes with large windows to gain optical access. Using LaVision's endoscopic PIV system has enormous advantages in these experiments. Small optical access of only 8 mm holes enables PIV measurements in a much easier way and therefore reduces the costs and complexity of the required prototype.



laser endoscope



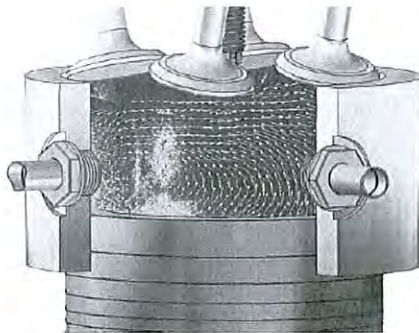
camera endoscope

LaVision's **laser endoscope** generates a laser light sheet from a high power pulsed laser. It is designed to fit at the outlet of the **Laser Guiding Arm** (articulated arm) and consists of a thin steel tube at the end. Image acquisition is done by a specially developed **camera endoscope** which can easily be mounted to a **FlowMaster** series camera together with a lens.

Applications

- ▶ Internal aerodynamic phenomena
- ▶ turbomachinery, aircraft engines, compressors, pumps
- ▶ IC engine flows, tumble and swirl studies
- ▶ reactive flow fields, Industrial reactors, combustion studies
- ▶ pharmaceutical and medical applications

Synchronized IC-Engine Flow Investigations



Instantaneous in-cylinder tumble flow applying endoscopic imaging

The **FlowMaster Micro-PIV** systems are designed to measure velocity fields of particle seeded flows with micron scale spatial resolution using PIV techniques.



stereoscopic Micro-PIV setup

The light source is a double pulsed Nd:YAG laser that is focused by an epifluorescent microscope with a high numerical aperture on a microfluidic device. The microflow is seeded with fluorescent particles. A microscope lens collects the particle signal that has a longer wavelength than the illuminating light. This signal is separated from the laser light by a filter cube and is recorded by a **FlowMaster** series camera. The double frame images are evaluated with conventional PIV algorithms.

Experimental study of vorticity-strain rate interaction in turbulent partially premixed jet flames using tomographic particle image velocimetry

Bruno Coriton and Jonathan H. Frank^{a)}

Combustion Research Facility, Sandia National Laboratories, Livermore, California 94551, USA

The investigated flow conditions were the same as those described in Coriton and Frank⁴¹ consisted of Sandia flame C,⁴² a turbulent piloted partially premixed CH₄/air jet flame,

The experimental configuration for tomographic PIV measurements is depicted in Fig. 1. A detailed description and measurement uncertainty analysis are provided in Coriton and Frank,⁴¹ and only a brief overview is given here. The apparatus consisted of a high repetition rate diode-pumped dual-head Nd:YAG laser and a set of four high speed CMOS cameras. Measurements were performed at a repetition rate of 10 kHz using a laser energy of 5 mJ/pulse. A pair of cameras was positioned on each side of the laser beam with two camera lenses positioned at 20° with respect to the z -axis and the other two camera lenses at 30°. The cameras were operated at 20 kHz in a frame straddling mode using an 896×800 px² region of the detector with a projected pixel size of approximately 15 $\mu\text{m}/\text{px}$. The jet and coflow were seeded with 0.3 μm aluminum oxide particles. Light scattering from the alumina particles was imaged onto each camera using identical camera lenses and Scheimpflug mounts to compensate for the displacement of the imaging plane. The camera lenses were stopped down to $f/16$ and $f/22$ to obtain the necessary depth of field across the probe volume. Computation of the velocity vectors consisted of smoothing (3×3 px² Gaussian filter) and correcting the raw particle images for non-uniformity of particle scattering signals, reconstructing the particle volume distribution using a multiplicative algebraic reconstruction tomography (MART) algorithm, calculating the velocity vectors by iterative volume cross correlation for a final volume interrogation size of $24 \times 24 \times 24$ vx³ ($393 \times 393 \times 393$ μm^3) with 75% overlap. Spurious vectors were identified and replaced using an outlier detection method, and the measurement noise was further reduced with a spatial filter based on a penalized least-square method. The probe volume size was $16.5 \times 12.3 \times 2.5$ mm $\sim 2.21D \times 1.65D \times 0.33D$ and contained $169 \times 126 \times 26$ vectors with approximately 98 μm spacing. The probe volume straddled the mean reaction zone location of the turbulent flames, which spans radial positions of approximately $x/D \sim 0.8$ – 1.6 and is identified by the mean OH laser-induced fluorescence (LIF) signal shown in Fig. 1. Vorticity and

The spatial dynamic range of PIV measurements is essentially limited by the camera detector size and can be too restrictive for resolving the full range of turbulence length scales, resulting in a compromise between resolving large or small scale structures. In the present study, the imaging magnification of approximately 1.9 yielded a reconstructed probe volume that encompassed approximately half the width of the turbulent jets at $y/D = 15$. The smallest turbulence length scale that could be resolved by the TPIV system according to the Nyquist criterion was 786 μm , which corresponds to twice the dimension of the interrogation region. The smallest turbulence length scales (Table I) were not resolved by the TPIV system. According to Worth *et al.*⁴⁴ and Buxton *et al.*,⁴⁵ a minimum interrogation volume size of 3 – 6η is required to accurately determine the turbulent

thin volume in one direction a "slab"

"slab"

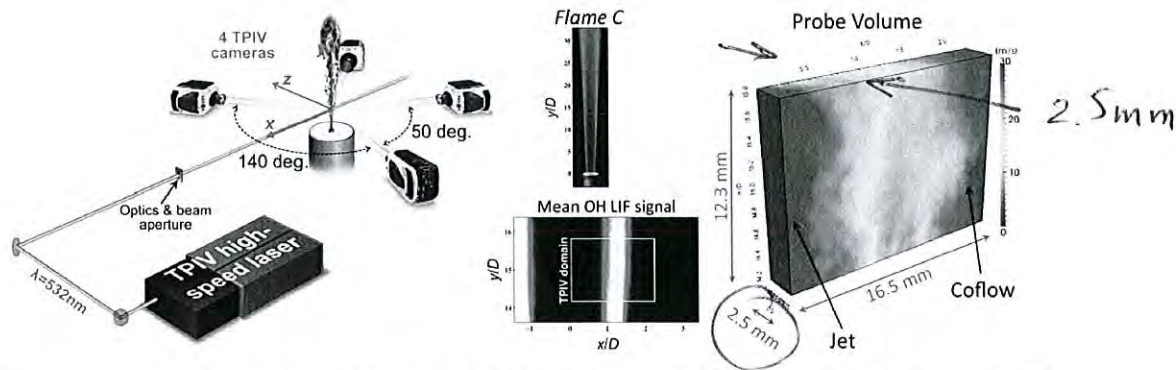


FIG. 1. Left: experimental configuration for tomographic PIV measurements in turbulent piloted jet flames and air jet. Center: location of the measurement probe volume relative to the mean location of the reaction zone, as indicated by the flame luminosity and mean OH LIF signal. Right: velocity magnitudes from a single-shot tomographic PIV measurement in flame C. The jet axis is located near the left edge of the probe volume.

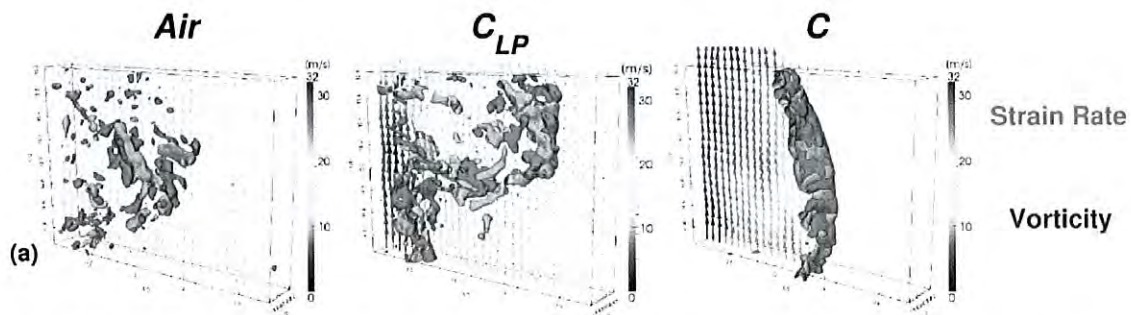


FIG. 3. (a) Strain rate isosurfaces (red) and vorticity isosurfaces (blue) for $|s| = 2.6\langle|s|\rangle$ and $\omega = 3.0\langle\omega\rangle$ from single-shot measurements in the *Air* jet (left), flame C_{LP} (middle), and flame C (right). (b) Enstrophy production isosurfaces and (c) strain-rate production isosurfaces for $III_{\omega} = III_s = 300 \times 10^9 \text{ s}^{-3}$ (red) and $III_{\omega} = III_s = -300 \times 10^9 \text{ s}^{-3}$ (blue) in the *Air* jet, for $III_{\omega} = III_s = 350 \times 10^9 \text{ s}^{-3}$ (red) and $III_{\omega} = III_s = -350 \times 10^9 \text{ s}^{-3}$ (blue) in flame C_{LP} , and for $III_{\omega} = III_s = 400 \times 10^9 \text{ s}^{-3}$ (red) and $III_{\omega} = III_s = -400 \times 10^9 \text{ s}^{-3}$ (blue) in the flame C . Velocity vectors are plotted in the central plane at $z/D = 0$ (1 out of 36 in-plane vectors plotted). The jet axis is located near the left edge of the probe volume. Additional sample shots of each case are available in the supplementary material.⁴⁶

Assessment and application of tomographic PIV for the spray-induced flow in an IC engine

B. Peterson^{a,*}, E. Baum^b, C.-P. Ding^b, D. Michaelis^c, A. Dreizler^d,
B. Böhm^d

^a Institute for Energy Systems, Department of Mechanical Engineering, School of Engineering, University of Edinburgh, The King's Buildings, Mayfield Road, Edinburgh EH9 3JL, Scotland, UK

^b Fachgebiet Reaktive Strömungen und Messtechnik (RSM), Technische Universität Darmstadt, Jovanka-Bonshits-Straße 2, 64287 Darmstadt, Germany

^c LaVision GmbH, Anna-Vandenhoeck-Ring 19, 37081 Göttingen, Germany

^d Fachgebiet Energie- und Kraftwerkstechnik (EKT), Technische Universität Darmstadt, Jovanka-Bonshits-Straße 2.

This paper presents the first application of TPIV to resolve the 3D3C spray-induced flow within a SG-DISI optical engine. TPIV measurements are obtained after injection when particle distributions are suitable for accurate TPIV particle reconstruction. Planar high-speed PIV (HS-PIV) measurements (4.8 kHz) are combined with TPIV (3.3 Hz) to provide a time-history of the fuel-spray and 2D2C flow-field preceding the phase-locked, single-cycle TPIV measurements. HS-PIV also pro-

Figure 1 shows the experimental setup for the combined TPIV and planar HS-PIV. A dual-cavity frequency-doubled Nd:YAG (Spectra Physics, 350 mJ/pulse, 3.3 Hz) was used for TPIV. The laser beam passed through a half-wave plate (p-polarized) and two cylindrical lenses to expand and collimate laser light to specify the laser sheet thickness (5 mm). The light passed through a

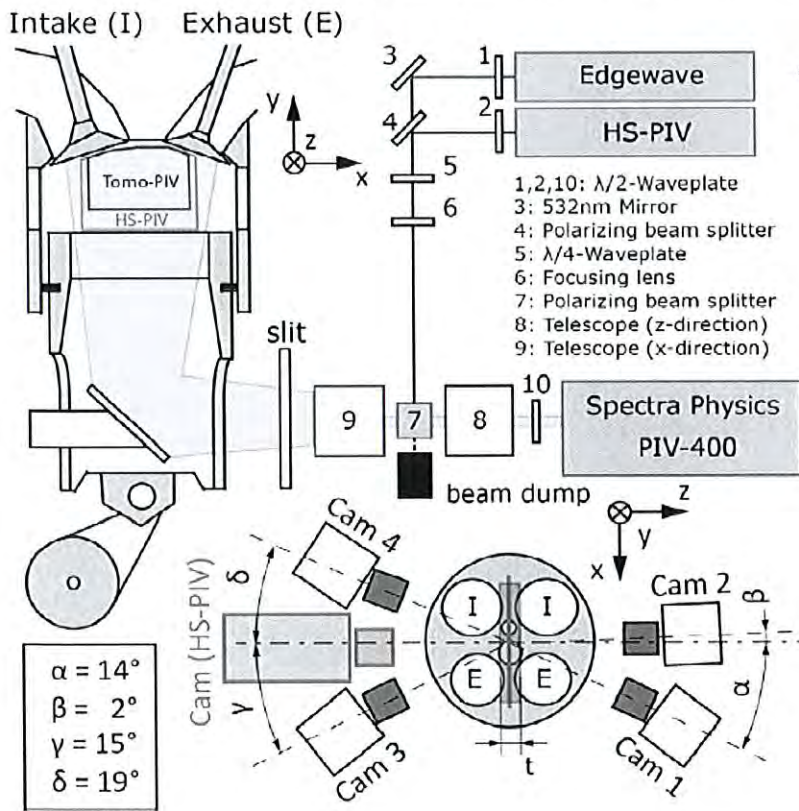


Fig. 1. Experimental setup.

Tomo PIV

pulsed

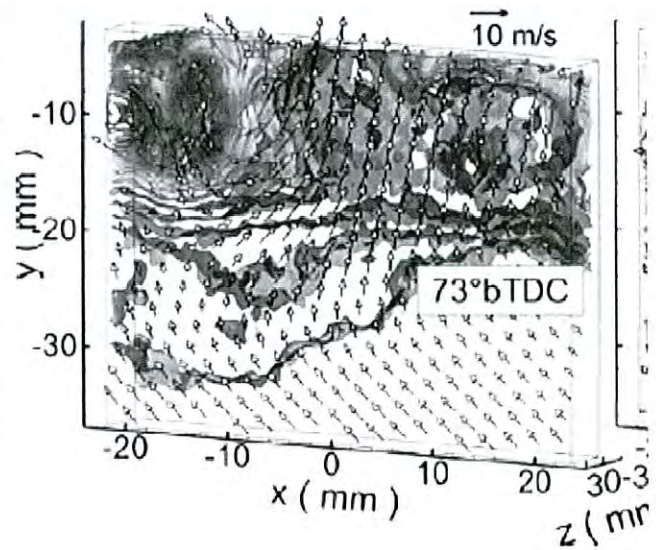
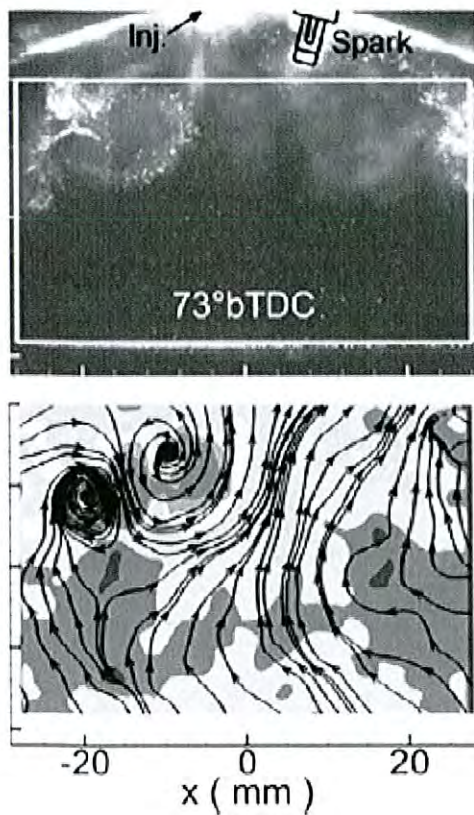
4.8 kHz
regular PIV

3.3 Hz
Tomo PIV

pulsed

vided an independent line-of-sight information of the illuminated volume ($50 \times H \times 5 \text{ mm}^3$; height (H) determined by piston position) centered within the cylinder axis.

TPIV and HS-PIV were processed with DaVis 8.2.1 (LaVision). Images of a spatially defined transparency < 0.2 pixels. 3D particle reconstruction was performed using an iterative Multiplication Algebraic Reconstruction Technique algorithm (Fast-MART). TPIV was calculated by direct volume correlation with decreasing volume size (final size: $64 \times 64 \times 64$ pixels) with 75% overlap, providing a $1.5 \times 1.5 \times 1.5 \text{ mm}^3$ spatial resolution (based on the final interrogation window size) and 0.375 mm vector spacing in each direction. HS-PIV images

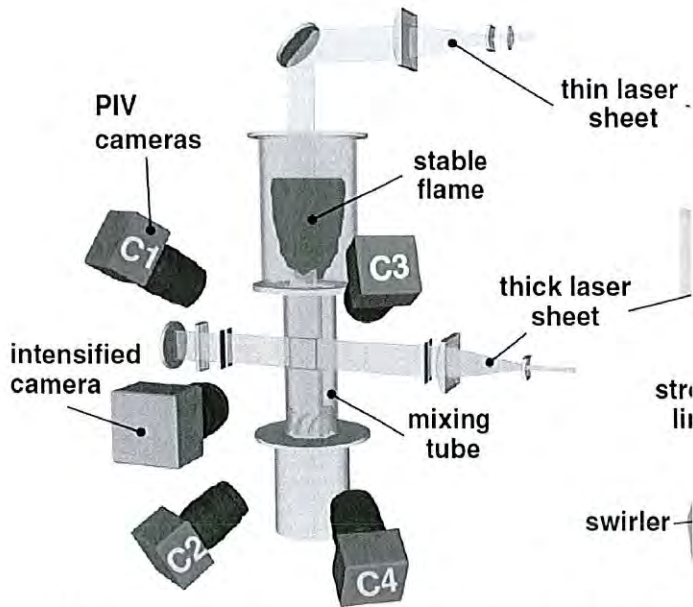


Simultaneous high-speed 3D flame front detection and tomographic PIV

Tomo PIV

Dominik Ebi and Noel T Clemens

Department of Aerospace Engineering and Engineering Mechanics, The University of Texas at Austin, Austin, TX 78712 USA



Olive oil droplets with a diameter of about $1 \mu\text{m}$ were used as an aerosol in this work, which were seeded into the flow with a six-jet atomizer (TSI-Inc.). The olive oil droplets were illuminated with a high-repetition rate diode-pumped, frequency doubled (527 nm) Nd:YLF laser (Coherent Evolution-90) operated at a repetition rate of 5 kHz providing about 13 mJ pulse^{-1} . The laser beam was expanded into a collimated sheet with a height of about 30 mm by a set of cylindrical lenses. The large natural beam divergence of the employed laser system ($M^2 = 25$) was sufficient to provide a thick sheet with a thickness of about 17 mm (FWHM) at the probe volume loca-

drops at 5 kHz

The Mie scattering was recorded with four high-speed CMOS cameras (Photron FASTCAM-ultima APX) operated at 10kHz, which limits the resolution to $256 \times 512 \text{ pix}^2$. The cameras were fitted with Scheimpflug adapters and Nikkor 105mm lenses set to an aperture of $f/8$. The small aperture provided the depth-of-field needed for the particles to be in focus in the entire illuminated volume. The cameras were oriented in a diagonal cross-like arrangement with a total camera angle of about 60° , which is optimal for the tomographic reconstruction [42]. The field-of-view for each camera is about $30 \times 15 \text{ mm}^2$ with pixel resolutions within 3% of $64 \mu\text{m}$

Mie camera at 10kHz

The four cameras were operated at twice the frequency compared to the lasers to quasi-simultaneously record both, the Mie scattering resulting from the droplet illumination by the thick sheet as well as from the illumination by the thin sheet. The timing is illustrated in figure 2. A master clock

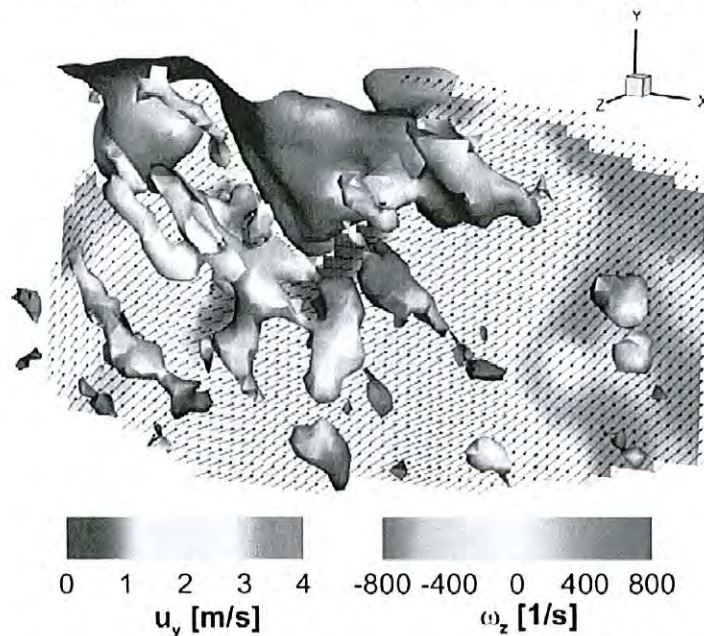


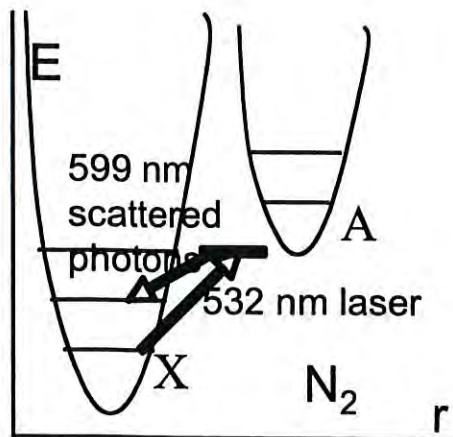
Figure 14. Reconstructed 3D flame front (rendered in blue) and velocity field in unburnt gas. Contour shows axial velocity field in one z -plane. 3D vortical structures are visualized by an iso-surface of λ_2 and colored by the z -component of vorticity.

Raman Scattering

To measure number density of
MAJOR SPECIES – such as:
 N_2 , O_2 , H_2O , CO_2 , CH_4 , CO , C_2H_6 , H_2

Single point (no 2-D image),
 Time averages, usually not instantaneous
 Expensive, need big laser (1 joule/pulse)

Raman scattering: laser light at any wavelength (such as green) scatters off ground-stated molecules, causing molecule to briefly jump up to an energetic state that is not an allowed quantum level, then returns to an excited allowed state. Scattered light is red shifted – shift is different for each type of molecule.



Raman signal much weaker than fluorescence since laser not tuned to an allowed absorption transition, only consider major species and need powerful laser of 1 Joule/pulse

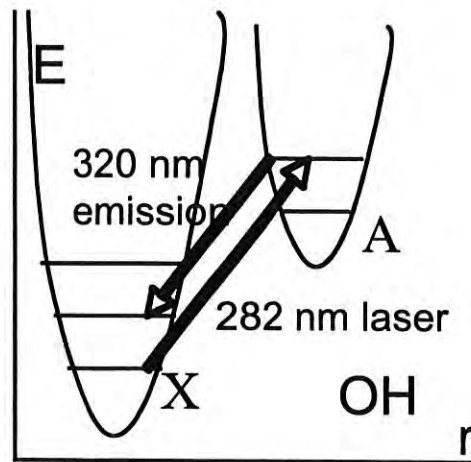
Tunable laser not needed
 Measure ALL species with each laser pulse
 No correction for collisional quenching

Laser Induced Fluorescence

To measure number density of **MINOR SPECIES** such as:
 OH , CH , CH_2O , NO , CO , O , H

Single point or 2-D planar imaging
 Signal large enough for instantaneous images
 Not too expensive, but need a tuneable dye laser

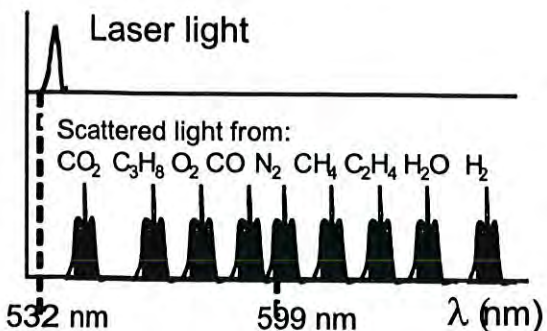
Fluorescence: absorption followed by spontaneous emission of a photon. Laser must be tuned to rotational line in absorption spectrum of one molecule, molecule jumps from ground state up to an allowed quantum level (absorption) then after 10^{-8} sec it spontaneously jumps down to a level higher than ground state. Emitted light is red shifted; amount of shift different for each type of molecule.



Fluorescence signal is much stronger than Raman
 But only minor species fluoresce
 Need only few milliwatts per laser pulse

Tunable laser required
 Measure only ONE species with any one laser setup; need to retune and repeat for others

Raman scattering (continued)



from energy level diagram

E1 = ground state

E* = temporary excited state

E2 = final state

$$\nu_{\text{laser}} = (E^* - E1)/h$$

$$\nu_{\text{scattered}} = (E^* - E2)/h$$

$$\Delta\nu = \nu_{\text{laser}} - \nu_{\text{scattered}}$$

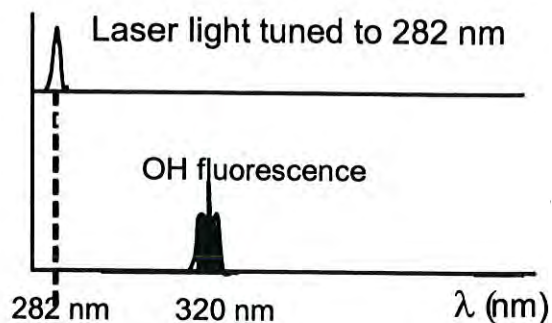
$$\Delta\lambda / \lambda = \Delta\nu / \nu \quad \text{so:}$$

$$\Delta\lambda_{N2} / \lambda_{\text{laser}} = (E2 - E1) / h \nu_{\text{laser}}$$

From Lederman 's paper in PECS, if a 532 nm YAG laser is used:

	$\Delta\nu$ (cm ⁻¹)	$\Delta\lambda$ (nm)
CO2	1286	36
C3H8	1451	41
O2	1556	44
CO	2143	61
N2	2330	67
CH4	2914	82
C2H4	3020	85
H2O	3651	103
H2	4060	115

Fluorescence (continued)



from energy level diagram

E1 = ground state

E* = upper quantum level - excited state

E2 = final state

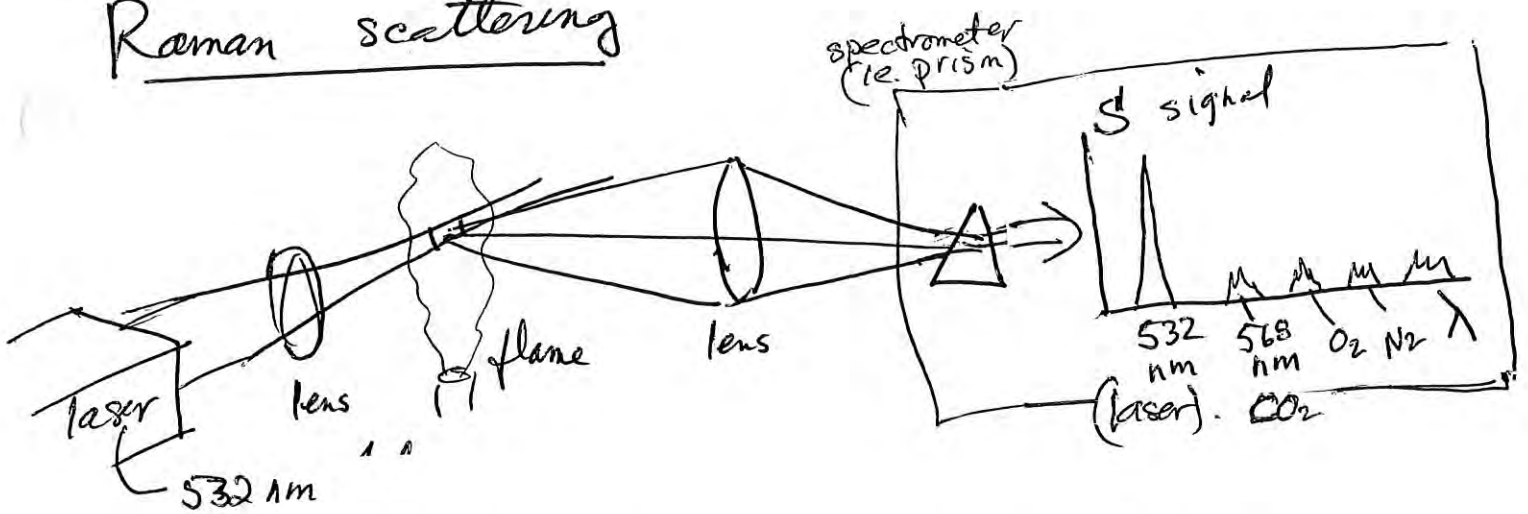
$$\nu_{\text{laser}} = (E^* - E1)/h$$

$$\nu_{\text{fluorescence}} = (E^* - E2)/h \quad \text{so:}$$

$$\lambda_{\text{laser}} = c h / (E^* - E1)$$

$$\lambda_{\text{fluorescence}} = c h / (E^* - E2)$$

Raman scattering



consider the band of Raman scattered light from the CO_2 molecule. It is shifted 36 nm to the red (larger wavelength) from the laser line

ex. laser line $\lambda = 532 \text{ nm}$ (green) CO_2 band $\Rightarrow \lambda = 568 \text{ nm}$ (yellow)

Raman signal - formula is similar to Rayleigh scattering

$$S_{\text{CO}_2} = (\text{const}) \cdot I_{\text{laser}} \cdot n_{\text{CO}_2} \cdot \sigma_{\text{CO}_2} \cdot f(T)$$

signal from $\text{CO}_2 =$ light in band near 568 nm laser intensity # CO_2 molecules / volume scattering cross section for CO_2 temp. affects band width

calibrate by recording signal S_{N_2} from N_2 of known n_{N_2}

$$\hookrightarrow n_{\text{CO}_2} = \chi_{\text{CO}_2} \frac{P}{kT}$$

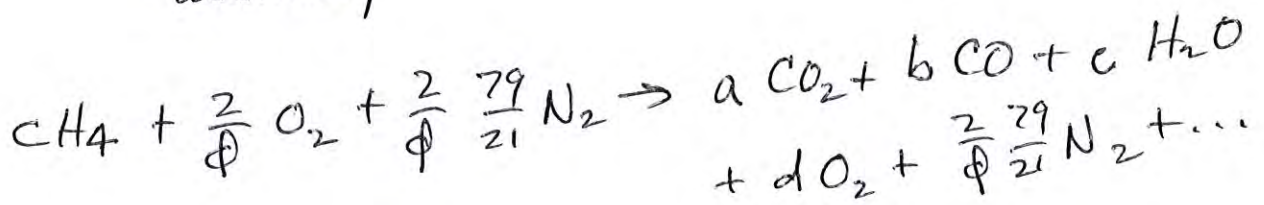
$$\boxed{\frac{S_{\text{CO}_2}}{S_{\text{N}_2}} = \frac{n_{\text{CO}_2}}{n_{\text{N}_2}} \frac{\sigma_{\text{CO}_2}}{\sigma_{\text{N}_2}}}$$

Mixture fraction = Z = most important quantity in nonpremixed flames

select carbon atoms

$$Z_c = \frac{\text{mass fraction carbon atoms in any molecule}}{\text{mass fraction carbon atoms in fuel stream}}$$

assuming air stream has zero carbon



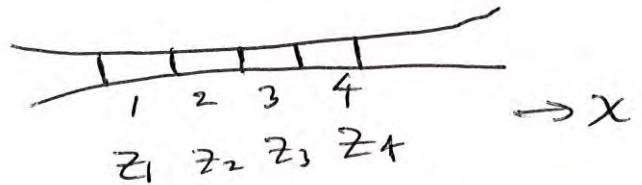
$$Z_c = \frac{\left[\frac{12a + 12b}{44a + 28b + 18c + \dots} \right]}{[12/16]}$$

measure a, b, c, d
to measure Z_c

Scalar dissipation rate χ

$$\chi = 2D \left[\left(\frac{\partial Z}{\partial x} \right)^2 + \left(\frac{\partial Z}{\partial y} \right)^2 + \left(\frac{\partial Z}{\partial z} \right)^2 \right]$$

along the laser beam
focus camera pixels
on regions 1, 2, 3 and 4



use central difference formula to get $\frac{\partial Z}{\partial x}$ from z_1, z_2, z_3, z_4
then point laser in y direction, z direction and repeat

Raman scattering

advantages

- get all major species (about 6) in each pulse
- good spatial resolution (1mm x 0.5mm x 0.5mm)
local, not line of sight
- laser pulse is 10nsec - good temporal resolution

disadvantages

- cannot do small concentrations, mole fractions $< 1\%$
- cannot do 2-D imaging, line Raman only
- probe volume must be 1mm long, cannot resolve

Kolmogorov scales

- must have a clean "blue" flame -
fuel can be: H_2 , CH_4 , DME, CO
fuel cannot be propane, ethylene, Jet A
- need large windows to collect very dim light
- cannot do sooty flames, particles, PIV, droplets
- some Raman scattering bands overlap
- powerful laser cracks glass windows

Relationships among Nitric Oxide, Temperature, and Mixture Fraction in Hydrogen Jet Flames

R. S. BARLOW*

Combustion Research Facility, Sandia National Laboratories, Livermore, CA 94551-0969

and

C. D. CARTER

Systems Research Laboratories, Inc., Dayton, OH 45440-3696

Simultaneous point measurements of NO, the major species, mixture fraction, temperature, and OH are obtained in nonpremixed turbulent hydrogen jet flames, using the combination of spontaneous Raman scattering, Rayleigh scattering, and laser-induced fluorescence. Results are presented for an undiluted hydrogen flame at Reynolds number 10,000 and for flames with 20% and 40% helium dilution, with emphasis on the relationships among nitric oxide, mixture fraction, and temperature. Conditional statistics are used to extract information on the coupling between reaction zone structure and measured NO levels. Fluctuations of the NO mole fraction conditional on mixture fraction are greatest near the base of the flame, where NO formation rates and concentrations are sensitive to local strain. Similarly, when NO levels are averaged conditional on both mixture fraction and temperature, the temperature dependence is strongest near the flame base, where reaction zones are thin. The radial dependence of the conditional mean NO mole fraction (conditional on mixture fraction) is shown to be small at upstream locations and negligible at the downstream locations that contribute most to the overall NO emission. These results combined with previously reported data on the present hydrogen flames provide a detailed basis for evaluation and refinement of turbulent combustion models for thermal NO_x formation in jet flames.

INTRODUCTION

A critical objective of current research and development in combustion is to predict and minimize NO_x formation in practical combustion devices [1]. A detailed knowledge of NO_x formation mechanisms in simple turbulent jet diffusion flames is an important step toward this larger objective. Several experimental studies have been carried out to determine the effects of parameters such as fuel type, residence time, radiation, buoyancy, and dilution on NO_x formation in jet flames [2-9]. These experiments were based upon gas-sampling probe techniques that yield only averaged measurements. Consequently, the details of turbulence-chemistry interactions and the instantaneous relationships between NO concentration

and other scalars were not measured, and the basis for comparison with turbulent combustion models has therefore been limited.

In the present study, pulsed-laser diagnostics are used to obtain simultaneous point measurements of NO, the major species, OH, and temperature in turbulent hydrogen jet flames. Our initial work with this combined diagnostic capability has concentrated on hydrogen because its relatively simple kinetics facilitate the assessment of combustion models, particularly the approaches used in modeling turbulence-chemistry interactions. We have made extensive measurements consisting of radial profiles at several streamwise locations in an undiluted hydrogen jet flame with a jet Reynolds number of 10,000 and in two helium-diluted hydrogen flames. Dilution with helium reduces the radiative fraction to low levels, allowing for independent evaluation of turbulence-chemistry submodels and radiation submodels.

* Corresponding author: Robert S. Barlow, Department 8351, MS 9051, Sandia National Laboratories, Livermore, CA 94551-0969. barlow@ca.sandia.gov

A significant body of results from this study were reported in Ref. 10, including scatter plots of measured scalars at various streamwise locations, mean values of the NO mole fraction conditional on mixture fraction, and overall NO emission values for the undiluted and diluted flames. In the present paper we focus on the relationships among NO, mixture fraction, and temperature by considering averages and rms fluctuations of the NO mole fraction conditional on: i) the mixture fraction alone and ii) both mixture fraction and temperature.

Conditional data analysis is a useful tool for investigating the influence of turbulent mixing on thermochemical states in flames. Processing the data conditional on the instantaneous mixture fraction yields quantitative information on turbulence-chemistry interactions that cannot be extracted from time- or Favre-averaging approaches. Double conditioning on mixture fraction and temperature (or some other reaction progress variable) allows a detailed look at the relationships among scalars under various conditions of local strain or departure from equilibrium. Some of the results in this paper are specifically relevant to the Conditional Moment Closure (CMC) model for turbulent combustion. However, the experimental results and conditional statistics presented here and in Ref. 10 provide a detailed basis for evaluating both the underlying assumptions and the predictive

accuracy of a variety of turbulent combustion models.

EXPERIMENTAL METHODS

Experiments were conducted in the Turbulent Diffusion Flame laboratory at the Combustion Research Facility. The flow facility and diagnostic systems have been described previously [10–12], and only a brief summary is included here. Spontaneous Raman scattering was used to measure concentrations of the major species, N_2 , O_2 , H_2 , and H_2O . The Rayleigh scattering signal was converted to temperature using a species-weighted scattering cross section, based on the Raman measurements. Rayleigh cross sections were derived from the survey of refractive indices by Gardiner et al. [13]. Linear laser-induced fluorescence (LIF) was used to measure NO and OH. Quantitative NO and OH concentrations were obtained by correcting these fluorescence signals on a shot-to-shot

basis for variations in the Boltzmann fraction and the collisional quenching rate, which were determined from the measured temperature and species concentrations. The NO data were also corrected for the temperature dependent effects of collisional line broadening. Mixture fraction was calculated from the measured species concentrations (moles/l) as

$$f = \frac{(w_{H_2} + \alpha w_{He})([H_2O] + [H_2]) + \left(w_H + \frac{\alpha}{2} w_{He}\right)[OH]}{w_{N_2}[N_2] + w_{O_2}[O_2] + (w_{H_2O} + \alpha w_{He})[H_2O] + (w_{H_2} + \alpha w_{He})[H_2] + \left(w_{OH} + \frac{\alpha}{2} w_{He}\right)[OH]}$$

where the w s are molecular weights and α is the mole ratio of helium to hydrogen in the fuel stream. Here, the helium-hydrogen ratio is assumed to be unaffected by differential diffusion. Note that other definitions of mixture fraction are possible [14].

The burner for the turbulent hydrogen flames was a straight tube (inner diameter, $d = 3.75$ mm and outer diameter 4.8 mm) centered at the exit of a vertical wind tunnel contraction. The beam from a flashlamp-pumped dye laser (532 nm, 5 Hz, ~ 750 mJ/pulse) was used for the Raman and

Rayleigh measurements. The NO and OH fluorescence measurements were accomplished using two separate Nd:YAG-pumped dye laser systems, which were fired approximately 1 and 2 μ s, respectively, before the Raman laser.

The output of one dye laser system was tuned to the $R_1(18)$ transition in the $A^2\Sigma^+ - X^2\Pi(0,0)$ band of NO. A solar-blind photomultiplier tube (PMT) and Schott UG-5 colored glass filters were used to collect NO fluorescence from the system of bands at 236, 247, 259, and 271 nm. The second dye laser system was tuned to the $O_{12}(8)$ transition in the $A^2\Sigma^+$

– $X^2\Pi(1,0)$ band of OH. Colored glass filters were used in front of a PMT for broadband detection of the (1,1) and (0,0) bands.

The temperature-dependent calibration functions for each of the Raman channels were determined by measuring signals from H_2 -air flat flames over a wide range of known conditions of temperature and species concentrations above a Hencken burner. (The Hencken burner is a nearly adiabatic burner consisting

of an array of small fuel tubes arranged in a stainless steel honeycomb matrix that allows for the flow of air.) OH measurement, were referenced to a H_2 -air Hencken burner flame at an equivalence ratio of $\phi = 0.94$, where the OH number density was measured by laser absorption. The NO calibration factor was determined by doping lean premixed laminar flames with known concentrations of NO and differencing the signals for two doping levels. As demonstrated in Ref. 10, the sensitivity of the NO system is sufficient to obtain measurements of NO concentrations below 10 ppm.

The spatial resolution for all measurements was $\sim 750 \mu\text{m}$ in each direction. The scalar gradient length scales, λ_B , in these flames were estimated as discussed in Ref. 15, based upon the relation $\lambda_B = 0.38C_B(x - x_0)\text{Re}_d^{-3/4}$, where $(x - x_0)$ is the streamwise distance from a virtual origin and Re_d is the jet Reynolds number. The viscosity of air at an intermediate temperature of 1200 K was used in the Reynolds number, and C_B was taken to be 10 [16]. For all the streamwise locations reported here the estimated λ_B was greater than the 750- μm measurement resolution by at least a factor of two. However, it is important to note that these estimates are based on correlations for nonreacting jets and that the measurement of scalar gradients in reacting flows is an active area of research.

RESULTS AND DISCUSSION

Table 1 summarizes the flow conditions and measurement locations for the experimental flames. In all cases the coflow air velocity was 1.0 m/s, and the flames were attached and unconfined. Ranges of temperature and humidity in the coflowing air were 293–295 K and 0.006–0.008 kg/kg-air. In Table 1, Re_d is the cold jet exit Reynolds number, and L is the

TABLE 1

Flame Parameters and Measurement Locations

H_2 :He (by vol.)	Re_d ($u_j d/\nu$)	L/d (visible)	Streamwise Locations (x/L)
100:0	10,000	~ 180	1/8, 1/4, 3/8, 1/2, 5/8, 3/4, 1
80:20	10,000	> 150	1/8, 1/4, 3/8, 1/2, 5/8, 3/4, 1
60:40	9,300	~ 100	1/2, 3/4, 1

approximate visible flame length. These flame conditions were chosen to match, as well as possible, some of the conditions for which Driscoll et al. [9] have reported sampling-probe measurements of the NO_x emission index. NO_2 levels within these flames are negligible [9], so the measurements of NO alone are sufficient to characterize the total NO_x concentrations.

Streamwise Evolution of Flame Structure

Radial profiles of Favre-averaged mixture fraction, temperature, and NO mole fraction, X_{NO} , for the three flames are shown in Figs. 1–3. These data quantify the spreading rate of the flame and the shape of the mean stoichiometric contour. Note that the mean mixture fraction on the centerline reaches the stoichiometric value at something less than 3/4 of the visible flame length in each case. Any model for NO_x formation in nonpremixed flames should, at the first level, predict these mean quantities accurately, as they reflect the entrainment and mixing process and determine the global residence time for NO_x formation.

The profiles for the undiluted case and the 20% helium case (Figs. 1 and 2) show that near the nozzle ($x = L/8$) the mixture fraction gradients are steep, even in the mean, and the zones of high temperature and high NO concentration are narrow. As discussed in our previous paper [10], point measurements and planar OH images [17] reveal a streamwise evolution of the structure of the high-temperature, NO production zone from thin layers near the flame base to broad regions near the flame tip. NO production rates near the flame base are expected to be sensitive to local scalar dissipation rates (local strain) in these thin reaction layers, due to the influence of strain on temperature depression and O-atom superequilibrium. NO concentrations are doubly

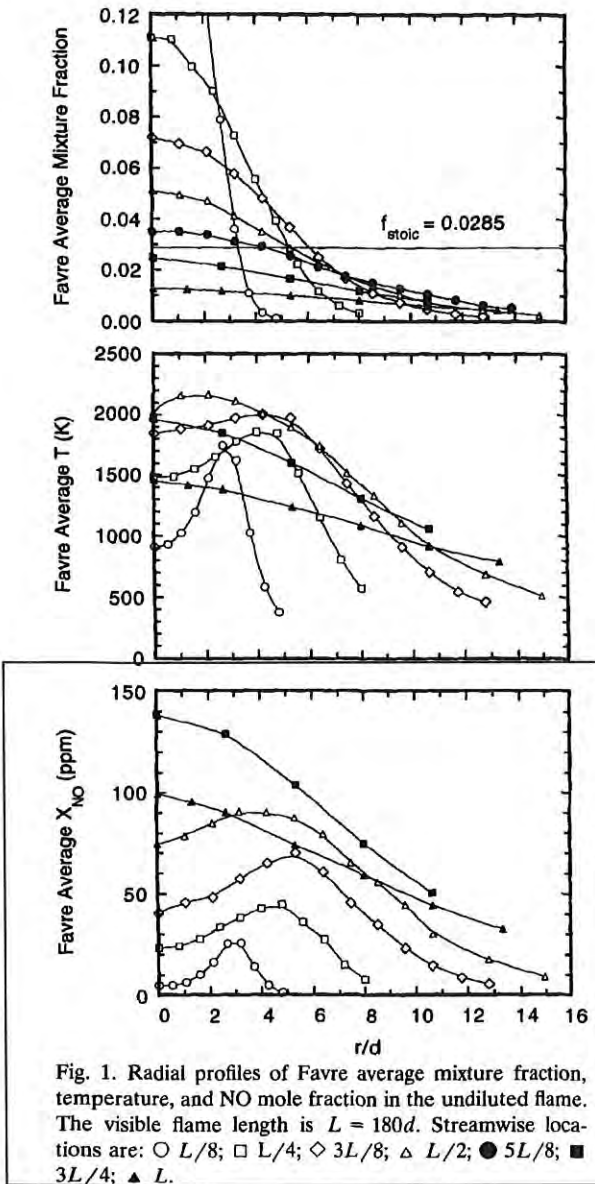


Fig. 1. Radial profiles of Favre average mixture fraction, temperature, and NO mole fraction in the undiluted flame. The visible flame length is $L = 180d$. Streamwise locations are: \circ $L/8$; \square $L/4$; \diamond $3L/8$; \triangle $L/2$; \bullet $5L/8$; \blacksquare $3L/4$; \blacktriangle L .

sensitive to local strain rates because of the combined effects of nonequilibrium chemistry and residence time. A high local strain rate means low temperature (relative to equilibrium) and short residence time at the NO forming conditions. Further downstream ($x = 3L/4, L$) scalar dissipation decreases, temperature and radical concentrations approach equilibrium, the high-temperature zones become broad, and instantaneous NO production rates at a given mixture fraction can be ex-

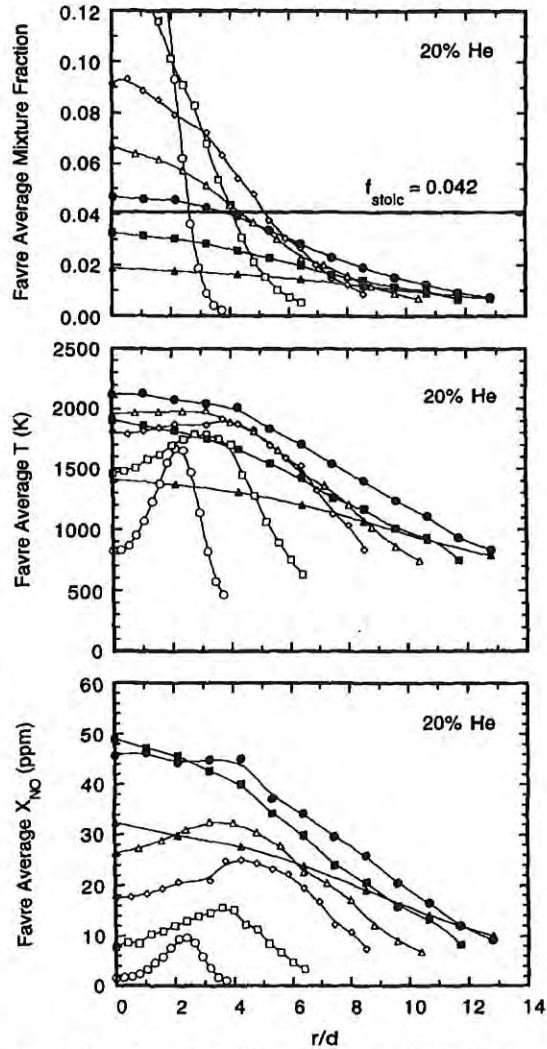


Fig. 2. Radial profiles of Favre average mixture fraction, temperature, and NO mole fraction in the 20% helium diluted flame. The visible flame length is $L = 150d$. Streamwise locations are: \circ $L/8$; \square $L/4$; \diamond $3L/8$; \triangle $L/2$; \bullet $5L/8$; \blacksquare $3L/4$; \blacktriangle L .

pected to approach the rate corresponding to equilibrium temperature and species concentrations. This streamwise evolution of reaction zone structure will be an important consideration as we examine conditional means and fluctuations of NO mole fraction.

Radial Dependence of the Conditional Means

A useful approach to quantifying the effects of turbulent mixing on thermochemical states in

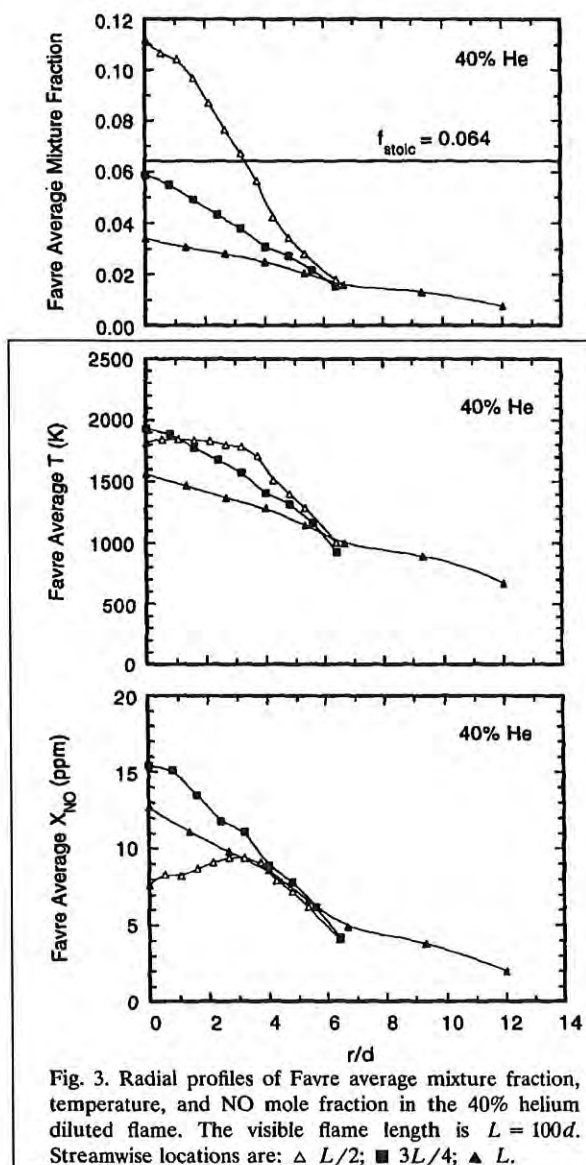


Fig. 3. Radial profiles of Favre average mixture fraction, temperature, and NO mole fraction in the 40% helium diluted flame. The visible flame length is $L = 100d$. Streamwise locations are: Δ $L/2$; \blacksquare $3L/4$; \blacktriangle L .

flames is to consider the measured scalar data in mixture fraction coordinates and determine statistics conditional on the instantaneous value of the mixture fraction. It would be convenient to include all measured data from a radial profile in determining conditional statistics. However, it must first be established that the conditional mean of a given scalar is not a strong function of radial location. Radial independence of conditional means is a convenient assumption of the Conditional Moment Closure model [18-20] as applied to jet flames,

and this assumption has been shown to be valid for major species concentrations in hydrocarbon jet flames that are far from extinction. In the present work we wish to check that the assumption of radial independence holds for the major species in hydrogen flames and determine to what extent the conditional means of temperature and nitric oxide vary with radius.

Figure 4 shows conditional means of temperature and the mole fractions of H_2 , O_2 , and H_2O at four axial stations in the undiluted flame. The five sets of curves in each graph correspond to different radial locations, as listed in Table 2. Intervals of 0.004 in mixture fraction were used in calculating the conditional means. Results confirm that there is no significant radial dependence of the conditional means of the major species. However, near the base of the flame, at $x = L/8$, there is a clear radial dependence of the conditional mean temperature. As the probe volume moves out in radius, the conditional mean temperatures shift downward by as much as 200 K. The magnitude of this radial dependence decreases with increasing streamwise distance, such that the spread in the curves at $x = 3L/4$ is less than 70 K.

The observed radial dependence of the conditional mean temperature suggests that the conditional scalar dissipation may also depend on radial location, particularly near the base of the flame. Reaction zones near the flame base are thin, and results in Ref. 10 show that these reaction layers have some characteristics similar to strained laminar flames. Laminar H_2 -air flame calculations (e.g., Ref. 10, Fig. 3) show that temperature reductions comparable to those observed in the conditional means are produced by strain rates within the range estimated for the present jet flame. These strain rates are at least an order of magnitude below the extinction limit for hydrogen-air. The possibility of a radial dependence of the joint statistics of mixture fraction and scalar dissipation has implications for several combustion modeling approaches, and the present results underscore the need for direct measurements of scalar dissipation in turbulent flames.

Due to the strong dependence of the NO production rate on temperature, one might

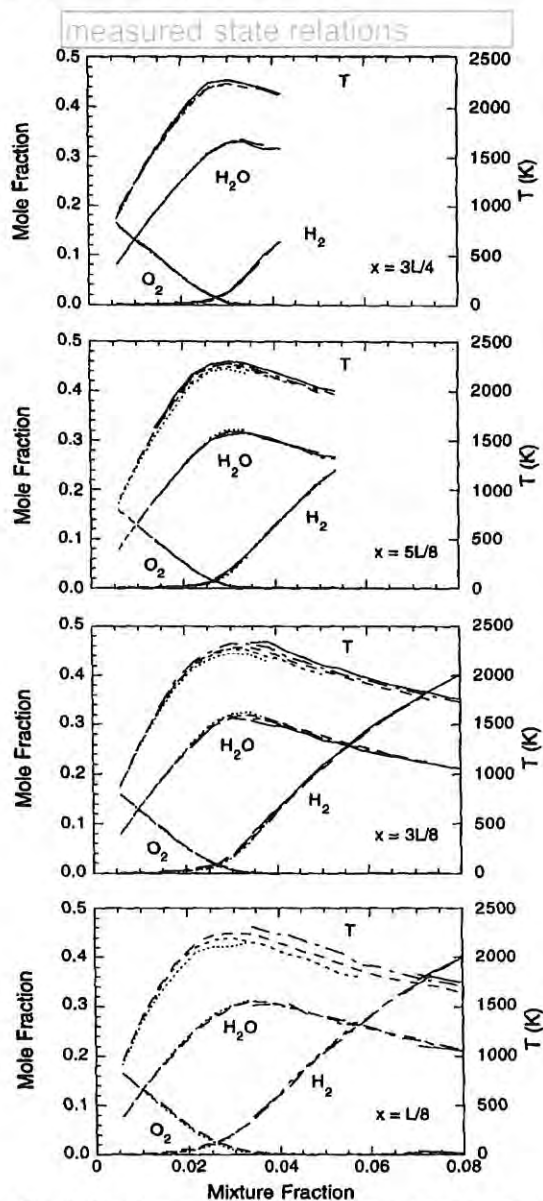


Fig. 4. Conditional mean temperatures and major species mole fractions calculated for each of five radial positions at four streamwise stations in the undiluted H₂ flame. In each plot the progression of line types (—), (---), (— · —), (----), (-----) runs from a radial location on the fuel-rich side of the mean stoichiometric contour to a radial location on the fuel-lean side. Locations are listed in Table 2.

expect the conditional mean NO mole fraction, $\{X_{NO}\}_f$, to exhibit a radial dependence. Figure 5 shows results for $\{X_{NO}\}_f$ at different radial locations for each of six downstream stations in the undiluted flame. The curves are not smooth because fluctuations in X_{NO} are

TABLE 2

Radial Locations for Conditional Means Plotted in Figures 4 and 5^a

x/L	(—) r/d	(---) r/d	(— · —) r/d	(----) r/d	(-----) r/d
3/4	0.0	2.7	5.3	8.0	10.7
	1.3	4.0	6.7	9.3	12.0
5/8	0.0	2.1	4.3	6.4	8.5
	1.1	3.2	5.3	7.5	9.6
1/2	3.2	5.3	6.4	7.5	10.7
					12.8
3/8	1.1	3.2	5.3	7.5	9.6
	2.1	4.3	6.4	8.5	10.7
1/4	0.8	2.4	4.0	5.6	7.2
	1.6	3.2	4.8	6.4	8.0
1/8	1.1	2.1	3.2	3.7	4.3
	1.6	2.7			

^a In most cases data from two adjacent measurement locations were combined to increase sample size.

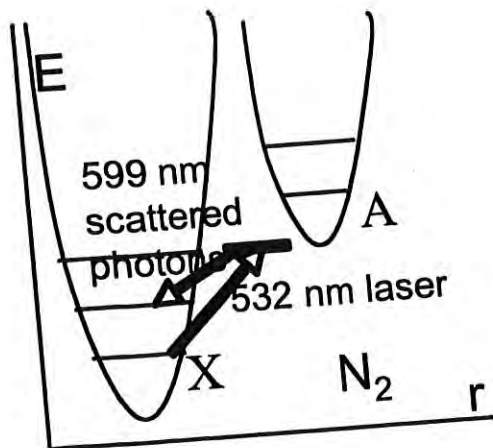
greater than those in temperature or major species mole fractions and we have only 6000 to 8000 samples at each streamwise position. (Operational constraints of the flashlamp-pumped dye laser made the collection of substantially more samples at each location impractical.) Nevertheless, there are clear trends in the data. In the lower portion of the flame, at $x = L/2$ and below, there is a distinct radial dependence of the conditional mean NO mole fraction. Five curves are shown in each plot, with the solid curve corresponding to the measurement location farthest inside the mean stoichiometric contour and the dotted curve corresponding to the location farthest outside. (See Table 2 for exact locations.) For fuel-rich values of the mixture fraction, the solid curve is highest, and the conditional mean NO levels decrease with increasing radius. This is consistent with the temperature curves, which also decrease with increasing radius. Surprisingly, the conditional means of temperature and NO move in opposite directions for fuel lean values of the mixture fraction, and $\{X_{NO}\}_f$ increases with radius in spite of the decrease in $\{T\}_f$. The physical mechanisms that lead to this counter-intuitive result are not obvious, but the implication is that, due to the relatively slow rate of thermal NO production, the convective history of fluid samples is more important than local conditions in determining measured NO levels.

Raman Scattering

To measure number density of
MAJOR SPECIES – such as:
 N_2 , O_2 , H_2O , CO_2 , CH_4 , CO , C_2H_6 , H_2

Single point (no 2-D image),
Time averages, usually not instantaneous
Expensive, need big laser (1 joule/pulse)

Raman scattering: laser light at any wavelength (such as green) scatters off ground-stated molecules, causing molecule to briefly jump up to an energetic state that is not an allowed quantum level, then returns to an excited allowed state. Scattered light is red shifted – shift is different for each type of molecule.



Raman signal much weaker than fluorescence since laser not tuned to an allowed absorption transition, only consider major species and need powerful laser of 1 Joule/pulse

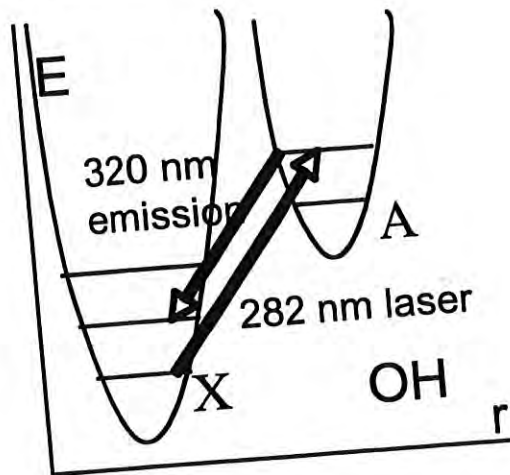
Tunable laser not needed
Measure ALL species with each laser pulse
No correction for collisional quenching

Laser Induced Fluorescence

To measure number density of **MINOR SPECIES** such as:
 OH , CH , CH_2O , NO , CO , O , H

Single point or 2-D planar imaging
Signal large enough for instantaneous images
Not too expensive, but need a tuneable dye laser

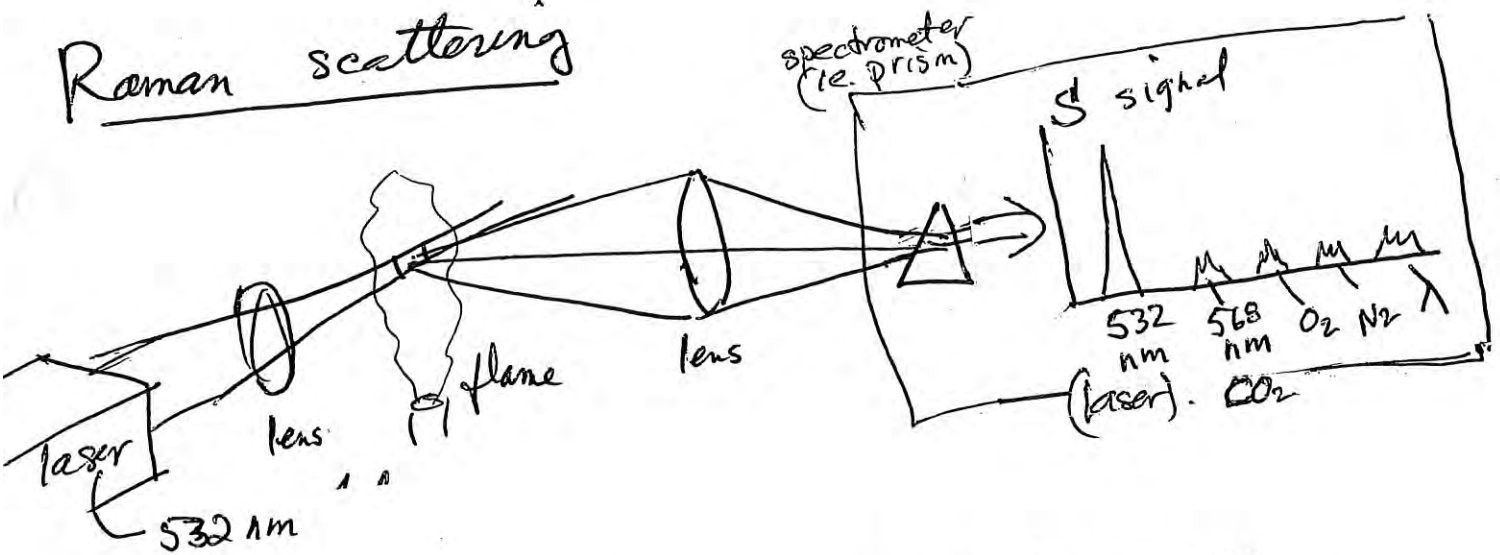
Fluorescence: absorption followed by spontaneous emission of a photon. Laser must be tuned to rotational line in absorption spectrum of one molecule, molecule jumps from ground state up to an allowed quantum level (absorption) then after 10^{-8} sec it spontaneously jumps down to a level higher than ground state. Emitted light is red shifted; amount of shift different for each type of molecule.



Fluorescence signal is much stronger than Raman
But only minor species fluoresce
Need only few milliwatts per laser pulse

Tunable laser required
Measure only ONE species with any one laser setup; need to retune and repeat for others

Raman scattering



consider the band of Raman scattered light from the CO_2 molecule. It is shifted 36 nm to the red

(larger wavelength) from the laser line
 ex. laser line $\lambda = 532 \text{ nm}$ (green) CO_2 band $\Rightarrow \lambda = 568 \text{ nm}$ (yellow)

Raman signal - formula is similar to Rayleigh scattering

$$S_{\text{CO}_2} = (\text{const}) \cdot I_{\text{laser}} \cdot n_{\text{CO}_2} \cdot \sigma_{\text{CO}_2} \cdot f(T)$$

signal from $\text{CO}_2 =$ light in band near 568 nm
 laser intensity
 # CO_2 molecules / volume
 scattering cross section for CO_2
 temp. affects band width

calibrate by recording signal S_{N_2} from N_2 of known n_{N_2}

$$\hookrightarrow n_{\text{CO}_2} = X_{\text{CO}_2} \frac{P}{kT}$$

$$\frac{S_{\text{CO}_2}}{S_{\text{N}_2}} = \frac{n_{\text{CO}_2}}{n_{\text{N}_2}} \frac{\sigma_{\text{CO}_2}}{\sigma_{\text{N}_2}}$$

Raman scattering

advantages

- get all major species (about 6) in each pulse
- good spatial resolution ($1\text{mm} \times 0.5\text{mm} \times 0.5\text{mm}$)
local, not line of sight
- laser pulse is 10nsec - good temporal resolution

disadvantages

- cannot do small concentrations, mole fractions $< 1\%$
- cannot do 2-D imaging, line Raman only
- probe volume must be 1mm long, cannot resolve

Kolmogorov scales

- must have a clean "blue" flame -
fuel can be: H_2 , CH_4 , DME, CO
fuel cannot be propane, ethylene, Jet A
- need large windows to collect very dim light
- cannot do sooty flames, particles, PIV, droplets
- some Raman scattering bands overlap
- powerful laser cracks glass windows

A significant body of results from this study were reported in Ref. 10, including scatter plots of measured scalars at various streamwise locations, mean values of the NO mole fraction conditional on mixture fraction, and overall NO emission values for the undiluted and diluted flames. In the present paper we focus on the relationships among NO, mixture fraction, and temperature by considering averages and rms fluctuations of the NO mole fraction conditional on: i) the mixture fraction alone and ii) both mixture fraction and temperature.

Conditional data analysis is a useful tool for investigating the influence of turbulent mixing on thermochemical states in flames. Processing the data conditional on the instantaneous mixture fraction yields quantitative information on turbulence-chemistry interactions that cannot be extracted from time- or Favre-averaging approaches. Double conditioning on mixture fraction and temperature (or some other reaction progress variable) allows a detailed look at the relationships among scalars under various conditions of local strain or departure from equilibrium. Some of the results in this paper are specifically relevant to the Conditional Moment Closure (CMC) model for turbulent combustion. However, the experimental results and conditional statistics presented here and in Ref. 10 provide a detailed basis for evaluating both the underlying assumptions and the predictive

accuracy of a variety of turbulent combustion models.

EXPERIMENTAL METHODS

Experiments were conducted in the Turbulent Diffusion Flame laboratory at the Combustion Research Facility. The flow facility and diagnostic systems have been described previously [10–12], and only a brief summary is included here. Spontaneous Raman scattering was used to measure concentrations of the major species, N_2 , O_2 , H_2 , and H_2O . The Rayleigh scattering signal was converted to temperature using a species-weighted scattering cross section, based on the Raman measurements. Rayleigh cross sections were derived from the survey of refractive indices by Gardiner et al. [13]. Linear laser-induced fluorescence (LIF) was used to measure NO and OH. Quantitative NO and OH concentrations were obtained by correcting these fluorescence signals on a shot-to-shot

basis for variations in the Boltzmann fraction and the collisional quenching rate, which were determined from the measured temperature and species concentrations. The NO data were also corrected for the temperature dependent effects of collisional line broadening. Mixture fraction was calculated from the measured species concentrations (moles/l) as

$$f = \frac{(w_{H_2} + \alpha w_{He})([H_2O] + [H_2]) + \left(w_H + \frac{\alpha}{2}w_{He}\right)[OH]}{w_{N_2}[N_2] + w_{O_2}[O_2] + (w_{H_2O} + \alpha w_{He})[H_2O] + (w_{H_2} + \alpha w_{He})[H_2] + \left(w_{OH} + \frac{\alpha}{2}w_{He}\right)[OH]}$$

where the w s are molecular weights and α is the mole ratio of helium to hydrogen in the fuel stream. Here, the helium-hydrogen ratio is assumed to be unaffected by differential diffusion. Note that other definitions of mixture fraction are possible [14].

The burner for the turbulent hydrogen flames was a straight tube (inner diameter, $d = 3.75$ mm and outer diameter 4.8 mm) centered at the exit of a vertical wind tunnel contraction. The beam from a flashlamp-pumped dye laser (532 nm, 5 Hz, ~ 750 mJ/pulse) was used for the Raman and

Rayleigh measurements. The NO and OH fluorescence measurements were accomplished using two separate Nd:YAG-pumped dye laser systems, which were fired approximately 1 and 2 μ s, respectively, before the Raman laser.

The output of one dye laser system was tuned to the $R_1(18)$ transition in the $A^2\Sigma^+ - X^2\Pi(0,0)$ band of NO. A solar-blind photomultiplier tube (PMT) and Schott UG-5 colored glass filters were used to collect NO fluorescence from the system of bands at 236, 247, 259, and 271 nm. The second dye laser system was tuned to the $O_{12}(8)$ transition in the $A^2\Sigma^+$

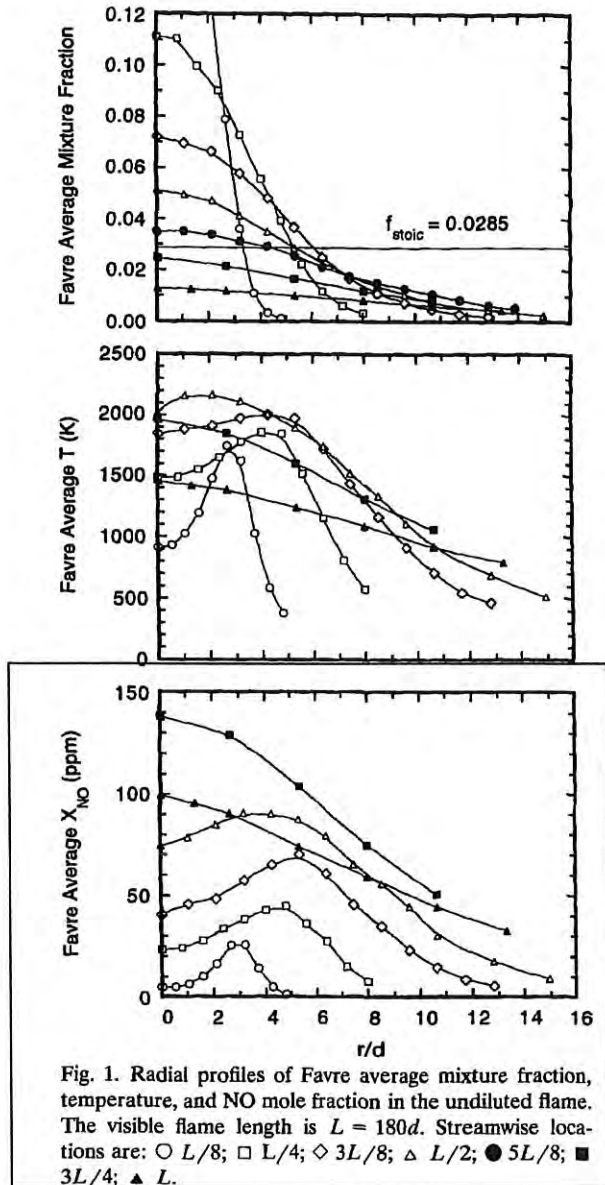


Fig. 1. Radial profiles of Favre average mixture fraction, temperature, and NO mole fraction in the undiluted flame. The visible flame length is $L = 180d$. Streamwise locations are: \circ $L/8$; \square $L/4$; \diamond $3L/8$; \triangle $L/2$; \bullet $5L/8$; \blacksquare $3L/4$; \blacktriangle L .

sensitive to local strain rates because of the combined effects of nonequilibrium chemistry and residence time. A high local strain rate means low temperature (relative to equilibrium) and short residence time at the NO forming conditions. Further downstream ($x = 3L/4, L$) scalar dissipation decreases, temperature and radical concentrations approach equilibrium, the high-temperature zones become broad, and instantaneous NO production rates at a given mixture fraction can be ex-

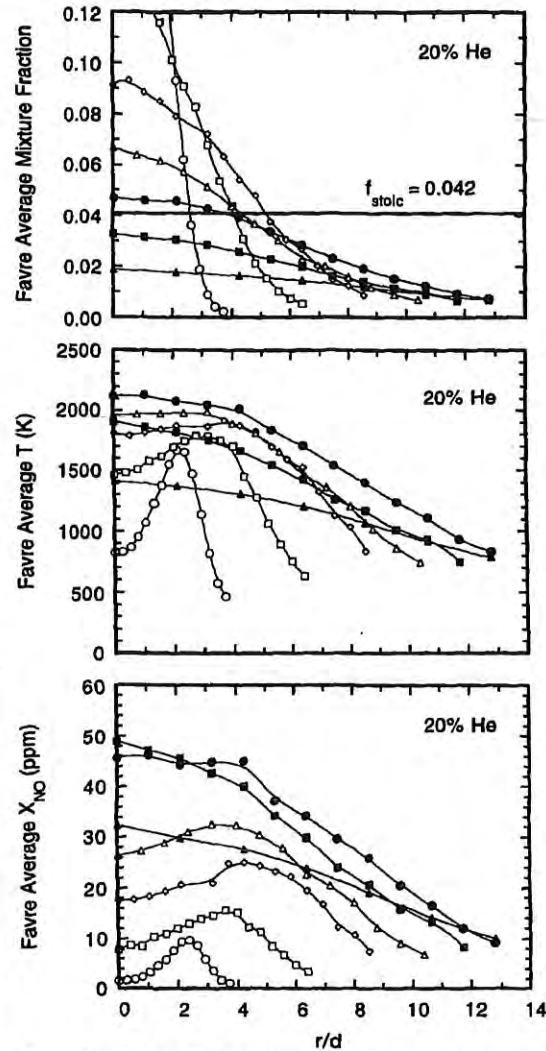


Fig. 2. Radial profiles of Favre average mixture fraction, temperature, and NO mole fraction in the 20% helium diluted flame. The visible flame length is $L = 150d$. Streamwise locations are: \circ $L/8$; \square $L/4$; \diamond $3L/8$; \triangle $L/2$; \bullet $5L/8$; \blacksquare $3L/4$; \blacktriangle L .

pected to approach the rate corresponding to equilibrium temperature and species concentrations. This streamwise evolution of reaction zone structure will be an important consideration as we examine conditional means and fluctuations of NO mole fraction.

Radial Dependence of the Conditional Means

A useful approach to quantifying the effects of turbulent mixing on thermochemical states in

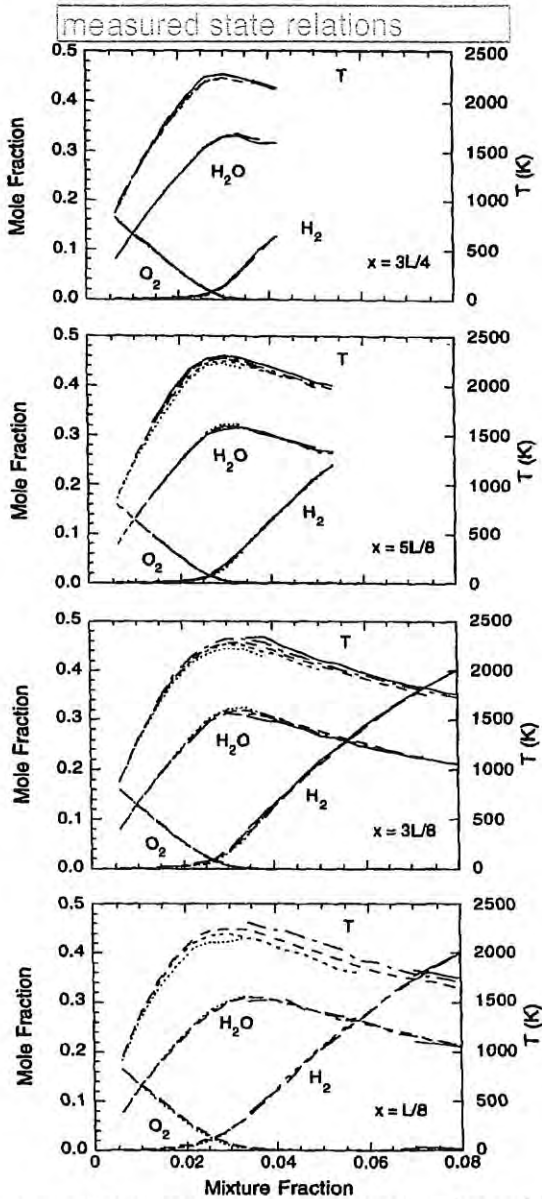


Fig. 4. Conditional mean temperatures and major species mole fractions calculated for each of five radial positions at four streamwise stations in the undiluted H₂ flame. In each plot the progression of line types (—), (---), (— · —), (--- · —), (— · · —) runs from a radial location on the fuel-rich side of the mean stoichiometric contour to a radial location on the fuel-lean side. Locations are listed in Table 2.

expect the conditional mean NO mole fraction, $\{X_{NO}\}_f$, to exhibit a radial dependence. Figure 5 shows results for $\{X_{NO}\}_f$ at different radial locations for each of six downstream stations in the undiluted flame. The curves are not smooth because fluctuations in X_{NO} are

TABLE 2
Radial Locations for Conditional Means Plotted in Figures 4 and 5^a

x/L	(—) r/d	(---) r/d	(— · —) r/d	(--- · —) r/d	(— · · —) r/d
3/4	0.0	2.7	5.3	8.0	10.7
	1.3	4.0	6.7	9.3	12.0
5/8	0.0	2.1	4.3	6.4	8.5
	1.1	3.2	5.3	7.5	9.6
1/2	3.2	5.3	6.4	7.5	10.7
					12.8
3/8	1.1	3.2	5.3	7.5	9.6
	2.1	4.3	6.4	8.5	10.7
1/4	0.8	2.4	4.0	5.6	7.2
	1.6	3.2	4.8	6.4	8.0
1/8	1.1	2.1	3.2	3.7	4.3
	1.6	2.7			

^a In most cases data from two adjacent measurement locations were combined to increase sample size.

greater than those in temperature or major species mole fractions and we have only 6000 to 8000 samples at each streamwise position. (Operational constraints of the flashlamp-pumped dye laser made the collection of substantially more samples at each location impractical.) Nevertheless, there are clear trends in the data. In the lower portion of the flame, at $x = L/2$ and below, there is a distinct radial dependence of the conditional mean NO mole fraction. Five curves are shown in each plot, with the solid curve corresponding to the measurement location farthest inside the mean stoichiometric contour and the dotted curve corresponding to the location farthest outside. (See Table 2 for exact locations.) For fuel-rich values of the mixture fraction, the solid curve is highest, and the conditional mean NO levels decrease with increasing radius. This is consistent with the temperature curves, which also decrease with increasing radius. Surprisingly, the conditional means of temperature and NO move in opposite directions for fuel lean values of the mixture fraction, and $\{X_{NO}\}_f$ increases with radius in spite of the decrease in $\{T\}_f$. The physical mechanisms that lead to this counterintuitive result are not obvious, but the implication is that, due to the relatively slow rate of thermal NO production, the convective history of fluid samples is more important than local conditions in determining measured NO levels.

CARS = Coherent Anti-Stokes Raman Spectroscopy

to measure temperature in sooty, droplet laden combustors

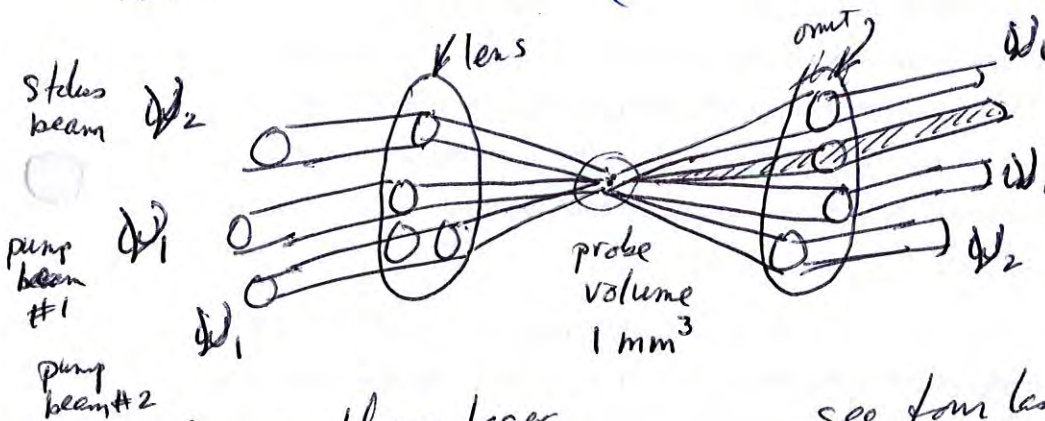
very accurate 1% = 20K at 2000K

temperature range = 800K to greater than 2500K

WPAFB has one on a cart - roll up to the experiment!

description: Lederman PECS 3, 1-34, 1977 (simple ideas)
 Hancock et al CNF 109, 323, 1997
 Roy et al. CNF 138, 273, 2004

3 laser beams in (focus) 4 laser beams out!



new beam collected on photodetector - give temperature for each laser pulse instantaneous point measurement

focus three laser beams at the probe volume
 - two at frequency ν_1
 - one at frequency ν_2

see four laser beams come out!
 - three that you put in
 - plus new coherent scattering beam at new frequency ν_3 = CARS beam

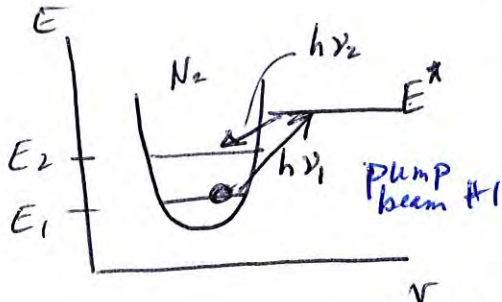
- 10^6 more than spontan. Raman
 - large amount of light in CARS beam = indicator of T
 - can collect all scattered light through small window
 need small window in + small window out
 - much more light collected than spontaneous Raman

Lederman (PECS) CARS = 2 Raman steps, in phase

Raman step #1

$$(\text{photon at } \nu_1) + \left(\begin{array}{l} N_2 \\ \text{molecule in} \\ \text{ground state} \\ E_1 \end{array} \right) = \left(\begin{array}{l} \text{raises } N_2 \\ \text{molecule to} \\ \text{excited state} \\ E_2 \end{array} \right) + \left(\begin{array}{l} N_2 \text{ gives off} \\ \text{a photon} \\ \text{at } \nu_2 \end{array} \right)$$

$$E_2 - E_1 = h(\nu_1 - \nu_2)$$



step #1 = spontaneous Raman, molecule begins in ground state, ends up in state 2

a) $E^* = E_1 + h\nu_1$

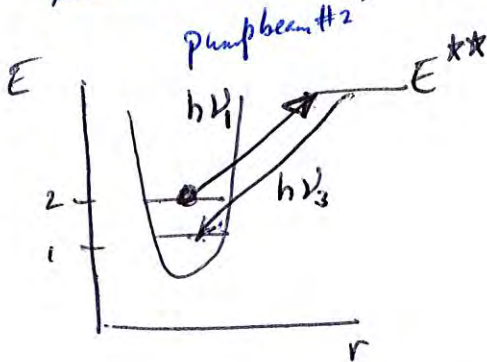
b) $E^* - E_2 = h\nu_2$

Raman step 2

now hit N_2 in excited state 2 with another photon spontaneous Raman, molecule

now begins excited state 2, ends up in ground state 1

"two photon process"



c) $E^{**} = E_2 + h\nu_1$

d) $h\nu_3 = E^{**} - E_1$

Therefore, from above eqns (a-d):

$$h\nu_3 = \overbrace{E^{**}} - E_1$$

$$= (E_2 - E_1) + h\nu_1$$

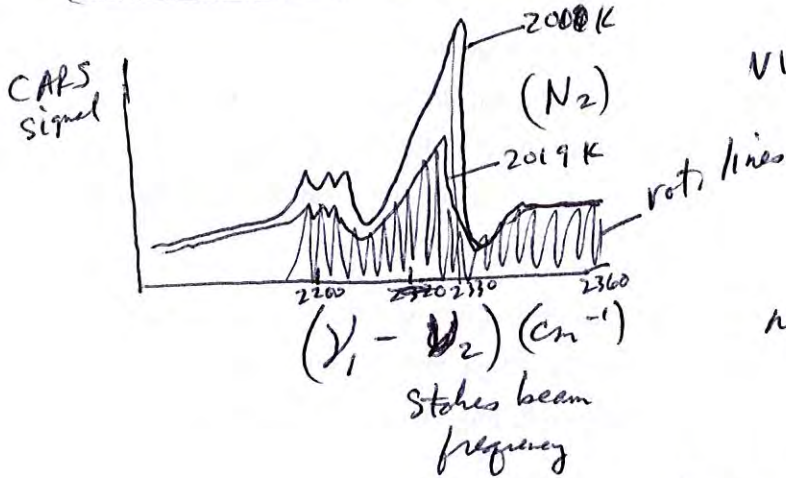
$$= h(\nu_1 - \nu_2) \text{ from a + b}$$

$$\boxed{\nu_3 = 2\nu_1 - \nu_2}$$

↑ ↑
frequency of CARS ~~beam~~ output laser beam (directed) $\nu_1, \nu_2 =$ frequencies of laser input beams

- If beams are phase-matched
- beam out is coherent
 - signal is 10^6 times spontaneous Raman

CARS beam has a spectral shape = one vibrational band of many rotational lines
 Eckbreth's book p. 302



vibrational band of rotational lines
 (light ν_3 band must be from N_2 - not from scattering off wells, windows)

note we said for Raman N_2
 $\Delta\nu = 2330 \text{ cm}^{-1}$

also some pressure dependence (but weak)

need spectral code to fit a calibrated spectrum at known T 's to measured spectrum - to



infer a measured T

assume: rotational state population is Maxwell-Boltzmann
 low $T \rightarrow$ only lower rotational levels populated
 high $T \rightarrow$ more of higher rotational levels populated

limitations

lowest T measurable = $\frac{800K}{}$

must cross three beams - but good thing is you get no signal if uncrossed - spectrum is correct if only partially crossed!

need small windows in + out - OK

very high power lasers (1 J/pulse)

work well in yellow flames with soot + drop

not if there is too many drops or particles

very careful alignment, expensive lasers, need PhD in diagnostics!

Ford GM WPAFB
DLR, Lund, Darmstadt
Heidelberg

CARS = Coherent Anti-Stokes Raman Spectroscopy

Textbooks:

1. Eckbreth AC. 1996. Laser Diagnostics for Combustion Temperature and Species. Amsterdam: Gordon & Breach. 596 pp. 2nd ed.
2. Kohse-Hoinghaus K, Jeffries JB. 2002. Applied Combustion Diagnostics. New York: Taylor & Francis. 705 pp.
3. Linne MA. 2002. Spectroscopic Measurement: An Introduction to the Fundamentals. New York: Academic. 414 pp.

Single point measurement of:

- a) Gas Temperature
- b) Concentrations of Fuels: ethylene, acetylene, methane, hydrogen,
- c) Concentrations of Major species: CO₂, H₂O, CO, O₂, N₂

Shine three laser beams in - to cross at the point of interest,

Light comes out in the form of a laser beam - strong, easy to collect, need only small window

Since signal out is strong and pulsed (10 nsec), works well with soot, sprays, bright yellow flames

Very accurate temperatures, to within 20 K out of 2000 K, = 1%

Used at Purdue, WPAFB Dayton, Edwards AFB in jet engines, rocket chambers

Difficult to operate, must be a laser expert

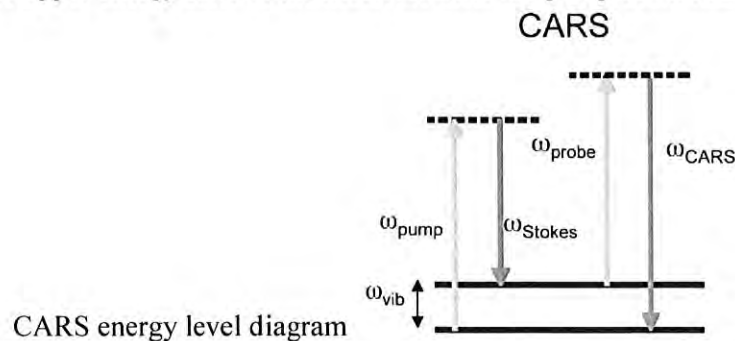
Must align three laser beams to cross, sometimes difficult

Expensive, lots of equipment needed

For clean flames – regular (spontaneous) Raman has better Signal to Noise, used at Sandia

For engines, complex fuels – CARS works better, used at AFRL

CARS is a third-order optical process involving three laser beams: a pump beam of frequency ω_p , a Stokes beam of frequency ω_s and a probe beam at frequency ω_{pr} . These three beams are represented by the three arrows on the left. The two black solid lines are the energy levels of the gas molecule. The dotted line is not an allowed quantum level, but is the upper energy state of the molecule after the pump beam hits it.



These three beams interact with the gas and generate a coherent optical beam that exits and is at the anti-Stokes frequency ($\omega_{pr} + \omega_p - \omega_s$). This output beam is represented by the green arrow. The latter is resonantly enhanced when the frequency difference between

the pump and the Stokes beams

$$(\omega_p - \omega_s) = \omega_{\text{vib}} \quad (1)$$

This frequency ω_{vib} is the energy in a vibrational level of the molecule, divided by Planck's constant (h). So the Pump beam can be any color, the Stokes beam must be tuned to a color to satisfy Eq. 1.

In 1965, a paper was published by two researchers of the Scientific Laboratory at the Ford Motor Company, P. D. Maker and R. W. Terhune, in which the CARS phenomenon was reported for the first time.

CARS can be explained by a (damped) harmonic oscillator with a characteristic frequency of ω_v . This oscillator is not driven by a single optical wave, but by the difference frequency $(\omega_p - \omega_s)$ between the pump and the Stokes beams instead. This driving mechanism is similar to hearing the low combination tone when striking two different high tone piano keys: your ear is sensitive to the difference frequency of the high tones.

Similarly, the Raman oscillator is susceptible to the difference frequency of two optical waves. When the difference frequency $\omega_p - \omega_s$ approaches ω_v , the oscillator is driven very efficiently. On a molecular level, this implies that the electron cloud surrounding the chemical bond is vigorously oscillating with the frequency $\omega_p - \omega_s$. These electron motions alter the optical properties of the sample, i.e. there is a periodic modulation of the refractive index of the material. This periodic modulation can be probed by a third laser beam, the probe beam. When the probe beam is propagating through the periodically altered medium, it acquires the same modulation. Part of the probe, originally at ω_{pr} will now get modified to $\omega_{pr} + \omega_p - \omega_s$, which is the observed anti-Stokes emission. Under certain beam geometries, the anti-Stokes emission may diffract away from the probe beam, and can be detected in a separate direction.

Line CARS = temperature and concentrations along a 2 mm line

Jim GORD, AFRL, Dayton: does CARS **line imaging** of temperature to 20 atm. pressure, Probe length = 2 mm

cross three sheets along a line, get one sheet out to camera

pump, probe (800 nm very red), stokes = 983 nm (IR), CARS output = 675 nm (red)

Gord uses a femtosecond pulse duration - why femtosec pulse = quenching-free, larger S/N, hi-rep (10 kHz)

Gord uses a TiSapphire laser for the pump and probe laser sheets, it is a Ti Sapphire Spectra Physics Solstice Laser (100 fs pulse width), 10 kHz rep rate

He uses a tunable Topas OPA laser, pumped by a Continuous Wave green diode laser for the third laser sheet - the Stokes laser sheet

He records the output laser sheet using a 10 kHz camera - since the three input laser sheets are operated at 10,000 pulses /sec

CARS and PLIF study of JP-8 combustion

This proposed Michigan effort will complement some ongoing CARS work of Drs. Jim Gord [3] and Terry Meyer [4]. Dr. Driscoll will perform fluorescence imaging of five species (JP-8, OH, formaldehyde, CO, toluene). Michigan 2-D PLIF will image the instantaneous edges of the pyrolysis, preheat and reaction zones shown in Fig. 1a

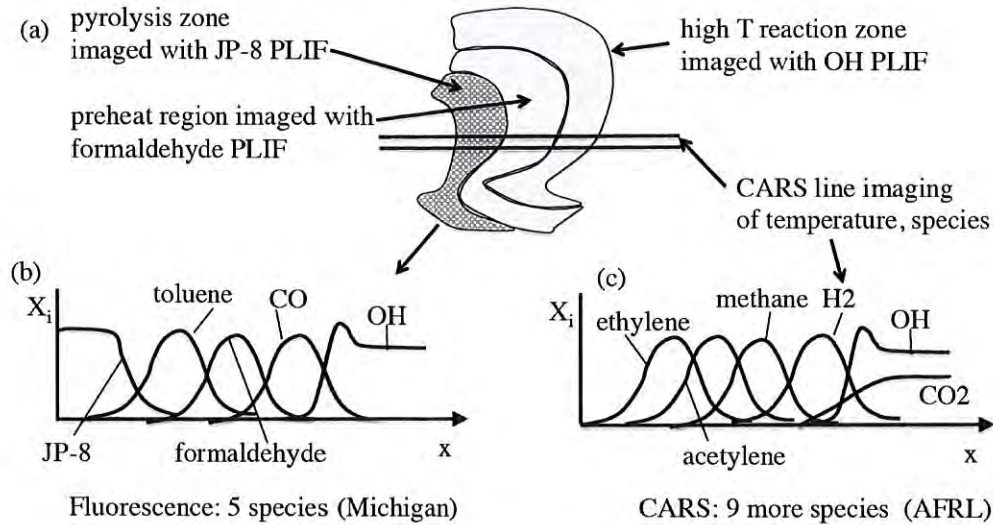


Figure 1. Pyrolysis, preheat, reaction zones will be identified from 2-D PLIF in turbulent flames at Michigan; CARS line imaging of nine other species will be developed at AFRL.

While the fluorescence imaging at Michigan will provide profiles of five important species, CARS is the only diagnostic that has the demonstrated ability to measure line profiles of nine other important species (ethylene, methane, H₂, O₂, CO₂, acetylene, H₂O, CO, N₂) for higher hydrocarbon fuels that create soot precursors, as demonstrated by Gord [3] and Meyer [4] and others. CARS temperature and the concentration profile of one (or two) species will be recorded along a line, simultaneously with three PLIF images (formaldehyde, OH and JP-8). This will be repeated for the other CARS species.

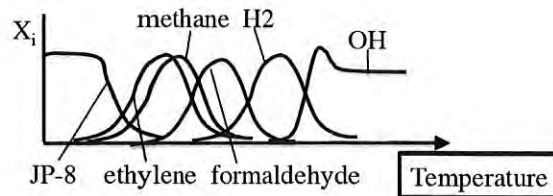


Fig. 1d. Statistically-averaged concentration profiles will be plotted versus gas temperature for one residence time, say 0.1 ms. Profiles such as these will be recorded for different values of residence time.

Dr. Jim Gord at AFRL plans to complete development of the optimum way to use CARS to simultaneously gas temperature and be repeated for different species (ethylene, methane, H₂, H₂O, CO₂, O₂, N₂, acetylene, CO).

CARS temperature line imaging: CARS is operational at AFRL [15] and has been used in JP-8 flames [22, 23, 27]. In addition, many studies at AFRL have demonstrated CARS concentration line imaging in flames for species 6-13: H₂, CH₄, CO₂, H₂O, CO, N₂, O₂ and acetylene [3,4,15-27]. Figure 2 shows some CARS single shot data; Gord et al. [3] measured H₂, O₂ and N₂ concentrations simultaneously with temperature. Meyer et al. [4] measured CO₂, O₂ and N₂ with temperature. In several cases the fuel used was JP-8 [22, 23, 27]. The instantaneous temperature measurements are estimated to have an accuracy of 97%, which is an uncertainty of 54 K at 1800 K [Meyer et al, 19].

	Species or temperature		Diagnostic		Location	Ref.
1	hydroxyl	OH	PLIF	2-D image	U. Michigan	1,7
2	formaldehyde	CH ₂ O	PLIF	2-D image	U. Michigan	1,7
3	JP-8	JP-8	PLIF	2-D image	U. Michigan	8-11
4	carbon monoxide	CO	LIF	line image	U. Michigan	12, 13
5	toluene	C ₇ H ₈	LIF	line image	U. Michigan	14
	temperature	T	PLIF (2-line)	2-D image	U. Michigan	12
	temperature	T	nsec-CARS	line image	AFRL*	15-29
6	hydrogen	H ₂	nsec-CARS	line image	AFRL	3
7	methane	CH ₄	nsec-CARS	line image	AFRL	17, 19
8	carbon dioxide	CO ₂	nsec-CARS	line image	AFRL	18
9	water	H ₂ O	nsec-CARS	line image	AFRL	17
10	carbon monoxide	CO	nsec-CARS	line image	AFRL	20
11,12	nitrogen, oxygen	N ₂ , O ₂	nsec-CARS	line image	AFRL	3
13	acetylene	C ₂ H ₂	nsec-CARS	line image	AFRL	24
14	ethylene	C ₂ H ₄	nsec-CARS	line image	AFRL	28, 29

Table 2. Species to be measured in the turbulent flames using CARS and PLIF. *A second Hi-Pilot burner will be located at AFRL but moved to Dr. Meyer's lab as necessary.

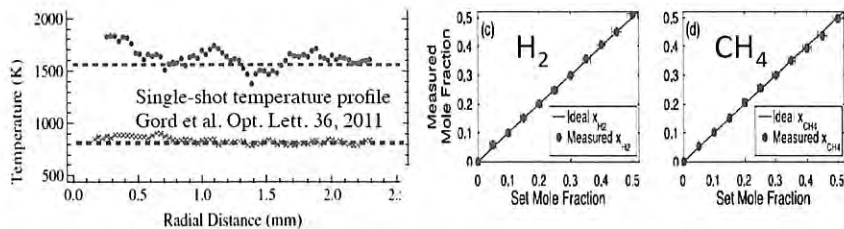


Fig. 2. CARS temperature profiles, concentration data of Drs. Gord [15] and Meyer [19].

Ethylene is listed in Table 2 as a ninth CARS species of interest because it is a major product of JP-8 pyrolysis. Fortunately, the CARS spectrum of ethylene has been

successfully recorded by Tedder [28] and by Santoro [29]. Tedder [28] states: "WIDE CARS is capable of simultaneously measuring temperature and mole fractions of ethylene, N₂, O₂, H₂, CO, and CO₂." She recorded the ethylene CARS spectrum, but only in a non-reacting gas mixture. Santoro [29] says: "non-resonant signals, i.e., background susceptibility from unburned ethylene, provide a measure of unburned ethylene concentrations in the flame". While these preliminary studies do not guarantee success in measuring ethylene concentrations in a JP-8 flame, they suggest that it may be possible so further research at AFRL is warranted.

Three additional species of interest that are not listed in Table 2 are: butane (C₄H₁₀), propene (C₃H₆) and butene (C₄H₈) which also are products of the pyrolysis of JP-8. It is suggested that AFRL make efforts to determine the feasibility of CARS line imaging of these species. Of course, obstacles are expected, including: (a) interferences between the hydrocarbons in the signal spectrum, (b) keeping the CARS beams overlapped for the 3-4 mm distances over which line images will be recorded, (c) obtaining sufficient signal-to-noise ratio, and (d) gating the cameras with short nanosecond gate times to remove unwanted flame radiation.

Task : Interact with Dr. Jim Gord and Dr. Terry Meyer on CARS diagnostics

At AFRL: Drs. Driscoll, Gord and Meyer have had several discussions. It was agreed that all three of us will plan to interact after we have submitted our plans separately to Dr. Chiping Li and have received approval. It is recommended that Drs. Gord and Meyer be funded to optimize their CARS line-imaging methods to measure concentrations and temperature. They have several possible methods and several possible lasers to use, so these details are not presented here. A repetition rate of 10 Hz is sufficient and it is desired to perform 1-D imaging along a line that is 4 mm long and to achieve maximum signal-to-noise. Their laser wavelengths should be optimized to avoid possible interferences from the various hydrocarbon species. They have published a very impressive list of papers; their papers, along with those of others, have shown that CARS has been used successfully with ethylene fuel and with Jet-A fuel [16, 22, 23, 27]. A promising method is the triple-pumped CARS method reported by Gord et al. [3]. They simultaneously recorded the concentrations of two target species (H₂ and O₂) along with gas temperature. They used two injection-seeded Nd:YAG lasers operating at 10 Hz to pump two narrowband dye lasers and a broadband dye laser while also providing a 532-nm CARS pump beam. The broadband dye laser was used to generate a Stokes beam for each of the four CARS signals, with a frequency spectrum centered near 607 nm. The two narrowband dye lasers were used to provide the pump beams for O₂ and H₂.

The proposed research plan is for Drs. Gord and Meyer, on separate AFOSR contracts, to repeat this triple-pumped CARS method in calibration burners within their labs, so that two species concentrations are measured along with temperature. This procedure will be done four times; each time two new species profiles will be recorded. The result will be line profiles of all nine species listed in Table 2 (CH₄, H₂, H₂O, CO₂, O₂, N₂, CO, acetylene and ethylene). It is sufficient to record two species and temperature simultaneously, and to later correlate the statistical averages of the various profiles with

temperature. It also may be possible to simultaneously record more than two concentrations along with temperature. For example, Tedder et al. [28] increased the spectral excitation bandwidth using a unique mixture of laser dye to simultaneously measure the concentrations of seven species, including ethylene. This approach also will be explored, but the method demonstrated by Gord and Meyer (two species simultaneously with temperature) is sufficient to meet our goals.

References

3. Gord, J. et al., Triple-pump CARS: temperature and multiple-species concentration measurements [N₂, O₂, H₂] in reacting flows, *Optic Commun.* 224, 131, 2003.
4. Meyer, T., Gord, J. et al., Dual-pump dual-broadband CARS for temperature and CO₂-O₂-N₂ measurements in gas-turbine combustors, *Comb Flame* 142 52, 2005
15. Gord, et al. One-dimensional single-shot thermometry in flames using femtosecond-CARS line imaging, *Optics Letters* 36, 21, 4182, 2011.
16. Meier et al., Experimental Analysis of Soot in a Gas Turbine Model Combustor [CARS temperature with ethylene fuel], *J. Engr. Gas Turb.* 133, 121503-1, 2011
17. Gord, et al. [Review of CH₄, H₂, O₂, N₂ CARS measurements] *Prog. Energy and Combust Sci.* 36, 280, 2010.
18. Gord, et al., Dual-Pump Coherent Anti-Stokes Raman Scattering Temperature and CO₂ Concentration Measurements, *AIAA J.* 41, 4, 679, 2003.
19. Meyer, T. et al, *Optics Lett* 39, 23, 6608, 2014.
20. Gord, J. et al, Chirped-probe-pulse f-sec CARS concentration measurements [of CO], *J. Opt. Soc. Amer. B* 30 ,1, 188, 2013.
21. O'Byrne, S., et al., Dual-Pump CARS [of H₂, O₂, N₂] in a Supersonic Combustor, *AIAA J.* 45,4, 922, 2007.
22. Meyer, T. and Gord, J., Temperature and CO₂ concentration measurements in...a liquid-fueled combustor [JP-8 Fuel], *Comb. Flame* 138, 273, 2004.
23. Meyer, T. and Gord, J., Dual-pump dual-broadband CARS for exhaust-gas temperature and CO₂-O₂-N₂ mole-fractions in model gas-turbine combustors [with Jet-A fuel], *Comb Flame* 142, 52, 2005.
24. Gord, J. et al., Detection of acetylene by CARS, *Appl. Phys B* 87, 731, 2007.
25. Gord, J., Pitz, R., Minor-species [H] structure of... tubular flames, *Proc Combust. Inst.* 35 1107, 2015.
26. Gord, J., Femtosecond two-photon LIF imaging of atomic species using a... Ti: sapphire laser, *Appl Phys B* 116, 7, 2014.
27. Thariyan, et al., Dual-pump CARS for temperature and species measurements in a high-pressure gas turbine combustor [Jet-A fuel], *Measur Sci Tech* 22, 015301, 2011.
28. Tedder et al., Width-increased dual-pump CARS, *Applied Optics* 49, 1305 (2010).
29. Lee, SY, Pal. S., Santoro, RJ, Temperature and unmixed fuel [ethylene] measurements in turbulent flames using CARS, *Chemical and Physical Processes in Combustion* (book) p. 107, Comb. Inst. Eastern States Section, 1997.

Dual-pump vibrational/rotational femtosecond/picosecond coherent anti-Stokes Raman scattering temperature and species measurements

Chloe E. Dedic,¹ Joseph D. Miller,² and Terrence R. Meyer^{1,*}

¹Iowa State University, Department of Mechanical Engineering, Ames, Iowa 50011, USA

²Air Force Research Laboratory, Aerospace Systems Directorate, Wright-Patterson AFB, Ohio 45431, USA

*Corresponding author: trm@iastate.edu

Received September 19, 2014; accepted October 16, 2014;

posted October 20, 2014 (Doc. ID 222788); published November 18, 2014

A method for simultaneous ro-vibrational and pure-rotational hybrid femtosecond/picosecond coherent anti-Stokes Raman scattering (fs/ps CARS) is presented for multi-species detection and improved temperature sensitivity from room temperature to flame conditions. N₂/CH₄ vibrational and N₂/O₂/H₂ rotational Raman coherences are excited simultaneously using fs pump pulses at 660 and 798 nm, respectively, and a common fs Stokes pulse at 798 nm. A fourth narrowband 798 nm ps pulse probes all coherence states at a time delay that minimizes nonresonant background and the effects of collisions. The transition strength is concentration dependent, while the distribution among observed transitions is related to temperature through the Boltzmann distribution. The broadband excitation pulses and multiplexed signal are demonstrated for accurate thermometry from 298 to 2400 K and concentration measurements of four key combustion species. © 2014 Optical Society of America

OCIS codes: (300.6230) Spectroscopy, coherent anti-Stokes Raman scattering; (320.7150) Ultrafast spectroscopy; (120.1740) Combustion diagnostics; (300.6290) Spectroscopy, four-wave mixing.

<http://dx.doi.org/10.1364/OL.39.006608>

Coherent anti-Stokes Raman scattering (CARS) spectroscopy has been used extensively for accurate, *in-situ* temperature and relative species concentration measurements in gas-phase samples to increase the understanding of chemical reactions pertinent to complex combustion processes [1]. Early efforts implemented CARS using nanosecond (ns) sources to excite vibrational or pure-rotational molecular transitions. To excite multiple species simultaneously, dual-broadband CARS was developed to study closely spaced Raman transitions using two broadband dye lasers [2]. Another technique, dual-pump CARS, uses two separate narrowband pump beams that can be tuned to excite a variety of molecule pairs [3]. Bengtsson *et al.* combined vibrational CARS and dual-broadband CARS to simultaneously excite and detect ro-vibrational and pure-rotational spectra [4]. This work was expanded on by Roy *et al.* to excite pure-rotational spectra of N₂ and O₂ and ro-vibrational spectra of N₂ and CO₂ to measure concentration and temperature within low- and high-temperature regions [5]. Tedder *et al.* increased the spectral excitation bandwidth using a unique mixture of laser dye to measure seven species within H₂/C₂H₄ combustion mixtures [6]. Recently, Satija and Lucht utilized a two-beam configuration to generate pure-rotational CARS and a third beam to probe N₂ ro-vibrational CARS, offering temperature measurements over a broad range using a simplified setup [7].

Challenges associated with ns CARS temperature and species measurements include low laser repetition rates, uncertainties due to nonresonant background [8], and collisional broadening at elevated pressures [9]. To isolate the resonant CARS signal from nonresonant background, picosecond [10] and femtosecond [11] laser sources have been used to temporally separate the probe and preparation pulses. To avoid complex coherent interferences that occur with broadband femtosecond excitation/detection of multiple species, an approach

that combines broadband, femtosecond excitation with narrowband, picosecond detection has been employed. This approach, hybrid femtosecond/picosecond (fs/ps) CARS, can be used to enhance chemical specificity [12,13], simplify spectral analysis, suppress nonresonant background, and reduce the effects of collisions for accurate thermometry from low to high pressures [14].

Hybrid fs/ps CARS has been used to probe the vibrational transitions of N₂ for high-speed measurements of temperature with a precision of 2.2% and error of 3.3% [15], but is limited to temperatures above ~1200 K due to low population of the N₂ hot bands. Additionally, pure-rotational CARS has been implemented to measure temperature with errors of 1.8% and 2.5% at 1400 and 2283 K, respectively, with spectral focusing and second-harmonic bandwidth compression of the ps probe [16]. Measurements of relative species concentrations have been accomplished using rotational or vibrational transitions of N₂/O₂ [16,17] or N₂/CH₄ [18], respectively, and the ability to excite multiple species, such as N₂, H₂, CH₄, and CO₂, has been demonstrated using ultra-broadband CARS with a supercontinuum source [19].

In this Letter, quantitative measurement of four species (N₂, O₂, CH₄, and H₂) is demonstrated along with thermometry over a wide range from 298 to 2300 K through simultaneous pure-rotational and ro-vibrational hybrid fs/ps CARS. The ability to measure multiple species concentrations and wide temperature variations with minimal interferences from nonresonant background and collisions is important in unsteady combustion and other gas-phase reacting flows. This approach can furthermore be expanded to include additional species by utilizing laser sources with significantly wider spectral bandwidth.

Hybrid fs/ps CARS is a nonlinear, four-wave-mixing process that utilizes 100-fs pump/Stokes pulses (ω_p/ω_s) to excite vibrational and/or rotational transitions of a

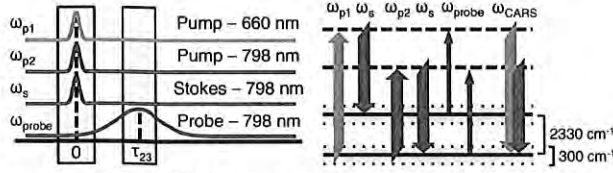


Fig. 1. CARS timing and frequency diagrams.

sample molecule. A third, frequency-narrowed picosecond pulse (ω_{probe}) is used to probe the molecular response. Simultaneous excitation of vibrational and rotational Raman coherences is accomplished using one Stokes beam, ω_s , at 798 nm and two pump beams, ω_{p1} and ω_{p2} , at 660 and 798 nm, respectively. A narrow-band pulse, ω_{probe} , at 798 nm is used to probe both Raman coherences and is delayed in time to suppress nonresonant interferences. The resulting frequency-resolved CARS signals contain ro-vibrational spectra and pure-rotational spectra. This configuration is shown in the time domain in Fig. 1(a) and frequency domain in Fig. 1(b).

Figure 1 only displays the excitation of vibrational and rotational N_2 transitions, but the same pulse arrangement also excites pure-rotational transitions of O_2 , the $S(0)$ pure-rotational transition of H_2 at 354 cm^{-1} , and the ν_1 vibrational transition of CH_4 at 2914 cm^{-1} because of the broadband pulses used. The frequency difference between the 660 nm pump and 798 nm Stokes pulses is centered between the N_2 and CH_4 Q-branch transitions [18].

As discussed by Engel *et al.* [18], the molecular number density can be related to the CARS signal by Eq. (1) for well-separated transitions:

$$N_i \propto \frac{\sqrt{I_{\text{CARS}}|_i}}{A_i \sqrt{I_{\text{NR}}|_i \left(\frac{d\sigma}{d\Omega}\right)_i}} \quad (1)$$

Here, $I_{\text{CARS}}|_i$ is the CARS intensity of species i , A_i is an experimental constant, and $(d\sigma/d\Omega)_i$ is the relative Raman cross section. $I_{\text{NR}}|_i$ represents the excitation efficiency of species i since the excitation energy has the same spectral characteristics as the nonresonant CARS intensity as measured within a cell of argon. For a mixture of n species, the mole fraction of species i can be described by

$$x_i = \frac{N_i}{\sum_{j=1}^n N_j} \quad (2)$$

Combining Eqs. (1) and (2) and consolidating the excitation energy, the Raman cross section, and the experimental constant for each species into constants K_i , which can be determined based on a calibration curve, the measured mole fraction for one species is defined by

$$x_i = \frac{K_i \sqrt{I_{\text{CARS}}|_i}}{\sum_{j=1}^{n-1} K_j \sqrt{I_{\text{CARS}}|_j} + \sqrt{I_{\text{CARS}}|_n}} \quad (3)$$

In this work, Eq. (3) is used to calculate mole fractions of CH_4 and H_2 within a mixture of N_2 , CH_4 , and H_2 . To relate CH_4 to H_2 , which are simultaneously excited but collected separately, Q-branch transitions are normalized to the $\nu(\text{N}_2)$ transition, and S-branch transitions are normalized to the $\text{N}_2(J=8)$ transition. Because N_2 is nearly inert in combustion reactions, it is an excellent candidate to relate species detected separately. The measurement of O_2 mole fraction within a mixture of N_2 and O_2 is also achieved utilizing Eq. (3). In addition, a method for measuring mole fraction with non-isolated N_2/O_2 lines is also investigated for enhancing accuracy at low O_2 mole fractions and for use when isolated lines are unavailable.

In addition to mole fraction, temperature is measured using vibrational and rotational CARS spectra. A time- and frequency-resolved model based on fundamental spectroscopic constants and experimental parameters was used to generate N_2 ro-vibrational and N_2/O_2 rotational spectra at various temperatures as implemented by Miller and co-workers [15,20] and described in detail by Stauffer *et al.* [21] and Prince *et al.* [12]. Best-fit temperatures were computed using a spectral library and optimization algorithm to minimize the residual between experimental and modeled spectra.

The experimental arrangement is modified from previously published studies [15,20]. A Ti:sapphire, regeneratively amplified, 1-kHz-rate laser (Solstice, Spectra-Physics) is used to produce a 2.5 mJ, 150 cm^{-1} , 100 fs pulse centered around 798 nm. 1.5 mJ is directed into a variable-bandwidth 4-f pulse shaper. The output, ω_{probe} , is used as the probe pulse for both rotational and vibrational fs/ps CARS. During this work, a 2.5 cm^{-1} Gaussian probe pulse was selected to provide sufficient spectral resolution for rotational CARS and adequate energy to perform vibrational CARS at high temperature.

The remaining 1 mJ from the source is used to pump an optical parametric amplifier (TOPAS, Spectra-Physics). The output of the OPA is frequency doubled using a second-harmonic-generation crystal, and the wavelength can be tuned to excite transitions of multiple molecules as the vibrational pump pulse, ω_{p1} . The residual of the OPA is split using a 50/50 beam splitter. One-half of the beam is used as the Stokes pulse, ω_s , while the other half is used as the rotational CARS pump beam, ω_{p2} . The frequency difference between ω_{p1} and ω_s corresponds to vibrational transitions of N_2 and CH_4 , and the difference between ω_{p2} and ω_s corresponds to pure-rotational transitions of N_2 , O_2 , and H_2 . A BOXCARS phase-matching configuration is used, with the two pump beams, ω_{p1} and ω_{p2} , aligned collinearly. The probe pulse is delayed in time (τ_{23}) relative to the preparation pulses to suppress nonresonant background. The resulting collinear pure-rotational and ro-vibrational CARS signals can be directed to a 0.303 m spectrometer (Shamrock SR-3031, Andor) and resolved separately using a 1200 line/mm grating and an electron-multiplied CCD camera (DU-970 P-UVB, Newton).

The simultaneous dual-pump vibrational/rotational fs/ps CARS technique was used to measure mole fractions of CH_4 and H_2 in a $\text{CH}_4/\text{H}_2/\text{N}_2$ mixture within a 298 K flow cell. The same cell was used to study a binary mixture of O_2 and N_2 at concentrations simulating O_2

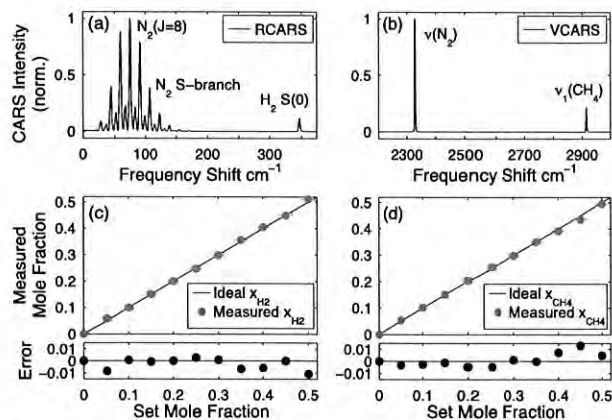


Fig. 2. Sample (a) H_2/N_2 spectra, (b) CH_4/N_2 spectra, and measured mole fractions of (c) H_2 and (d) CH_4 .

consumption during a reaction. To test the system capability for thermometry, CARS measurements were performed within the product stream of an adiabatic H_2 -air Hencken burner flame over a range of fuel/air equivalence ratios (60 SLPM typical H_2 -air flow rate).

Figure 2 shows sample CARS spectra recorded within a mixture of 50% N_2 , 30% H_2 , and 20% CH_4 at a probe delay of 12 ps. As discussed earlier, the intensities of the $\nu_1(\text{CH}_4)$ and $\nu(\text{N}_2)$ vibrational transitions and the $\text{N}_2(J=8)$ and $\text{H}_2 S(0)$ pure-rotational transitions be used to calculate the respective mole fractions. Figure 2 also displays the measured mole fractions versus the set mole fractions of H_2 and CH_4 . The horizontal error bars represent the uncertainty of the set mole fractions attributable to the mass-flow controllers. The experimental constant, K , for H_2 and CH_4 is 1.82 and 0.92, respectively. The absolute error associated with the concentration measurement is shown at the bottom of Fig. 2 and is less than 0.011 for H_2 and 0.013 for CH_4 for mole fractions between 0.05 and 0.50.

Due to the well-separated nature of the $\nu_1(\text{CH}_4)$ and $\nu(\text{N}_2)$ transitions and the $\text{N}_2(J=8)$ and $\text{H}_2 S(0)$ transitions, measuring mole fractions of CH_4 , H_2 , and N_2 within a gas mixture is relatively straightforward. However, O_2 and N_2 rotational transitions are spectrally overlapped at atmospheric conditions, resulting in a complex spectrum. Frequency beating between overlapping transitions can be observed by delaying the probe pulse in time, as highlighted by the experimental time-frequency plot in Fig. 3(a). For the purposes of this study the probe was set to a fixed delay of 12.5 ps [Fig. 3(a) red line], and the resulting spectra at varying concentrations of O_2 and N_2 are shown in Fig. 3(b). Initially the gas cell was filled with air [Fig. 3(b) dark blue line plot] and the N_2 concentration was increased incrementally until the cell contained 100% N_2 [Fig. 3(b) red dashed line plot]. This concentration range spans typical combustion conditions. The line positions for N_2 and O_2 S-branch transitions were calculated and are shown in Fig. 3(c).

The following analysis demonstrates two methods for measuring the O_2 concentration. To calculate O_2 mole fractions similar to the previous calculations for CH_4 and H_2 , well-separated N_2 and O_2 transitions must be

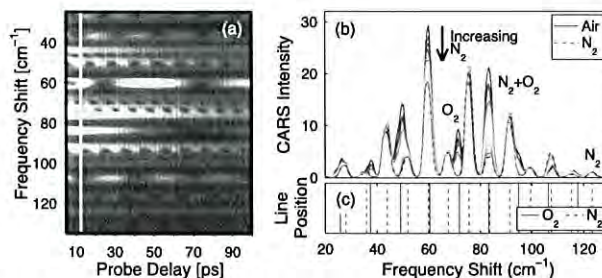


Fig. 3. (a) Experimental time-frequency plot of fs/ps RCARS in air at 298 K, (b) RCARS spectra of N_2/O_2 at time delay indicated by white line in (a) normalized to the $\text{N}_2(J=14)$ transition with concentrations varying from air to pure N_2 , and (c) calculated N_2/O_2 line positions.

available. As evident from the line positions in Fig. 3(c), a separated $\text{N}_2(J=14)$ transition exists near 123 cm^{-1} . This transition can be considered separated because its intensity decays as a simple exponential function in time. In Fig. 3(b) all spectra are normalized to this transition. There is a near-separated $\text{O}_2(N=11)$ transition at 72 cm^{-1} , but its response is an exponential decay with an oscillating amplitude, indicating slight overlap with the adjacent N_2 transitions. However, this transition was compared to the $\text{N}_2(J=14)$ line, and Eq. (3) was used to calculate O_2 mole fraction. The results of this calculation for O_2 mole fractions up to 0.21 are shown in Fig. 4(a), where K_{O_2} is 0.08 and the horizontal error bars associated with uncertainty of the set mole fractions are within the symbols. The measurement error is better than 0.011 for O_2 mole fractions greater than 0.04 but increases substantially at lower concentrations.

Mole fraction information can also be found by considering the nearly overlapped $\text{O}_2(N=13)$ and $\text{N}_2(J=9)$ transitions near 83.5 cm^{-1} , with a central frequency separation of 0.2 cm^{-1} . As shown in Fig. 3(b), the transition from air to pure N_2 results in a simple decrease in the line intensity with no appreciable shift in the peak spectral location or change in line shape. This mixed spectral feature was compared to the $\text{N}_2(J=14)$ line and the result as a function of theoretical mole fraction is shown in Fig. 4(b). These results fit well to a second-order polynomial, as indicated in Eq. (4), where p_1 , p_2 , and p_3 are coefficients determined using a least squares fitting routine and R is defined in Eq. (5). This relationship can be used as a secondary method of measuring O_2 mole fraction with reduced error at low mole fractions:

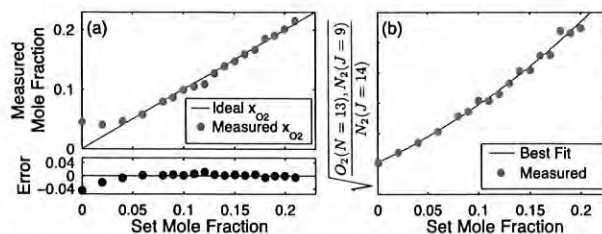


Fig. 4. (a) Measured O_2 mole fraction calculated from a nearly isolated O_2 transition. (b) Calibration curve shown with polynomial fit for overlapped N_2 and O_2 transitions.

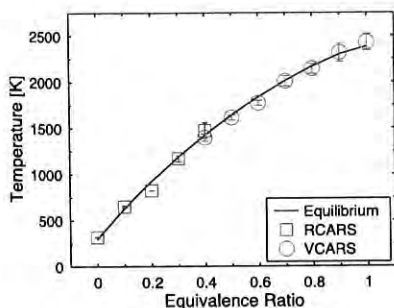


Fig. 5. Equivalence ratio curve showing the temperature fitting results for RCARS and VCARS compared to the adiabatic flame temperature.

$$x_{O_2} = p_1 R^2 + p_2 R + p_3, \quad (4)$$

$$R = \left(\frac{\sqrt{I_{\text{CARS}}|_{O_2(N=13), N_2(J=9)}}}{\sqrt{I_{\text{CARS}}|_{N_2(J=14)}}} \right). \quad (5)$$

Although the measurement of O_2 mole fraction is shown within a simple binary mixture, this measurement can be performed within a sample of N_2 , O_2 , CH_4 , and H_2 using the same procedure but normalizing all pure-rotational spectra to the well-separated $N_2(J=14)$ transition.

Dual-pump vibrational/rotational fs/ps CARS was performed within a H_2 -air flame for fuel/air equivalence ratios (ϕ) between 0.1 and 1.0 and at room temperature to evaluate the accuracy of the technique for thermometry over a wide range of temperatures. The results of these measurements are shown in Fig. 5; the vertical error bars represent one standard deviation due to the variation of best-fit temperatures for 100 time-averaged spectra. The probe pulse was delayed 7.5 ps from the preparation pulses to minimize nonresonant background and perform the temperature measurement before collisional line broadening becomes significant. The RCARS and VCARS temperature measurements at $\phi = 0.4$ agree within one standard deviation verifying the assumption of rotational and vibrational equilibrium. The solid line represents the calculated adiabatic flame temperature assuming equilibrium-combustion products. Typical accuracies for the temperature range in Fig. 5 are 95% and 98% for RCARS and VCARS measurements, respectively. The larger error in RCARS measurements is due to error in the theoretical modeling of overlapping O_2 and N_2 rotational transitions and requires further evaluation. However, this work demonstrates the feasibility for using dual-pump vibrational/rotational fs/ps CARS for thermometry in combustion environments.

In summary, this Letter demonstrated a dual-pump hybrid fs/ps CARS system that can simultaneously excite ro-vibrational and pure-rotational transitions of multiple molecules. This system can be used to detect vibrational spectra of N_2 and CH_4 and rotational spectra

of N_2 , O_2 , and H_2 for concentration measurements and thermometry over a wide range (298–2400 K). Accuracies are similar to that of ns CARS measurements of single species or over narrower temperature ranges. Moreover, these measurements are insensitive to collisions, independent of nonresonant background, and can be performed with higher repetition-rate laser sources. Future concentration measurements could be extended to include simultaneous vibrational excitation and measurement of CO and CO_2 through the use of a laser source with wider spectral bandwidth. Additionally, simultaneous excitation of ro-vibrational and pure-rotational energy states could be used to explicitly study vibrational-rotational nonequilibrium distributions.

Funding was provided by the Air Force Office of Scientific Research (Dr. Chiping Li, Program Manager) and the National Science Foundation (CBET-1056006, Dr. A. Atreya and R.-H. Chen, Program Directors). C. Dedic was supported by the National Science Foundation Graduate Fellowship Program.

References

- S. Roy, J. R. Gord, and A. Patnaik, *Prog. Energ. Combust.* **36**, 280 (2010).
- A. C. Eckbreth and T. J. Anderson, *Appl. Opt.* **24**, 2731 (1985).
- R. P. Lucht, *Opt. Lett.* **12**, 78 (1987).
- P.-E. Bengtsson, L. Martinsson, and M. Alden, *Appl. Spectrosc.* **49**, 188 (1995).
- S. Roy, T. R. Meyer, R. P. Lucht, M. Afzelius, P.-E. Bengtsson, and J. R. Gord, *Opt. Lett.* **29**, 1843 (2004).
- S. A. Tedder, J. L. Wheeler, A. D. Cutler, and P. M. Daney, *Appl. Opt.* **49**, 1305 (2010).
- A. Satija and R. P. Lucht, *Opt. Lett.* **38**, 1340 (2013).
- A. C. Eckbreth and R. J. Hall, *Combust. Sci. Technol.* **25**, 175 (1981).
- T. Seeger, F. Beyrau, A. Brauer, and A. Leipertz, *J. Raman Spectrosc.* **34**, 932 (2003).
- S. Roy, T. R. Meyer, and J. R. Gord, *Appl. Phys. Lett.* **87**, 264103 (2005).
- J. R. Gord, T. R. Meyer, and S. Roy, *Annu. Rev. Anal. Chem.* **1**, 663 (2008).
- B. D. Prince, A. Chakraborty, B. M. Prince, and H. U. Stauffer, *J. Chem. Phys.* **125**, 044502 (2006).
- D. Pestov, R. K. Murawski, G. O. Ariunbold, X. Wang, M. C. Zhi, A. V. Sokolov, V. A. Sautenkov, Y. V. Rostovtsev, A. Dogariu, Y. Huang, and M. O. Scully, *Science* **316**, 265 (2007).
- J. D. Miller, C. E. Dedic, S. Roy, J. R. Gord, and T. R. Meyer, *Opt. Express* **20**, 5003 (2012).
- J. D. Miller, M. N. Slipchenko, T. R. Meyer, H. U. Stauffer, and J. R. Gord, *Opt. Lett.* **35**, 2430 (2010).
- S. P. Kearney, *Appl. Opt.* **53**, 6579 (2014).
- S. P. Kearney, D. J. Scoglietti, and C. J. Kliewer, *Opt. Express* **21**, 12327 (2013).
- S. R. Engel, J. D. Miller, C. E. Dedic, T. Seeger, A. Leipertz, and T. R. Meyer, *J. Raman Spectrosc.* **44**, 1336 (2013).
- A. Bohlin and C. J. Kliewer, *Appl. Phys. Lett.* **104**, 031107 (2014).
- J. D. Miller, S. Roy, M. N. Slipchenko, J. R. Gord, and T. R. Meyer, *Opt. Express* **19**, 15627 (2011).
- H. U. Stauffer, J. D. Miller, M. N. Slipchenko, T. R. Meyer, B. D. Prince, S. Roy, and J. R. Gord, *J. Chem. Phys.* **140**, 024316 (2014).



CARS

Chirped probe pulse femtosecond coherent anti-Stokes Raman scattering thermometry at 5 kHz in a Gas Turbine Model Combustor

Claresta N. Dennis^{a,*}, Carson D. Slabaugh^a, Isaac G. Boxx^b, Wolfgang Meier^b, Robert P. Lucht^a

^a School of Mechanical Engineering, Purdue University, 585 Purdue Mall, West Lafayette, IN 47906, USA

^b German Aerospace Center (DLR), Institute of Combustion Technology, Pfaffenwaldring 38-40, 70569 Stuttgart, Germany

Available online 5 July 2014

Abstract

Single-laser-shot temperature measurements at 5 kHz were performed in a model gas turbine combustor using femtosecond (fs) coherent anti-Stokes Raman scattering (CARS). The combustor was operated at a global equivalence ratio of 0.65 and 10 kW thermal power. Measurements were performed at various locations within the flame in order to resolve the spatial flame structure and compare to previously published studies. Power spectral density analysis of the temperature measurements yielded the characteristic thermoacoustic pulsation frequency previously reported at 308 Hz. These results demonstrate the usefulness of fs-CARS for the investigation of highly turbulent combustion phenomena. The spatial resolution of the single-laser shot temperature measurements was approximately 600 μm, the precision was approximately ±2%, and the estimated accuracy was approximately ±3%. The dynamic range was sufficient for temperature measurements ranging from 300 K to 2400 K, although some detector saturation was observed for low temperature spectra.

© 2014 The Combustion Institute. Published by Elsevier Inc. All rights reserved.

Keywords: Laser diagnostics; Coherent anti-Stokes Raman scattering; Ultrafast spectroscopy; Gas turbine combustion; Turbulent swirl flame

1. Introduction

Coherent anti-Stokes Raman scattering (CARS) spectroscopy has been applied extensively for gas phase combustion diagnostics. Many literature reviews and textbooks describe CARS

theory in extensive detail, describing experimental and theoretical spectral modeling techniques. A 2010 survey of applications of CARS spectroscopy for reacting flow diagnostics highlights the many potential advantages of fs-CARS over traditional ns- and ps-CARS techniques [1]. Solid-state femtosecond lasers operate at high repetition rates and offer excellent shot-to-shot spectral stability, nearly eliminating the shot-to-shot spectral fluctuations encountered with typical broadband

* Corresponding author.

E-mail address: cn1@me.msu.edu (C.N. Dennis).

dye lasers used for nanosecond CARS. In addition, the nearly Fourier-transform limited broadband femtosecond laser pulses excite many Raman transitions at once, creating a strong coherence in the sample medium [2,3]. This allows fs-CARS temperature measurements based on the frequency-spread dephasing rate after initial excitation of the Raman coherence of the molecule by the pump and Stokes beams. If one uses a chirped-probe-pulse (CPP), a method introduced by Lang and Motzkus [4], the temporal decay of the Raman coherence can be mapped with linear and nonlinear contributions onto the frequency of the CARS signal allowing single-laser-shot measurements. Experiments have shown the CARS signal is nearly independent of molecular collisions after the initial excitation of the coherence and the initial decay rate of the Raman coherence in gas phase measurements depends only on temperature [5,6]. Focusing on the first few picoseconds after excitation will result in collision-free measurements for pressures up to 20 bar [3]. This simplifies significantly the theoretical modeling of fs-CARS spectra and improves accuracy by eliminating the need for Raman line-width information [1].

Since the review by Roy et al. [1], studies have demonstrated the improved accuracy of fs-CARS thermometry of reacting flows. Richardson et al. demonstrated excellent precision of the fs-CARS technique for flame measurements, with standard deviations of 1–1.5% of the mean temperature over a wide range of operating conditions [7]. Measurements were performed in a driven non-premixed hydrogen-air flame with nitrogen coflow and a turbulent methane-air Bunsen burner flame. Bangar et al. reported CPP fs-CARS temperature measurements of a hydrogen-air jet diffusion flame at 5 kHz [8]. They were able to resolve temperature fluctuations occurring due to Kelvin-Helmholtz instabilities and vortices present from the interaction of hot combustion gases and cold ambient air. Measured temperatures ranged from 400 to 2500 K with 2% standard deviation.

CPP fs-CARS has previously been applied only in mildly turbulent flames [7,8]. The purpose of the present work is to demonstrate the application of 5 kHz CPP fs-CARS thermometry to swirl stabilized model combustors with very high levels of turbulence. In collaboration with the German Aerospace Center (DLR), measurements were performed on the DLR Dual-Swirl Gas Turbine Model Combustor (GTMC). The GTMC is a research-scale swirl burner designed to study thermo-acoustic oscillatory effects on combustion chemistry for technically relevant operating conditions. The burner has been extensively characterized previously for various global equivalence ratios and thermal powers using planar laser-induced fluorescence (PLIF) of OH, CH and H₂CO, laser Doppler anemometry (LDA), OH*

chemiluminescence imaging, Raman scattering, two-line OH PLIF thermometry, and stereoscopic particle image velocimetry (PIV) [9–16]. The presence of an inner and outer recirculation zone and a precessing vortex core (PVC) has been well documented. A study by Weigand et al. [14] showed that mixing of hot products from the recirculation zones with the fresh gas influences the heat-release rate and the reacting flow-field, leading to induced periodic motions of the inner and outer recirculation zones. A more recent study was reported by Boxx et al. [16]. They obtained spatial and temporal frequency content from 5 kHz simultaneous stereoscopic PIV and OH-PLIF measurements and showed that the reaction zone conforms to the passage of large scale vortex structures associated with the PVC present within the flow-field.

In this study, CPP fs-CARS measurements were successfully performed throughout the highly turbulent reacting flow field of the GTMC. The measurements revealed very different temporal structure at different points in the flow. Power spectral density analysis was performed on the resulting temperature measurements to compare with previous studies. The spatial resolution of the technique was measured and found to be much better than previously reported for ns-CARS experiments. The accuracy and precision of these results is estimated to be within 3%. Beam steering effects were minimal and not significant to the point that single-shot spectra could not be analyzed; no loss of signal was experienced.

2. Experimental system

2.1. Femtosecond CARS optical system

For this experiment, the fundamental output of a 2 mJ, 5 kHz, 50 fs Ti:Sapphire regenerative amplifier (Legend Elite Duo, Coherent, Inc.) was used to pump an optical parametric amplifier (OPA) and also to provide the laser pulses for the CARS probe and Stokes beams (Fig. 1). Beam splitters were used to direct 90% of the amplifier energy to pump the OPA, 6% through a dispersive rod (30 cm, SF-10) to produce the chirped probe beam, and the remaining 4% to be used directly as the Stokes beam. The spectral bandwidths of the pump, Stokes, and CPP beams full width at half-maximum (FWHM) were 264 cm⁻¹, 406 cm⁻¹, and 422 cm⁻¹, respectively.

For the CPP fs-CARS experiments, the spatial and temporal overlap among the pump, Stokes, and probe beams are critical. All three beams were focused to the probe volume using a 200-mm plano-convex lens in a phase-matched, folded BOX-CARS geometry with a crossing angle of approximately 3° [17]. At the probe volume, spatial overlap was achieved by focusing all three beams through a 50 μm pinhole. Temporal

10-15
S

5-26

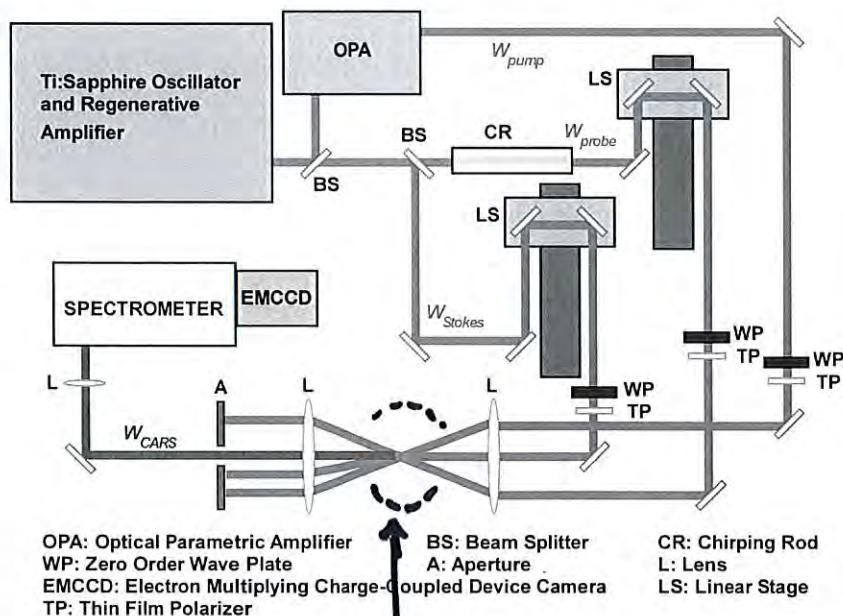


Fig. 1. Schematic diagram of CPP fs-CARS experimental system.

experiment

overlap was confirmed by placing a 100 μm thick Type-I BBO crystal at the probe volume and carefully adjusting the optical path lengths of the CPP and Stokes pulses using linear translation stages to maximize the intensity of sum-frequency signals generated from the combined beams.

The probe volume length was determined by translating the BBO crystal through the CARS probe volume along the propagation direction of the three laser beams. The nonresonant CARS signal generated inside the crystal was recorded and the CARS signal strength versus crystal position is shown in Fig. 2. The probe volume length was approximately 400 μm, corresponding to the FWHM, or 600 μm for the 10% to 10% of the maximum. The diameter of the probe volume

was approximately 50 μm. The excellent spatial resolution of these measurements is probably due to the low beam divergence and excellent Gaussian mode quality of the ultrafast laser.

The CPP fs-CARS signal beam, generated by the combination of spatially and temporally overlapped CPP, Stokes, and pump pulses, was then focused onto the entrance slit of a 0.25 m spectrometer. The CARS spectra were recorded using an electron multiplying charged coupled device (Andor iXon EMCCD) equipped with an optical mask to limit the signal illumination region to the bottom 50 rows of pixels. The CCD was vertically binned across the bottom 50 rows to allow for image acquisition at 5 kHz.

2.2. Calibration flame

The ‘Hencken burner’ is a commonly used reference flame for combustion diagnostics [18]. The burner top is 37.5-mm-square and consists of a central burner plate with a fine honeycomb structure through which the oxidizer flows. Fuel is carried by hypodermic needles which protrude just above the honeycomb structure. Downstream of the burner face, the fuel and oxidizer flows rapidly mix and combust to produce a uniform flow of product gases.

For this experiment, the Hencken burner was used to produce stable, near adiabatic H₂-air flames. Digital mass flow controllers were calibrated and used to control the volumetric flow rates of each of the gases. Hydrogen-air equivalence ratios of 0.3, 0.5, and 0.8 provided

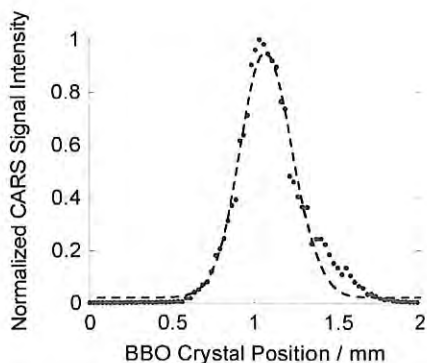


Fig. 2. CARS probe volume length measurement.

5-27

temperature standards at 1189, 1643, and 2168 K respectively. These standard temperatures were measured using the combined pure rotational/pure vibrational ns-CARS experiment developed by Satija and Lucht [19] and located in the same laboratory. The measured values are in agreement to within 0.2% of the calculated adiabatic flame temperature. The probe volume for the CPP fs-CARS measurements was located 35 mm above the center of the burner where the flame is most stable and product gases have reached equilibrium. Averaged experimental spectra and corresponding theoretical fits for each equivalence ratio are shown in Fig. 3.

Measurements in the Hencken burner at known flame temperatures provided the laser parameters required to theoretically model spectra obtained from flames of unknown temperature. Experimentally obtained reference spectra from each equivalence ratio were theoretically fit using a genetic algorithm based spectral fitting code, developed by Richardson et al. and described in detail in Refs. [20,21]. During this fitting process, the temperature was held constant at the adiabatic flame temperature and the laser parameters required to generate the theoretical spectrum were varied to obtain the best fit to the experimental spectrum. Each set of laser parameters obtained

from this procedure were then held fixed for analysis of CPP fs-CARS spectra from the turbulent GTMC flame. During the analysis of CARS spectra from the GTMC, only the temperature, the ratio of the resonant and nonresonant susceptibilities, and a linear scaling factor for intensity were allowed to vary. For each single-shot, CPP fs-CARS spectral fitting was performed using all four sets of laser parameters from room air and the reference flames. The temperature was determined by selecting the spectral fit with the lowest error.

The experimental precision and accuracy of the measurements was determined based on the mean and standard deviation, respectively, of probability density functions generated from 2000 single-shot measurements taken at each calibration condition in the Hencken burner. The CPP fs-CARS technique has excellent precision with a typical measured standard deviation of 1.5–2% of the mean flame temperature. Generally, the histogram mean values are a few degrees cooler than the calculated adiabatic flame temperature, though still within the estimated accuracy of 3%. The percentage accuracy of the measurement technique improved with increasing flame temperature. For example, during calibration a Hencken burner flame operated at an equivalence ratio of 0.8

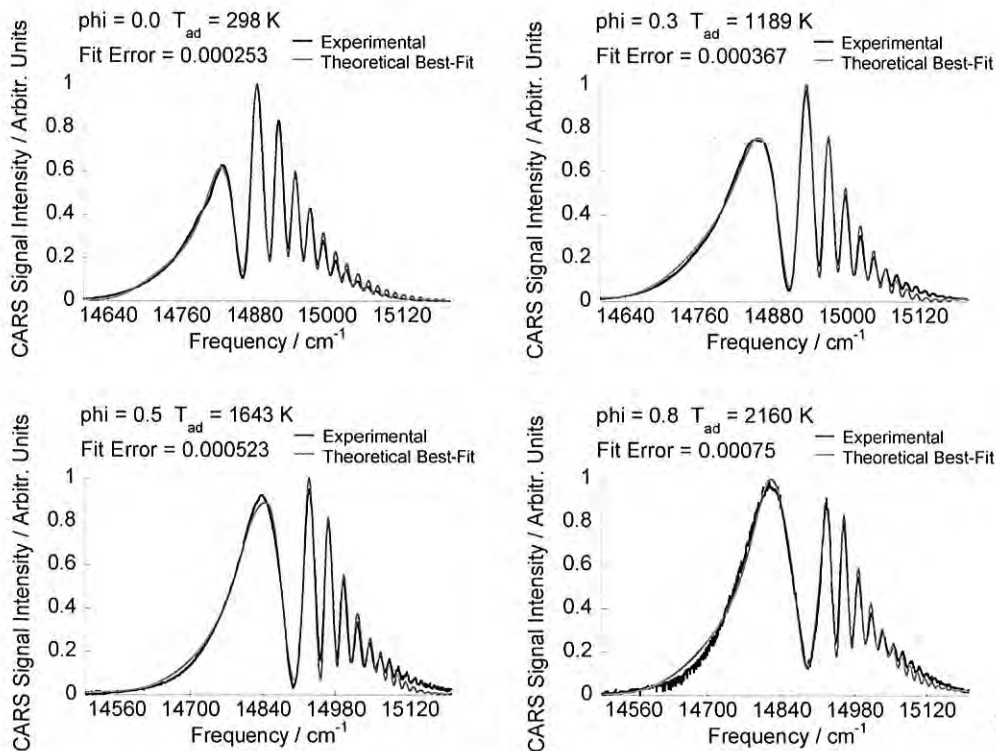


Fig. 3. Theoretical fits and experimental reference spectra representing an average of 2000 single-laser-shot measurements in the Hencken burner flame.

5-28

yielded the histogram shown in Fig. 4. The mean temperature at 2100 K was 2.7% below the adiabatic flame temperature of 2160 K and the standard deviation was 38 K or 1.8%.

2.3. Gas Turbine Model Combustor (GTMC)

The DLR GTMC used in this work has been the subject of numerous previous studies in which the geometry is described in detail [16,22,23,25], hence only a brief overview is provided here. A schematic diagram of the burner is shown in Fig. 5. Dry air was supplied to the plenum through an acoustic isolation section with an upstream choked orifice. Fuel and oxidizer flows were controlled by electromechanical mass flow controllers (Porter Series 200). A microphone (Bruel and Kjaer, Type 4939) was installed in the upstream plenum to monitor chamber acoustics. [23] The microphone signal was acquired simultaneously with the laser pulse and the EMCCD gate signals to synchronize the acoustics with the CARS measurements.

The flame studied in this work corresponded to the 'Flame V' condition in the work of Stohr et al. [23]. Air and methane were supplied to the burner at 324 g/min and 12.3 g/min, respectively. This corresponded to a global equivalence ratio of 0.65 and a thermal power of 10 kW. The burner was operated at this condition for thirty minutes, prior to data collection, to allow for thermal stabilization. This operating condition exhibited a thermo-acoustic pulsation at approximately 310 Hz consistent with previous work.

The time-averaged flow field corresponding to the Flame V condition was measured by Stohr et al. [23] and is shown in Fig. 6. The contours are streamlines representing the mean velocity field determined by extensive PIV characterization of the burner and the color scale indicates velocity magnitude in meters per second. The CARS measurement locations (indicated by black squares) were chosen to resolve the spatial structure of

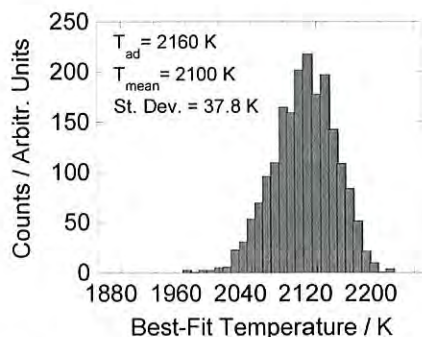


Fig. 4. Histogram resulting from 2000 single laser shot temperature measurements in the Hencken burner flame operated at $\phi = 0.8$.

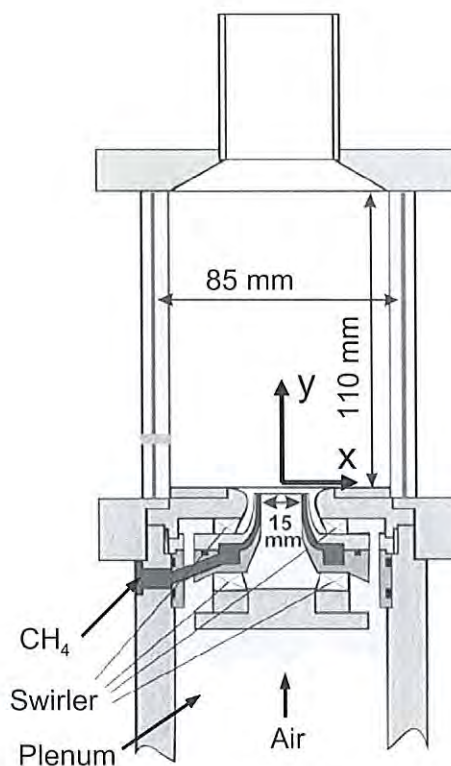


Fig. 5. Schematic diagram of DLR Dual-Swirl GTMC.

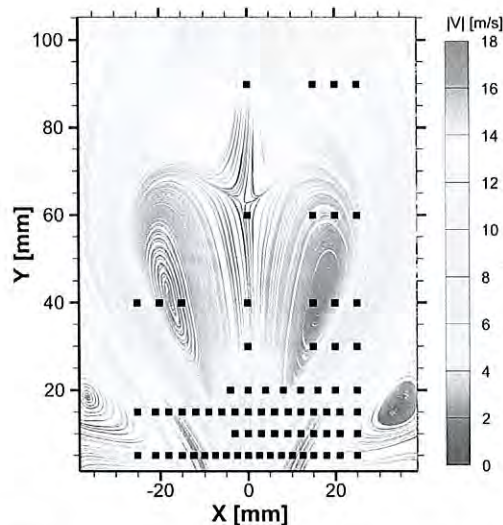


Fig. 6. CARS probe-volume locations with respect to mean flow field for the flame V operating condition.

the flame, with increased spatial resolution near the burner face. The demonstration of the temporally-resolved CARS temperature measurements in the highly turbulent shear layers near the flame

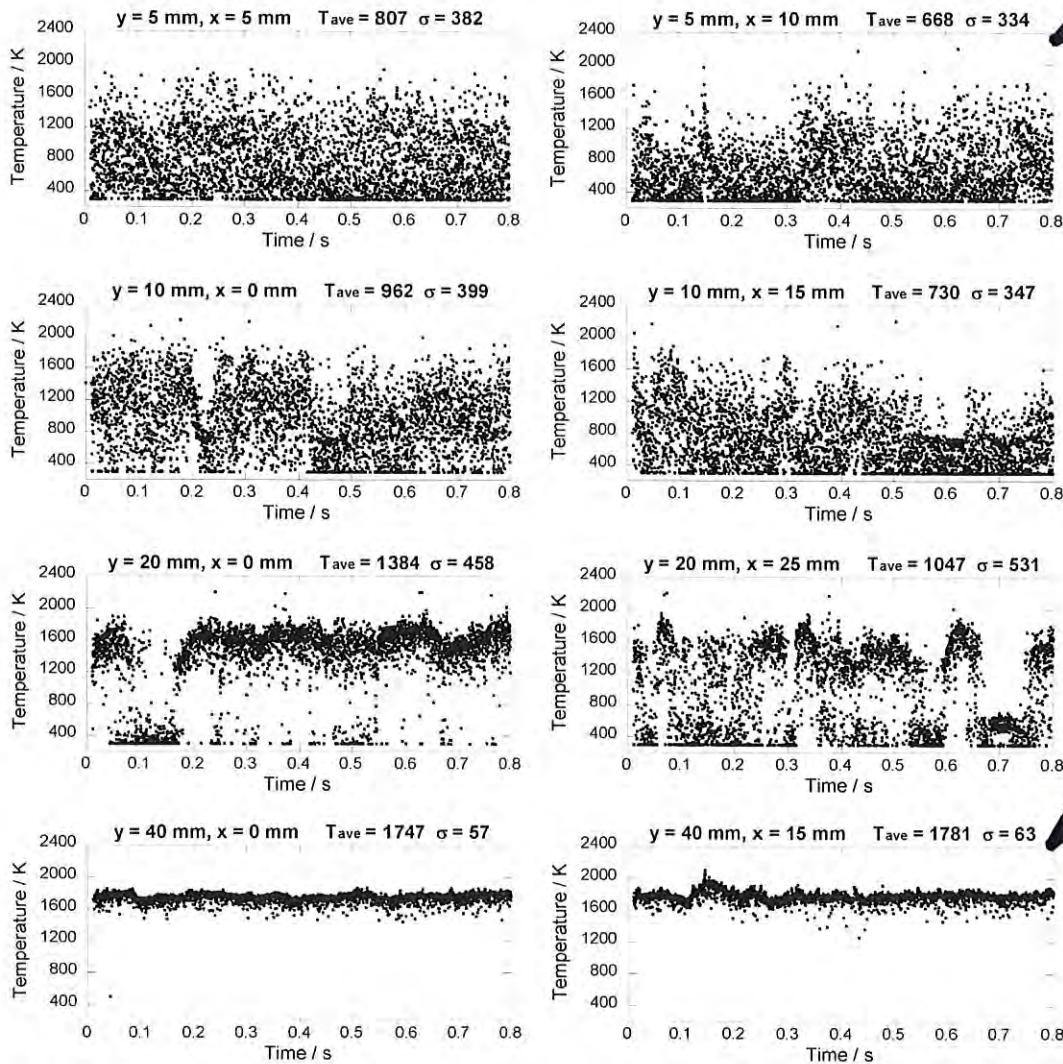
root was of key interest. A precessing vortex core coupled with unsteady flow–flame interactions dominates the flow physics in this region, resulting in highly unsteady temperatures [16,23,24].

3. Results

Measurements were performed at the grid locations shown in Fig. 6. Analysis of this data is still ongoing, but results from eight locations are shown in Fig. 7. For each probe volume location the mean temperature and the standard deviation are reported. The lower limit of temperature for the spectral fitting process was set to 300 K.

The probe volume locations at $y = 5$ mm and $x = 5$ and 10 mm, $y = 40$ mm and $x = 15$ mm,

and along the centerline are located within the inner recirculation zone. In this recirculation zone near the burner exit the measured temperatures vary widely; the variation decreases with axial distance as shown at $y = 20$ and 40 mm for $x = 0$. Probe volume locations at $y = 10$ mm and $x = 15$ mm, $y = 20$ mm and $x = 25$ mm coincide with the inner shear layer. As expected, the temperature increases with axial distance from the burner exit as combustion products reach equilibrium. The burner operating conditions corresponded to a global adiabatic flame temperature of 1750 K. At the location $y = 40$ mm, $x = 0$ mm, the measured mean temperature is around 1747 K, which agrees with the calculated post-flame temperature. In order to increase CARS signal levels in the high temperature post flame



← mixture of cold react. & hot products

← hot products

Fig. 7. Temperature measurements from 2000 consecutive single-laser-shots for 8 different probe volume locations.

5-30

regions where the density is low, the gain of the EMCCD camera was increased. An EMCCD gain setting of 5 was used at axial locations of $y = 15$, 20, and 30 mm, and a gain setting of 8 was used for locations at $y = 40$, 60, 90 mm. Without gain, in the high temperature regions, the CARS signal peaks at approximately 70 photoelectrons above background sensor levels. The time history plots for $y = 20$ mm, show instances where the temperature measurements appear to bottom out at the 300 K lower limit. For those laser shots the CARS signal was saturating the detector. We plan to employ a two CCD, two spectrometer system with 10% of the signal directed to one spectrometer-CCD system and 90% to the other to overcome this current dynamic range limitation.

To compare with existing thermo-acoustic measurements, eight locations were selected for power spectral density analysis. Results from two of the probe volume locations analyzed are shown in Figs. 8 and 9. The plotted data represents the average power spectra of temperature measurements acquired over five separate 5000 laser-shot acquisitions, representing five seconds of data acquisition.

The spectra show peaks at 176, 308, 485, and 796–805 Hz for the various axial and radial locations. Boxx et al. also observed a strong peak at 308 Hz, which was determined to be the dominant longitudinal thermo-acoustic pulsation of the flame. [16] The peak at 485 Hz is likely due to the PVC identified by Stöhr and Meier [22] and observed at 515 Hz by Boxx. Peaks occurring at 176 and 796–805 Hz are ± 308 Hz with respect to the PVC frequency and can be attributed to a superposition of thermo-acoustic pulsation and the precessing vortex core. [24] The same phenomenon was documented by Boxx et al. though occurring at 205, 515, and 822 Hz. Here the frequencies are shifted slightly, possibly due to the difference in the ambient operating conditions for each study though similar physics are represented.

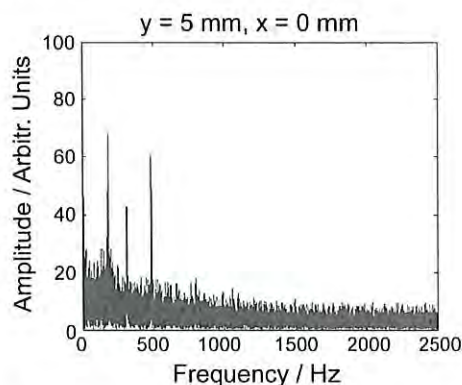


Fig. 8. Power spectrum from 25,000 CARS temperature measurements at $y = 5$ mm, $x = 0$ mm.

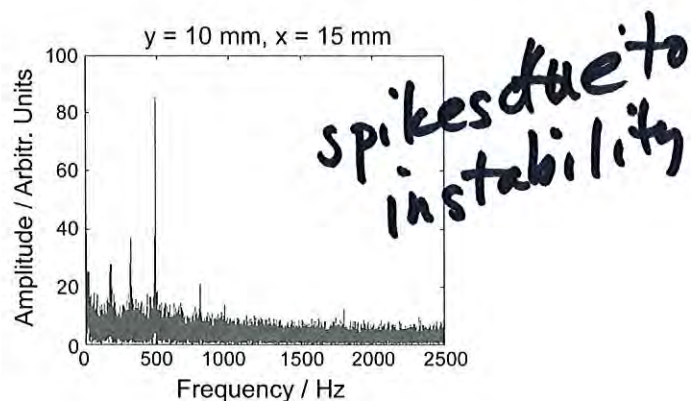


Fig. 9. Power spectrum from 25,000 CARS temperature measurements at $y = 10$ mm, $x = 15$ mm.

4. Conclusions

Chirped probe pulse femtosecond CARS has been successfully applied for flame temperature measurements in a model gas turbine combustor with significant swirl and high levels of turbulence. Every laser shot produced some resonant CARS signal; no significant loss of signal due to beam steering, pressure fluctuations, or shear layer density gradients was noticeable. Power spectral density analysis of the CPP fs-CARS thermometry results yielded the characteristic thermo-acoustic pulsation frequency previously reported at 308 Hz. These results demonstrate the usefulness of high repetition rate CPP fs-CARS for the study of turbulent combustion.

Acknowledgements

Funding for this work was provided by the U.S. Department of Energy, Division of Chemical Sciences, Geosciences and Biosciences under Grant No. DE-FG02-03ER15391. The ultrafast laser system was purchased with funding from AFOSR DURIP Grant No. FA9550-09-1-0387.

References

- [1] S. Roy, J.R. Gord, A.K. Patraik, *Prog. Energy Combust. Sci.* 36 (2) (2010) 280–306.
- [2] S. Roy, P.J. Kinnius, R.P. Lucht, J.R. Gord, *Opt. Commun.* 281 (2) (2008) 319–325.
- [3] J.R. Gord, T.R. Meyer, S. Roy, *Ann. Rev. Anal. Chem.* 1 (1) (2008) 663–687.
- [4] T. Lang, M. Motzkus, *J. Opt. Soc. Am. B* 19 (2) (2002) 340–344.
- [5] R.P. Lucht, P.J. Kinnius, S. Roy, J.R. Gord, *J. Chem. Phys.* 127 (4) (2007) 044316.
- [6] R.P. Lucht, S. Roy, T.R. Meyer, J.R. Gord, *Appl. Phys. Lett.* 89 (25) (2006) 251117.